12-12-2016 12:00 AM

X-ray Absorption and Emission Studies of Anodic Titania Nanostructures

Jun Li
The University of Western Ontario

Supervisor
Tsun-Kong Sham
The University of Western Ontario

Graduate Program in Chemistry
A thesis submitted in partial fulfillment of the requirements for the degree in Doctor of Philosophy

Recommended Citation
Li, Jun, "X-ray Absorption and Emission Studies of Anodic Titania Nanostructures" (2016). *Electronic Thesis and Dissertation Repository*. 4315.
https://ir.lib.uwo.ca/etd/4315

X-ray Absorption and Emission Studies of Anodic Titania Nanostructures

Jun Li

Supervisor
Tsun-Kong Sham
The University of Western Ontario

Graduate Program in Chemistry

A thesis submitted in partial fulfillment of the requirements for the degree in Doctor of Philosophy

Abstract

One-dimensional (1D) TiO_2 nanomaterials with ordered structure have been extensively applied in various fields, such as photocatalysts, solar cells, supercapacitors and rechargeable batteries, due to the unique structural and functional properties compared to the disordered nanoparticulate forms. Nevertheless, intrinsic disadvantages of TiO_2, such as its large band gap (~3 eV), fast recombination rate of photoexcited electron–hole pairs and insufficient ionic conductivity, severely limit the development of 1D TiO_2 nanomaterials for practical applications. To address the above issues, the scope of this thesis focus on the fundamental understandings of the electronic structure of highly ordered TiO_2 nanostructures upon the anatase-to-rutile solid phase transition, anion doping, noble metal decoration and sodium ion intercalation, using synchrotron based X-ray absorption, emission and related microscopy and spectroscopies.

X-ray absorption near edge structure (XANES) in combination with scanning transmission X-ray microscopy (STXM) is used to track the rutile nucleation site and the associated rutile growth behavior of 1D TiO_2 nanostructure. It is found that the bottom cap layer with its defective nature requires a lower thermal energy for rutile nucleation, and the growth of a dense rutile structure proceeds from the bottom to the top at the expense of nanostructured anatase TiO_2. The unzipping of the top nanotube into nanograss structure can further stabilize the anatase phase structure. To increase the photoabsorption and photoperformance of TiO_2, N-doped and Pd-decorated TiO_2 nanotubes are prepared. On one hand, a TiO_{2-x} anatase core warped by a Ti_4O_7 amorphous shell structure is achieved by N doping. The synergy for extraordinary photoabsorption established by this newly core-shell structure is revealed by XANES and resonant inelastic X-ray scattering (RIXS). On the other hand, the electronic and optical properties of Pd/TiO_2 Schottky heterojunction have been thoroughly investigated using X-ray absorption fine structure (XAFS), X-ray excited optical luminescence (XEOL) and RIXS to elucidate its enhanced photoactivity. Finally, amorphous and anatase TiO_2 nanotubes are comparatively studied for accommodating the sodium ion, of which XANES with its element and site specificities is applied to track the local effect of sodium uptake/release in TiO_2 nanotubes.

Keywords

X-ray absorption near edge structure, extend X-ray absorption fine structure, X-ray excited optical luminescence, resonant inelastic X-ray scattering, scanning transmission X-ray microscopy, TiO_2 nanostructures, electronic structure, anatase-to-rutile phase transition, nitrogen doping, palladium decoration, sodium intercalation

Co-Authorship Statement

This thesis contains materials from previously published manuscripts. Prof./Dr. Tsun-Kong Sham is co-authored on all published papers and he played a major role in editing and revising the content presented in this thesis.

In Chapter 3, TiO_2 nanotube lamella was prepared by Todd Simpson at Nanofabrication Laboratory, University of Western Ontario (UWO). STXM measurements were carried out by Dr. Z. Q. Wang. In Chapter 4, the sample synthesis was assisted by Dr. X. Li from Mechanical Engineering at UWO; TEM/HRTEM, XRD, UV-vis and XPS data were collected with the assistance of Dr. C. H. Liu from Soochow University; RIXS measurements were performed by Dr. Z. Q. Wang with the help of Dr. Y. C. Shao at the Advanced Light Source (ALS). In Chapter 5, RIXS data was collected at ALS with the help of Dr. Y. F. Ye. In Chapter 6, electrochemical experiments and the associated data analysis were performed by Dr. J. Liu and Dr. Q. Sun from Mechanical Engineering at UWO.

Technical support with synchrotron experiments at the Canadian Light Source (CLS) were provided by the following people: Dr. T. Regier at the SGM beamline, Dr. J. Wang at the SM beamline, Dr. Y. F. Hu at the SXRMB beamline and Dr. N. Chen at the HXMA beamline. Technical support at beamline 8.0 of ALS was provided by Dr. J. H. Guo.

To my family

Acknowledgments

First of all, I would like to thank my supervisor, Prof./Dr. Tsun-Kong Sham, for his remarkable guidance and unconditional support during my four-year graduate study. It has been quite an honor for me to work with such a great supervisor like him who has always showed me his insightful ideas, critical thinking and enthusiasm in studying science. Needless to say, he is very open-minded and offers me tons of great opportunities to communicate with the world about synchrotron research by visiting National Laboratories, attending domestic and international summer schools and conferences, which truly provide me international mobility in adopting the dynamic academic environment and the inner workings of the intellectual community.

Second, I want to thank my group members from both past and present: Dr. Yun-Mui Yiu, Dr. Zhiqiang Wang, Dr. Xiaoxuan Guo, Dr. Lijia Liu, Dr. Mohammad Norouzi Banis, Dr. Olga Lobacheva, Dr. Fuyan Zhao, Dr. Dong Zhao, Dr. Dejian Hou, Dr. Changhai Liu, Mr. Ankang Zhao, Ms. Madalena Sophia Kozachuk, Mr. Jiatang Chen, Mr. Hendrick Chan, Ms. Yingying Jiang, Mr. Aditya Balaji, Ms. Allison Halliday, Ms. Charllotte Wallace, Mr. Aaron Kirkey, Mr. Kristopher Kalhs, Mr. Biwei Xiao, Ms. Biqiong Wang, Mr. Wei Xiao, Ms. Fei Sun, Mr. Jiwei Wang and Ms. Minsi Li for all of their valuable suggestions and constructive feedback.

I also want to thank the technical supporters: Dr. Tom Regier, Dr. Jian Wang, Dr. Yongfeng Hu, Dr. Qunfeng Xiao and Dr. Ning Chen from the Canadian Light Source; Dr. Yifan Ye, Dr. Yuchen Shao and Dr. Yisheng Liu from the Advanced Light Source; Mr. Todd Simpson and Mr. Tim Goldhawk from Nanofabrication Laboratory, and Dr. Richard Gardiner from Biotron at the University of Western Ontario (UWO).

Moreover, I would like to thank my collaborators, Dr. Sui-Dong Wang's group at Soochow University, Dr. Xueliang (Andy) Sun's group at UWO and Dr. Jinghua Guo from Lawrence Berkeley National Laboratory for their support on sample synthesis and characterizations.

Research at the University of Western Ontario is supported by the Discovery Grant of the Natural Science and Engineering Research Council of Canada (NSERC), the Canada Research Chair (CRC) Program, the Canada Foundation for Innovation (CFI), and the Interdisciplinary Initiative (IDI) grant of UWO. Canadian Light Source (CLS) is supported by CFI, NSERC, National Research Council (NRC), Canadian Institute for Health Research (CIHR), and the University of Saskatchewan. I acknowledge the receipt of support from the CLS Graduate Student Travel Support Program from 2013 to 2016, and I gratefully acknowledge the Nanofabrication Facility at the University of Western Ontario for SEM imaging and EDX mapping. Advanced Light Source is supported by the Office of Basic Energy Sciences of the U.S. Department of Energy under Contract No. DE-AC02-05CH11231.

Finally, I would like to thank my parents and relatives in our whole big family under my grandparents in China for their unconditional love and support during my graduate study. I also would like to give my thanks to my friends in both China and Canada, my graduate study will not be that energetic and fruitful without them.

Table of Contents

List of Tables

List of Figures

List of Abbreviations

0D	Zero dimensional
1D	One dimensional
AGNT	As-grown nanotube
ALS	Advanced Light Source
APNT	As-prepared nanotube
ART	Anatase-to-rutile transition
CB	Conduction band
CCD	Charge-coupled device
CLS	Canadian Light Source
CVD	Chemical vapor deposition
DFT	Density functional theory
DI	De-ionized
EDX	Energy dispersive X-ray
EXAFS	Extended X-ray absorption fine structure
FIB	Focused-ion beam
FY	Fluorescence yield
HRTEM	High resolution transmission electron microscopy
HXMA	Hard X-ray MicroAnalysis
JCPDS	Joint Committee on Powder Diffraction Standards
LCF	Linear combination fitting
LIB	Lithium-ion battery

LINAC	Linear accelerator
LSV	linear sweep voltammetry
NC	Nanocrystal
NG	Nanograss
NIR	Near infrared
NNT	Nitrogen-doped nanotube
NP	Nanoparticle
NT	Nanotube
OD	Optical density
PCNT	Palladium-coated nanotube
PEC	Photoelectrochemical
PFY	Partial fluorescence yield
PGM	Plane grating monochromator
PL	Photoluminescence
PLY	Photoluminescence yield
RIXS	Resonant inelastic X-ray scattering
ROI	Region of interest
RXES	Resonant X-ray emission spectroscopy
SCE	standard calomel electrode
SEM	Scanning electron microscopy
SGM	Spherical Grating Monochromator
SIB	Sodium-ion battery

SM	SpectroMicroscopy
SR	Synchrotron radiation
STXM	Scanning transmission X-ray microscopy
SXRMB	Soft X-Ray Microcharacterization Beamline
TEM	Transmission electron microscopy
TEY	Total electron yield
UV	Ultraviolet
UWO	University of Western Ontario
VB	Valence band
WL	Whiteline
XAFS	X-ray absorption fine structure
XANES	X-ray absorption near edge structure
XAS	X-ray absorption spectroscopy
XEOL	X-ray excited optical luminescence
XES	X-ray emission spectroscopy
XPS	X-ray photoelectron spectroscopy
XRD	X-ray diffraction

Chapter 1

1 Introduction

1.1 Introduction to Nanostructured Titania

1.1.1 Titania Nanostructures Overview

In view of our rapacious consumption of the limited natural fossil resources and the subsequent global warming owing to the excessive release of CO_2, the generation and utilization of renewable clean energies are of foremost importance. By taking advantage of the clean and unlimited sunlight, for example, many efforts have been made to develop robust photocatalysts to generate hydrogen via solar water-splitting [1-3], reduce CO_2 to renewable hydrocarbon fuels [4-6], and functionalize many others [7-10]. In addition, rechargeable battery (e.g., lithium- and sodium-ion batteries) has been recently taken as one of the mostly studied clean energy systems using the renewable electricity [11-14]. All these developments aim to solve the global energy crisis without the cause of collateral damage to the environment.

Titania (TiO_2) has attracted a great deal of attention since its first discovery as a photocatalyst in 1972 [15]. In recent decades, research on TiO_2 has been devoted to its functionalization as not just photocatalysts [1,2,10], but also energy host materials for solar cells [8,9,16], supercapacitors [17,18], lithium- and sodium-ion batteries [11,12,14,19,20], due to its low cost, non-toxicity, superior stability and cyclability, as well as high rate performance.

In nature, anatase (tetragonal, space group $I4_1/amd$), rutile (tetragonal, space group $P4_2/mnm$) and brookite (orthorhombic, space group $Pbca$) exist as three crystalline phases of TiO_2 [21]. As shown in **Figure 1-1**, all crystal structures have the six-fold coordinated Ti atoms by connecting to O ligands, forming edge- and/or corner-linked TiO_6 octahedra with different distortions from the ideal O_h symmetry. Specifically, anatase holds a D_{2d} Ti local symmetry due to the displacements of O atoms from the equatorial positions, whereas the different in-plane (equatorial) and out-of-plane (axial) Ti-O bond lengths and two types of Ti-O-Ti in-plane bond angles deviating from 90 ° in rutile, result in its D_{2h} Ti local symmetry, and the more intense distortions in TiO_2 brookite, compared to the former two, with its all slightly different bond lengths and angles lead to the much lower C_1 Ti local symmetry [22].

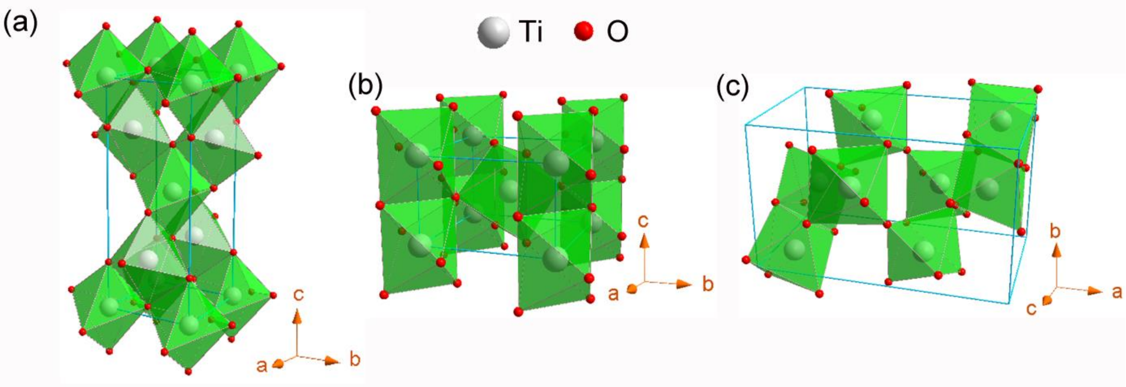

Figure 1-1 Crystal structure of TiO_2 polymorphs: (a) anatase, (b) rutile and (c) brookite.

Among these crystal structures, anatase and rutile TiO_2 are the two commonly studied polymorphs and are often taken as the subjects of investigation for technological applications due to their activities among others [1,2,8,23]. Nevertheless, two issues pertaining to TiO_2 itself constitute severe limitations and need to be well understood for the future scale-up development and applications. First, the band gaps of anatase (3.2 eV) and rutile (3.0 eV) TiO_2 are generally too large, which result in their ultraviolet (UV)-only photoabsorption and activity. As UV light only possesses ~5% of solar energy whereas most of its distribution (~95%) is in the visible and infrared regions [2,24], thus efforts on TiO_2 towards its photoabsorption of visible and/or infrared lights would arouse great interests for solar energy utilization. Second, the photogenerated electrons on the conduction band (CB) and the associated holes on the valence band (VB) of TiO_2, rather than migrating to the surface for photoactivity contribution, have a fast rate of recombination either in a direct way, or, in most cases, by trapping into surface defects of TiO_2 [1,2,25]. Hence, a further attempt (e.g., the erase or a proper control of surface defects) to elongate the lifetime of photogenerated electron–hole pairs in TiO_2 is a necessity for enhancing the photoactivity. To address these issues, different methods have been introduced and many of them have delivered some promising results [1,2,10,26,27].

First, in order to overcome the large band gap of TiO_2 (**Figure 1-2a**), the introduction of a secondary species into the titania lattice is found to be able to tune the TiO_2 band gap by adjusting the associated CB and VB energy levels [21]. Particularly, doping of TiO_2 with non-metal elements has been broadly enforced to tailor the TiO_2 band gap, of which the generation of band tail states right above the VB of TiO_2 by doping of non-mental elements is essentially believed to reduce the gap energy for enhanced photoabsorption as well as photoactivity in visible and infrared regions (**Figure 1-2b**) [1,10,28,29]. The very first attempt was initiated by Asahi et al. who reported that the N-doping in TiO_2 can lead to the enhanced photocatalytic degradation of methylene orange under visible light irradiation [10]. Since then, a lot of works related to N-doped TiO_2 have been conducted using various methods to pursue the high visible light photoactivity [26,30-34]. Moreover, doping of TiO_2 with other non-metals, such as C, F and S, has also been investigated both experimentally and theoretically [10,30,35-39]. Different synthesis methods such as hydrothermal, sputtering and thermal annealing have been employed to facilitate these doping processes [1,21,37,38,40]. Of these, thermal treatment of TiO_2 in certain atmospheres (e.g., NH_3, H_2S and H_2) is reported as a judicious doping route to attain doped TiO_2 species with improved photoresponse and higher photoelectron conversion efficiency by comparing to the bare one [1,26,37]. A great success has been achieved by Chen et al. [1] who recently synthesized a black core-shell TiO_2 using the high pressure hydrogen annealing, this newly formed black TiO_2 specimen has shown its extraordinary visible and infrared photoabsorption and superior solar water-splitting photoactivity and stability. On the other hand, doping of TiO_2 with transition metal species such as Cr, Fe, and Ni has also been studied [41-44]. Nevertheless, although the incorporation of metal cations into titania matrix can extend the photoabsorption of TiO_2 to visible region, the associated gap states (mainly around the CB of TiO_2, **Figure 1-2c**) generated by these foreign metal species would be exciton trap states which accelerate the recombination of photoexcited electron–hole pairs, resulting in lower photocatalytic activity [1,42].

Second, TiO_2 morphology engineering, phase control and noble-metal sensitizing are recognized as three promising paths to separate the photogenerated electrons and holes. It is well documented that zero-dimensional (0D) TiO_2 nanoparticles (NPs) have shown

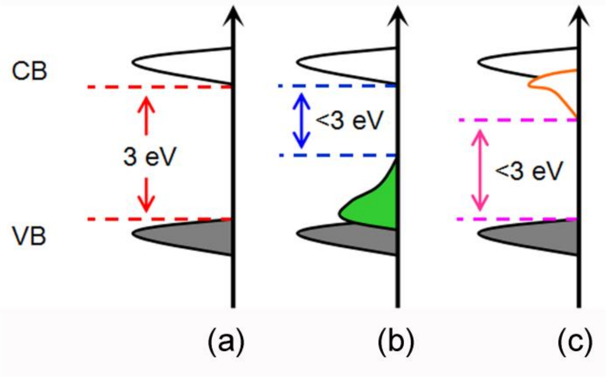

Figure 1-2 Schematic illustration of TiO_2 band gap modification: (a) bare TiO_2, (b) non-metal doped TiO_2, and (c) metal-doped TiO_2.

their excellent photoperformance as well as many others due to their large surface area [45-48]. However, the increase of surface defects related to the increased surface area and the slow charge carrier transfer in nanoparticulate form result in the fast recombination of photogenerated electrons and holes as these defects mostly act as recombination centers [21,49]. Instead, the synthesis of 1D TiO_2 nanostructure would greatly suppress such recombination processes, since the as-prepared 1D structures not only hold the inherent advantages of 0D TiO_2 NPs, but also facilitate the transfer of photogenerated charge carriers along their axial direction, leading to improved photocatalytic activity (**Figure 1-3a**) [21,25,50,51]. Accordingly, various attempts using sol-gel, hydrothermal, electrochemical anodization as well as other methods, have been applied to synthesize 1D TiO_2 structures in the shapes of nanotube, nanowire, nanobelt and nanorod [32,51-54]. In particular, highly ordered 1D TiO_2 nanotubes (NTs) prepared by a facial electrochemical anodization, have attracted a great deal of attention lately due to its large surface area, easy control of tube parameters (e.g., length, thickness and tube diameter) and the self-oriented tube arrays with the unidirectional tunnels for fast charge carrier transfer [55]. These anodic 1D TiO_2 NTs have been widely used in photocatalysis [56,57], water-splitting [2,58] and solar cells [16,59]. Another feasible route to prevent the fast recombination of photoexcited electron–hole pairs is constructing a multi-phase heterostructure. A typical example is the anatase-rutile mixed phase structure. It is well known that TiO_2 nanostructures with a certain ratio of anatase/rutile phase would deliver a synergy for elongating the lifetime of photogenerated charge carriers, resulting in the

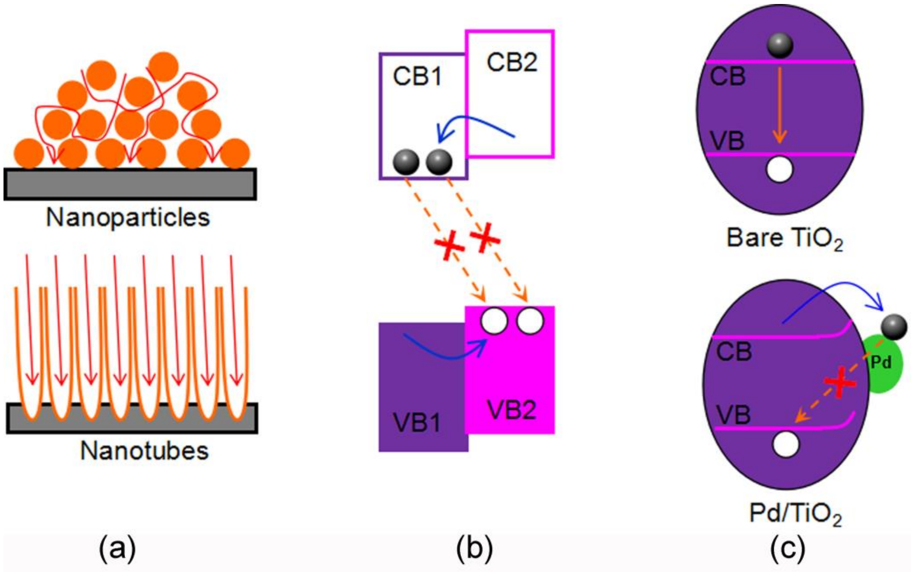

Figure 1-3 Schematic illustration of the electron–hole recombination suppression by (a) ordering the TiO_2 nanostructure: migration of charge carriers in nanoparticles (top) and nanotubes (bottom), (b) forming anatase-rutile mixed phase structure, and (c) constructing metal/TiO_2 heterostructure.

synergistic efficiency in photocatalysis (**Figure 1-3b**) [27,60,61]. In fact, a nanoparticulate TiO_2 with an anatase/rutile weight ratio of 80/20 has been commercialized as Degussa P25 due to its strong photoactivity, which is often used as a standard for photoperformance comparison in TiO_2 research [27,37,38,62]. Thereafter, more and more researchers have engaged in anatase-to-rutile transition (ART) investigations to understand the associated ART mechanism for preparing efficient anatase-ruitile mixed phase structures with improved photocatalytic activity [63-66]. So far, the gain of insights in ART study of TiO_2 has been carried out mainly by focusing on the size [66-68], morphology [65,69] and crystal anisotropy [63,64] dependences. In addition, noble-metal (Ag, Au, Pd and Pt) sensitizing has long been introduced to TiO_2 host structure for boosting its photoactivity by efficiently separating the photogenerated electrons on CB and holes on VB of TiO_2 [2,62,70,71]. The general consensus is that those attached secondary metal NPs act as electron sinks by attracting and holding the photoexcited electrons, thus impeding their recombination with holes on the VB of TiO_2 (**Figure 1-3c**). It can be rationalized as [25,62]: (1) the lower Fermi level energy of noble metal/TiO_2 heterostructure (once attached, the Fermi level of noble metal and TiO_2 will be equalized) than the CB energy of TiO_2 would facilitate the migration of photoexcited electrons from the CB of TiO_2 to those attached noble metal sites; (2) the formation of a Schottky barrier at the interface of noble metal/TiO_2 would prevent the back-transfer of electrons from the noble metal sites to the CB of TiO_2. Indeed, lots of successes exemplify the synergy within the noble metal/TiO_2 heterostructure. Especially, a recent report using Pd quantum dots sensitized TiO_2 NTs showed the extraordinary photoactivity towards the solar water-splitting for hydrogen generation [2].

Furthermore, it should be pointed out that TiO_2 is a versatile material which has also been widely adapted to battery research [11,72-74]. For example, anatase TiO_2 used as anode material has showed its great potential for accommodating Na^+ in sodium-ion battery (SIB) system, demonstrating the superior cyclability and high rate performance [11,12]. The cause of a great interest in anatase TiO_2-based SIB research is due to the following advantages [11,23]: (1) two-dimensional Na^+ diffusion tunnels along the a and b axis (**Figure 1-4**) with a size of 3.725 Å × 3.785 Å suitable for the interstitial accommodation of Na^+ (1.02 Å), (2) low insertion potential (~1 V vs. Na^+/Na), and (3) high theoretical capacity of ~335 mAh g^{-1}.

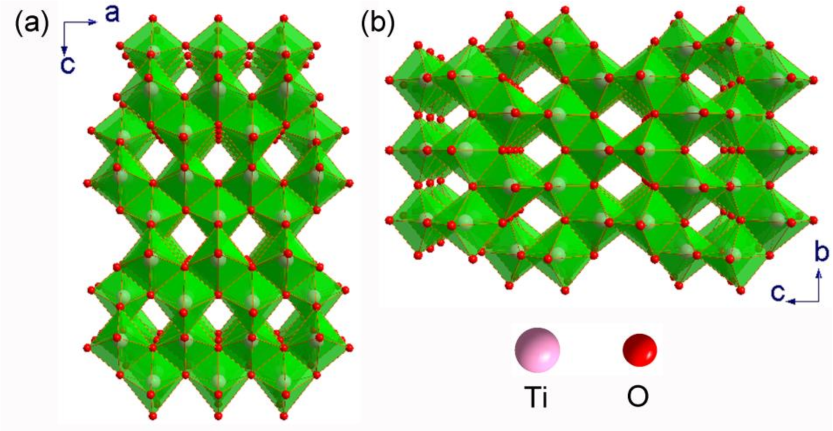

Figure 1-4 View of the anatase TiO_2 crystal structure along its b (a) and a (b) axis.

In this thesis, highly oriented TiO_2 nanostructure prepared by electrochemical anodization is chosen as the base material to examine its electronic and structural properties corresponding to the phase transition (particularly the ART behavior), anion doping (nitrogen and fluorine), palladium sensitization, and sodium ion intercalation. The goal, as mentioned above, is to fabricate functional 1D TiO_2 nanostructures to be used in clean solar energy systems as well as battery devices by understanding the associated mechanisms.

1.1.2 Synthesis of Anodic Titania Nanostructures

The synthesis of vertically oriented TiO_2 NT arrays using a facial electrochemical anodization method, has been broadly applied to titania-related research over the last two decades. The first attempt to attain anodized TiO_2 was initiated by Assefpour-Dezfuly et al. in 1984 who reported the synthesis of a porous TiO_2 nanostructure by anodization in chromic acid [75]. It initially did not draw much attention until 1999 when Zwilling et al. fabricated a much ordered nanoporous TiO_2 by anodization in a fluorine-containing electrolyte [76]. Since then, a fluorine-containing electrolyte is recognized as a necessity to form and sustain the TiO_2 nanoporous/nanotubular structure [55], great efforts have been dedicated to obtain fine TiO_2 NT structure by optimizing the experimental parameters, particularly the evolutions of electrolyte components. Four generations of electrolyte have been developed to tune the morphology of as-anodized TiO_2 NTs as shown in **Table 1-1** [55]. In general, a hydrofluoric acid aqueous electrolyte is firstly applied for TiO_2 NT growth. Nevertheless, the fast dissolution rate of as-formed NT in HF solution results in the short NT length with poorly self-organized NT structure [77,78]. Later on, fluorine-containing inorganic and organic neutral electrolytes are introduced for TiO_2 NT preparation with a much longer NT length and smoother NT wall [26,52,79-81]. Of which an electrolyte composition of NH_4F (0.1 ~ 0.5 wt. %), H_2O (0.1 ~ 5 wt. %) and ethylene glycol has been widely utilized for the scale-up synthesis of highly ordered TiO_2 NTs with tunable NT parameters, i.e., length, diameter, thickness. Moreover, a multi-step approach has been developed using this type of electrolyte to achieve desired NT morphology for various applications [2,26,58].

Other experimental parameters such as anodization potential, time and temperature, are also very important for the fine tuning of NT morphology [21,55]. Whereas the anodization voltage usually affects the NT diameter, the anodization time would mainly influence the NT length, and the temperature of electrolyte has an impact on the dissolution rate of NT which is normally set at room temperature (20 ~ 25 ℃) for the case of Ti anodization [55].

Table 1-1 Four generations of electrolyte for the synthesis of TiO_2 NTs [55].

TiO_2 NTs	Electrolyte	NT Morphology	References
1st generation	HF aqueous solution	200 ~ 500 nm long; poorly organized; ribbed NT wall	[77,78]
2nd generation	Aqueous solution of fluoride salts	0.5 ~ 2.4 μm long; self-organized; ribbed NT wall	[79,80]
3rd generation	Organic solution (e.g., glycerol) of fluoride salts with a small amount of H_2O	100 ~ 1000 μm long; self-organized; smooth NT wall	[81,82]
4th generation	Organic solution (e.g., ethylene glycol) of fluoride salts with a small amount of H_2O	100 ~ 1000 μm long; highly self-organized; smooth NT wall; Fine optimization of NT anodization	[26,83]

1.2 Synchrotron Radiation Overview

Synchrotron radiation (SR) is an electromagnetic radiation emitted when electrons are accelerated to the speed of light and directed in a curved orbit within external magnetic field. It did not receive much attention as a powerful tool until 1960s when the first dedicated synchrotron light source, Tantalus I, became operational in 1968 even though the theoretical description of SR was established in the 1920s [84]. Nowadays, more than 50 synchrotron light sources are operational and accessible by general users, including the Canadian Light Source (CLS, SK, Canada) and Advanced Light Source (ALS, CA, USA) used in this thesis. **Figure 1-5** shows the general layout of a modern SR facility.

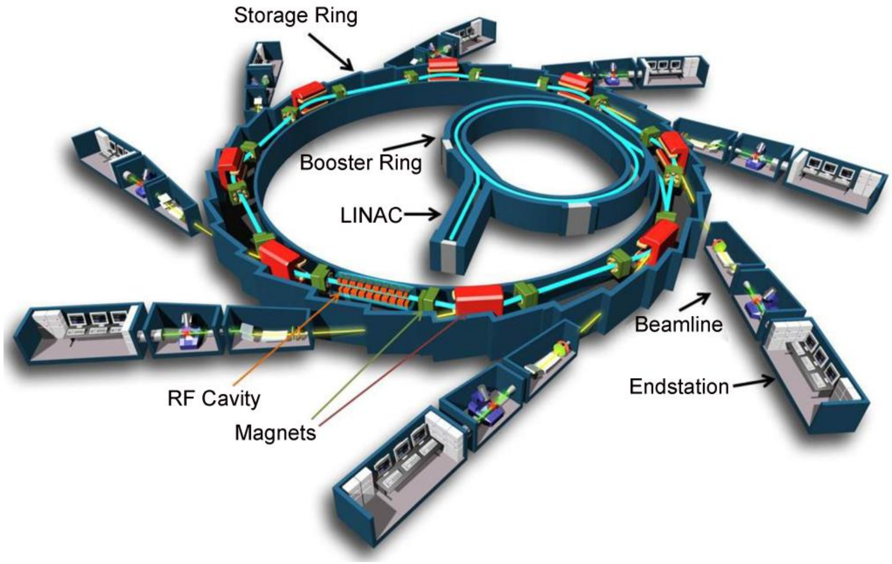

Figure 1-5 Schematic layout of SR facility [85].

1.2.1 The Generation of Synchrotron Radiation

To obtain synchrotron light, a particular cathode (electron gun) is used and heated to ~1000℃ to generate electrons which will be injected into the linear accelerator (LINAC) to speed up and achieve the 99.9998% of the speed of light with the energy to the order of MeV under a high voltage. Then electrons are fed into the booster ring to increase the energy of electrons to the order of GeV, and finally electrons are transferred into the storage ring where the electrons circulate at nearly the speed of light and emit the electromagnetic radiation tangentially to the curved orbit. In the storage ring (**Figure 1-5**), several sets of dipole/bending magnets (red) and quadrupole magnets (green) located around the circulator orbit are used to bend the accelerated electrons to get a 360 °circular beam in total and maintain the transverse dimension of the beam, respectively. In the current third generation synchrotron facilities, wiggler and undulator are used as insertion devices to attain a collimated beam with a much higher brightness compared with bending magnets (**Figure 1-6**), because the wiggler with a short period and large bend structure can produce a continuum of radiation while the undulator with a long period and small bend structure takes advantage of the phasing/interference effects to produce more collimated beam (spike-like peaks) with a much smaller spatial distribution. Hence, SR can be produced either by the bending magnets (tangential to the orbit) or by insertion devices at straight sections. The differences of spatial distribution generated by various magnets can be discriminated by the opening angle (1/γ) in **Equation 1-1**:

$$\gamma = \frac{E}{m_0 c^2} \approx 1975E(\text{GeV}) \qquad (1\text{-}1)$$

Where γ is the mass ratio between the mass of a relativistic electron and its rest mass (m_0), E is the energy and c is the speed of light. As shown in **Figure 1-6a**, compared to the opening angle (1/γ) of bending magnet, a much larger opening angle (>>1/γ) is produced by wiggler due to the high magnetic field involved, whereas undulator generates a smaller opening angle (1/$\gamma\sqrt{N}$, N is the number of magnets) with the application of low magnetic field [86].

In addition, a radio frequency cavity, the so-called "the heart of synchrotron", is also inserted in the storage ring at a straight section (**Figure 1-5**). It is been used to replenish the energy loss of electrons due to SR by providing a time varying electric field (voltage) that gives the electron a boost when it passes the accelerating gap.

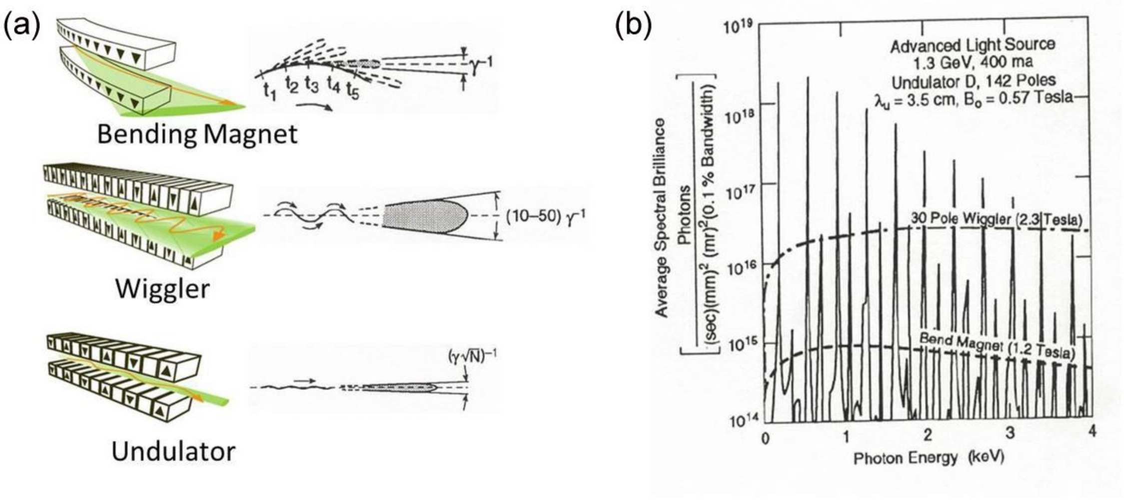

Figure 1-6 (a) Spatial and (b) spectral distributions of bending magnets, wiggler and undulator [86,87].

1.2.2 The Generation of Soft and Hard X-rays

As synchrotron light has a broad energy range from infrared to hard X-ray, the generation of an energy-specific photon beam is carried out using different types of optical elements. Specifically, grating and double-crystal monochromators are employed to produce the soft and hard X-rays, respectively.

Figure 1-7a shows the grating monochromator for generating soft X-ray. Once the incident light reaches the grating with a grazing angle, various diffraction lights with different energies (different diffraction angles) as well as the zero-ordered reflected light will be produced. Then by either rotating the grating (rotatable) or moving the optical aperture (movable), a beam with a specific energy can exit at a fixed angle. As demonstrated in **Figure 1-7b**, the physical principle of grating diffraction follows the **Equation 1-2**:

$$n\lambda = d(\sin\alpha \pm \sin\beta) \qquad (1\text{-}2)$$

Where n is the order of the diffraction, λ is the wavelength of the diffraction light, d is the distance between the grating lines, α and β are angles of incidence and diffraction, respectively.

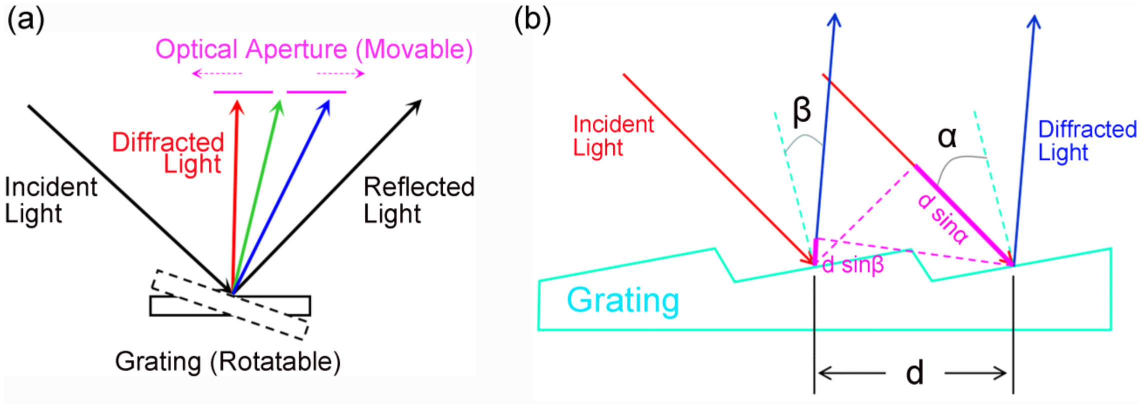

Figure 1-7 Schematic illustrations of (a) grating monochromator and (b) diffraction result from a typical Echellette-type grating.

As for Hard X-ray generation, a double-crystal monochromotor containing two identical crystals (i.e., same element and d-spacing) is usually applied. As shown in **Figure 1-8a**, an energy-specific beam with a fixed exit angle is produced by rotation and translation of the two paralleled crystals based on the Bragg's **Equation 1-3**.

$$n\lambda = 2d\sin\theta \qquad (1\text{-}3)$$

Where n is the order of diffraction, λ is the wavelength of photon beam, d is the lattice spacing as indicated in **Figure 1-8b**, and θ is the Bragg (grazing) angle. Different crystals such as Si (111), Si (333) and InSb (111) with different d-spacing values are typically used for energy selection.

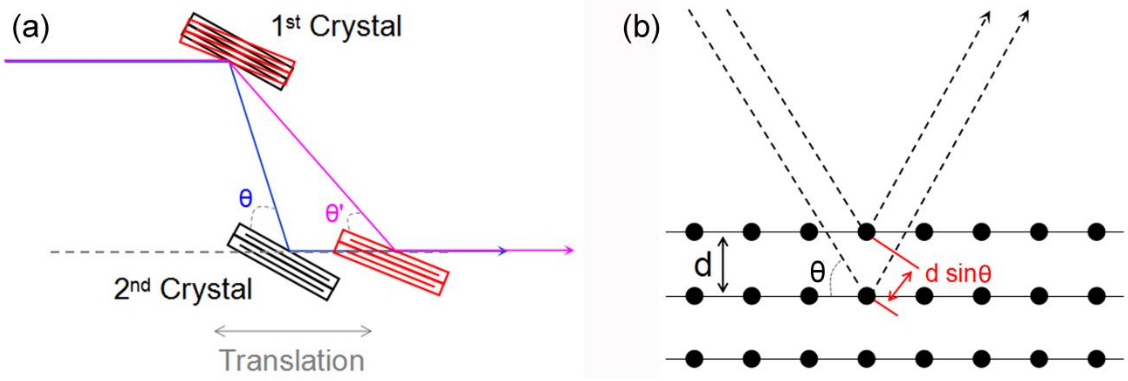

Figure 1-8 Schematic illustration of (a) a double-crystal monochromator, and (b) Bragg diffraction.

1.2.3 The Advantages of Synchrotron

Overall, SR holds many advantages over the traditional X-ray source [88], such as tunability, brightness, polarization and time structure. Specifically, SR provides photon beam with a tunable energy from IR to hard X-ray. The flux of SR can reach as high as 12 orders of magnitude than the traditional X-ray to provide a much higher brightness, and the highly collimated beam of SR can provide high spectral resolution. Moreover, SR also can generate photons which are linearly polarized in the plane of orbit and elliptically polarized out of the orbit plane. In addition, bunched electrons produced by RF cavity are pulse wave with a few nanoseconds between pulses, providing the performance of time-resolved spectroscopy. In this thesis, the X-ray absorption and emission analysis of titania-based nanostructures particularly benefit from the tunability and brightness advantages of SR, which offer the high spectral and spatial resolutions.

1.3 X-ray Absorption, Emission and Related Synchrotron Techniques

1.3.1 X-ray Absorption Fine Structure

When X-ray interacts with matter, either a partial or total X-ray absorption takes place. In general, the X-ray absorption/attenuation process follows the Beer-Lambert Law (**Equation 1-4**):

$$\frac{I_t}{I_0} = e^{-\mu t} \qquad (1\text{-}4)$$

Where I_t and I_0 are the intensities of transmitted and incident X-rays, respectively, t is the sample thickness, and μ is the absorption coefficient which can be described as follows (**Equation 1-5**):

$$\mu \approx \frac{\rho Z^4}{AE^3} \qquad (1\text{-}5)$$

Where ρ is the sample density, Z is the atomic number, A is the atomic mass, and E is the X-ray energy. It is apparent that the absorption coefficient μ is highly correlated with both atomic number Z and X-ray energy E, which suggests that X-ray absorption spectroscopy is an element-specific technique. At the same time, the absorption coefficient μ can also be described by the X-ray absorption cross section σ as (**Equation 1-6**):

$$\mu = \sigma \cdot \rho \qquad (1\text{-}6)$$

Once the energy of incident X-ray E is approaching the binding energy of a core electron (e.g., Pt 1s electron), a sharp increase of X-ray absorption cross section σ as well as the increase of absorption coefficient μ occurs by enhanced X-ray absorption. In experiment, element-specific fine structures as a function of incident photon energy show up once the core electron is excited from its core state to an unoccupied bound state, quasi-bound state and further to the continuum (photoelectric effect) as the X-ray energy increases, which can be referred to as an absorption edge. For example, the X-ray absorption cross section *σ* of platinum as a function of incident X-ray photon energy *E* is shown in **Figure 1-9**, of which the Pt-specific K, L_1, L_2 and L_3 edges are included. Note that the nomenclature of an absorption edge comes from the shell name of the core-electron that is being excited. Accordingly, excitations of the Pt 1s (K-shell), 2s (L_1-shell), $2p_{1/2}$ (L_2-shell) and $2p_{3/2}$ (L_3-shell) electrons correspond to the Pt K-edge, L_1-edge, L_2-edge and L_3-edge, respectively. Hence, for atoms in a chemical environment, X-ray absorption fine structure (XAFS) at a certain (element-specific) absorption edge can be observed when the X-ray is scanned across the associated absorption threshold E_0 as the absorption coefficient μ is energy-dependent, i.e., XAFS can be referred to the modulation of the absorption coefficient μ as a function of X-ray photon energy *E*.

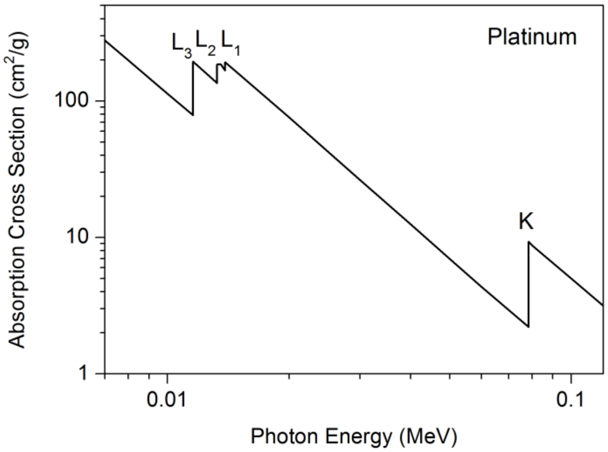

Figure 1-9 Log-log plot of X-ray absorption cross section (*σ*) of platinum as a function of X-ray photon energy (*E*) [89].

Typically, XAFS includes two parts: X-ray absorption near edge structure (XANES, ~20 eV below and ~50 eV above the absorption edge) and extended X-ray absorption fine structure (EXAFS, from ~50 eV to ~1000 eV above the edge). The separation of these two regions is mainly based on the different scattering behaviors of the electrons which hold different kinetic energies. In general, XANES originates from electronic transition into bound and quasi-bound states together with the multiple scattering interferences from the neighboring atoms due to the low kinetic energy of electron. As a local probe technique, XANES provides the local information of absorbing atom, such as unoccupied electronic states, oxidation states and local symmetry [26,65]. On the other hand, outgoing electron with much higher kinetic energy favors a single scattering process, contributing to the EXAFS. It offers local information, such as bond length and coordination number within the nearest 3 atomic shells of absorbing atom [25].

As mentioned above, XANES results from the multiple scattering process of photoexcited electron (from absorbing atom) with neighboring atoms, the related total absorption coefficient in an atomic cluster can be expressed as (**Equation 1-7**):

$$\mu(E) = \mu_0[1 + \sum_{n \geq 2} \chi_n(E)] \qquad (1\text{-}7)$$

Where μ_0 is the absorption coefficient of the absorbing atom, and $\chi_n(E)$ is a multiple scattering term which includes all the scattering contributions from the n-1 neighboring atoms as demonstrated in **Figure 1-10**.

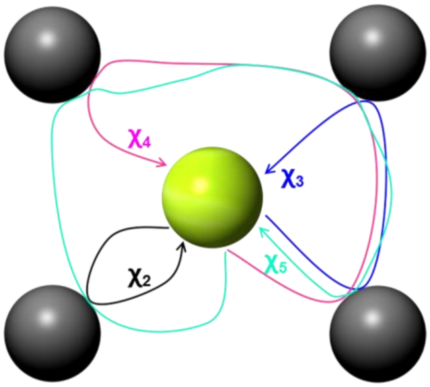

Figure 1-10 Schematic illustration of multiple scattering processes, where χ_n represents a scattering pathway involving n atoms.

Theoretically, one-electron approximation is usually applied to describe the X-ray absorption process; that is that upon X-ray excitation, a single core-electron within a N-electron atomic system is excited, whereas the rest N-1 electrons remain in their core level without absorbing the X-ray energy. Hence, the absorption coefficient μ is proportional to the probability of an electron transition between the initial and final quantum states by one-photon absorption. This electronic transition probability can be described based on Fermi’s gold rule as (**Equation 1-8**):

$$\mu \propto |\langle \psi_i | H | \psi_f \rangle|^2 \, \delta(\mathrm{E}_f - \mathrm{E}_i - \hbar\omega) \qquad (1\text{-}8)$$

Where ψ_i and ψ_f are the initial and final state functions with their eigenvalues of E_i and E_f, respectively, and H is the interaction Hamiltonian between the electromagnetic field and the electron which can be written as (**Equation 1-9**):

$$H = (\boldsymbol{\varepsilon}\,\boldsymbol{r})\mathrm{e}^{(i(\boldsymbol{k}\,\boldsymbol{r}))} = (\boldsymbol{\varepsilon}\,\boldsymbol{r}) + (\boldsymbol{\varepsilon}\,\boldsymbol{r})(\boldsymbol{k}\,\boldsymbol{r}) + \cdots \qquad (1\text{-}9)$$

Where $\boldsymbol{\varepsilon}$ is X-ray electric field vector, $\boldsymbol{r}$ is the electron coordinate vector, and $\boldsymbol{k}$ is the forward scattering vector. As shown in **Equation 1-9**, the expansion of the Hamiltonian contains two major terms: a dipole component $(\boldsymbol{\varepsilon}\,\boldsymbol{r})$ and a quadrupole component $(\boldsymbol{\varepsilon}\,\boldsymbol{r})(\boldsymbol{k}\,\boldsymbol{r})$. In XANES, the dipole term is dominant, thus the electronic excitation mainly follows the dipole selection rule ($\Delta l = \pm 1$, $\Delta j = \pm 1, 0$). For example, electronic transition from $2p_{1/2}$ core states to $3d_{3/2}$ final states is dipole-allowed, whereas transition to $3d_{5/2}$ or $3p_{1/2,\,3/2}$ is dipole-forbidden. On the other hand, the quadrupole component ($\Delta l = \pm 2, 0$; i.e., 1s to 3d transition) in **Equation 1-9** is much weaker in several orders of magnitude compared to the dipole component. Nevertheless, the absorption cross section of the quadrupole component becomes prominent, particularly in the K-edge XANES of transition metals due to its high sensitivity to metal d electron-ligand hybridization [90]. As a result, this weak quadrupole transition would result in the pre-edge features before the main edge absorption.

Unlike the multiple scattering process in XANES, photoelectron with its much higher kinetic energy in the EXAFS region undergoes single scattering, and the associated EXAFS function $\chi(E)$ is defined as (**Equation 1-10**):

$$\chi(E) = \frac{\mu(E) - \mu_0(E)}{\mu_0(E)} \qquad (1\text{-}10)$$

Where $\mu(E)$ is the measured absorption coefficient from experiment, and $\mu_0(E)$ is a smooth background function which represents the X-ray absorption of an isolated atom. To better address the wave behavior of photoelectron in EXAFS region, it is common practice to convert from $\chi(E)$ to $\chi(k)$ since the wave number k is defined as (**Equation 1-11**):

$$k = \sqrt{\frac{2m_e(E - E_0)}{\hbar^2}} \qquad (1\text{-}11)$$

Where m_e is the electron mass. Therefore, EXAFS can be denoted as the modulation of the absorption coefficient as a function of the wave number k of the photoelectron. By performing the single scattering analysis, the final EXAFS formula can be expressed as (**Equation 1-12**) [91]:

$$\chi(k) = \sum_j A_j(k)\sin[2kr_j + \phi(k)] \qquad (1\text{-}12)$$

Where j is a coordination shell in which all identical scattering atoms on this shell share the same distance r_j from the absorbing atom. As demonstrated in **Equation 1-12**, the EXAFS function $\chi(k)$ representing the oscillation of photoelectron is composed by two terms: the amplitude $A(k)$ and the phase $\phi(k)$. A Fourier transformation is usually carried out to separate these two components. It can provide the local information of the absorbing atom, such as coordination number and bond distance from different shell j.

1.3.2 De-excitation Process

With one-electron approximation, once a core-electron is excited to continuum as a photoelectron by X-ray, a core-hole is created (**Figure 1-11a**). Then electron from a shallower level would come down to fill the core-hole by de-excitation. Two competing processes are indicated in **Figure 1-11b** and **11c**, this de-excitation can be either non-radiative Auger electron ejection or radiative X-ray fluorescence emission. Specifically, in the two-step Auger process, while an electron from a shallower shell comes down to fill the core-hole, the released non-radiative energy would be transferred to excite another core-electron at an outer shell. Alternatively, the energy can also be released in one step as radiative X-ray fluorescence. As both processes are directly correlated with the core-hole created by X-ray excitation, thus both the Auger yield and fluorescence yield are proportional to the absorption coefficient (μ) of element of interest for XANES measurement. **Figure 1-11d** shows the fluorescence yield for K and L shells as a function of atomic number *Z*, it is obvious that whereas the fluorescence decay is predominant in high *Z* elements, the low *Z* elements have a higher fraction of Auger decay process instead, as the fractions of these two yields relative to the total decay add up to 1 [92].

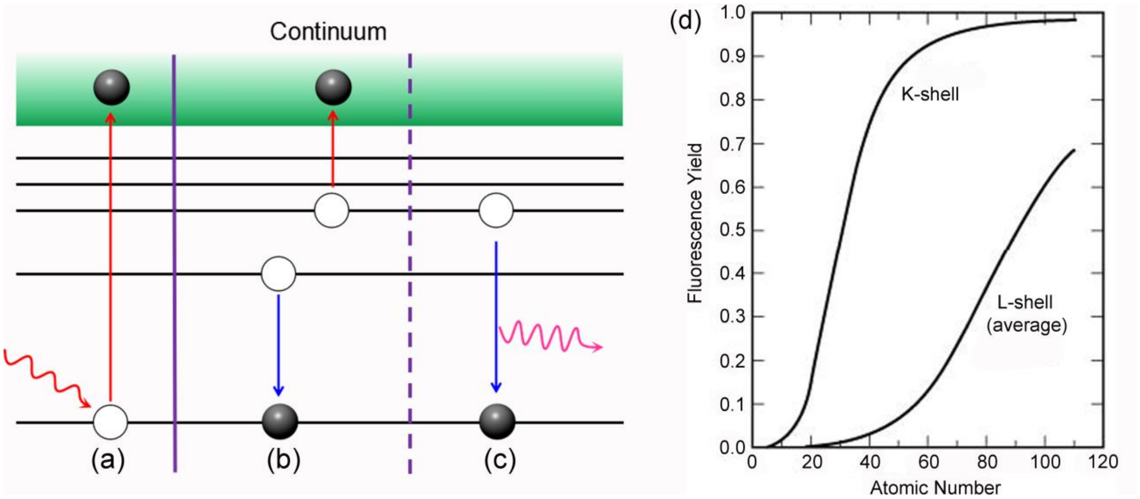

Figure 1-11 Schematic illustration of a core-electron excitation by X-ray and the subsequent de-excitation processes. (a) The presence of a photoelectron and a core-hole upon X-ray excitation. (b) Auger and (c) X-ray fluorescence de-excitation processes. (d) The fluorescence yield for K and L shells as a function of atomic number [92].

1.3.3 X-ray Excited Optical Luminescence

As mentioned above, Auger and X-ray fluorescence are two competing decay processes to refill the core-hole created by X-ray excitation, resulting in the presence of holes at a shallower level (**Figure 1-11b** and **11c**). Then a secondary Auger or X-ray fluorescence decay process at an outer shell would take place to refill these holes produced from the first decay process, and so forth. In semiconductors, a chain decay process occurs till the hole migrates to the top of VB, whereas, at the same time, the photoelectron excited by X-ray would move down to the bottom of CB, to form an electron–hole pair. This chain decay process is also called “thermalization” process (**Figure 1-12a**). After that, the recombination of electron–hole pair would possibly happen in the following three ways: (1) direct, (2) indirect, and (3) defect recombinations as shown in **Figure 1-12b**, **12c** and

12d, respectively. Meantime, the energy associated with these recombination processes can be released in either a non-radiative way as phonons, or a radiative manner as optical photons, which refers to the X-ray excited optical luminescence (XEOL). As for the latter, XEOL energy released in the first two recombination cases are called optical band gap emissions, whereas the case of radiative defect recombination would generate XEOL with an energy value lower than the band gap.

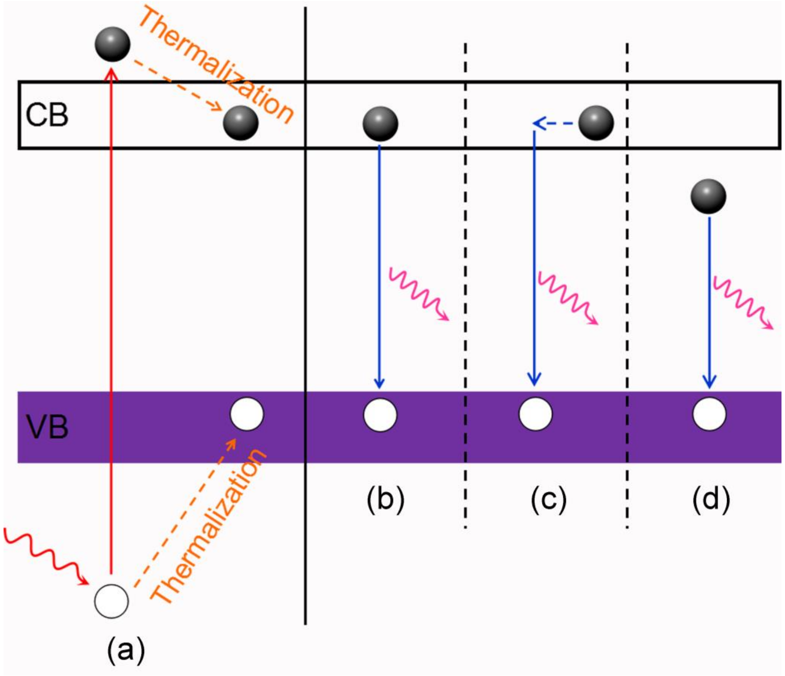

Figure 1-12 Schematic illustration of (a) core-electron excitation by X-ray and the subsequent thermalization process of photoelectron and hole to generate an electron–hole pair, and the recombination of electron–hole pair in (b) direct, (c) indirect and (d) defect manners.

It is worth noting that, unlike the conventional photoluminescence (PL) with the excitation of valence electron, the generation of XEOL is associated with the core-electron excitation as described above, although both PL and XEOL result from the final exciton recombination. Thus the generation of XEOL is element specific, and the optical luminescence yield (i.e., XEOL intensity variation) is also proportional to the modulation of absorption coefficient μ as a function of photon energy. Therefore, as the photon energy is tuned across the absorption edge of element of interest which contributes to luminescence generation, the as-obtained photoluminescence yield (PLY), also called optical XANES, can be collected as an extra XANES information comparable to other XANES detection modes, such as total electron yield (TEY) and fluorescence yield (FY) which will be discussed in Chapter 2. In experiment, XEOL in combination with XANES is used to unfold the luminescent mechanism of light-emitting materials with element and site specificities.

1.3.4 X-ray Emission Spectroscopy

As a complementary tool of XAS which probes the partial density of unoccupied electronic states of a material, X-ray emission spectroscopy (XES) measures the relevant partial density of occupied states. As demonstrated in **Figure 1-13**, once a core-hole is created by X-ray absorption, the XES process records the subsequent X-ray fluorescence decay with electronic transition from the VB states to the core-hole states following the dipole selection rule. As XES is directly related to the de-excitation process to fill the core-hole, thus XES is also an element specific technique resembling to XAS. Nevertheless, unlike XAS which is a first order process and involves only an electron excitation, XES contains both the electron excitation and the corresponding decay processes, hence XES is a second order optical process. In experiment, XES measures the intensity of emitted fluorescence as a function of emitted energy. As a photon-in and photon-out technique, XES has been widely utilized as a bulk-sensitive technique to measure both conducting and insulating samples due to the negligible charging effect.

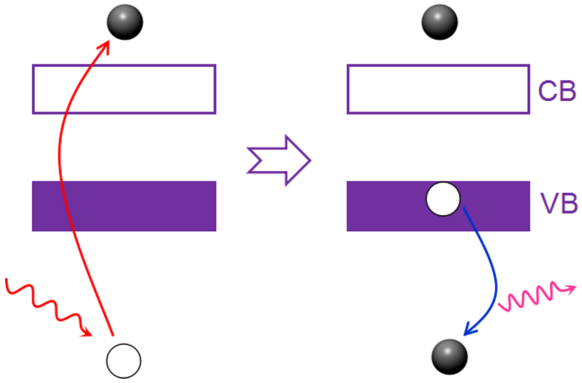

Figure 1-13 Schematic illustration of X-ray absorption and associated X-ray emission processes.

In general, XES can be divided into two categories based on their different excitation energies: non-resonant X-ray emission spectroscopy (NXES) and resonant inelastic X-ray scattering (RIXS). The latter is also called resonant X-ray emission spectroscopy (RXES), RIXS and RXES can be used interchangeably.

NXES involves an excitation energy which is well above the ionization threshold of core state of the element of interest, i.e., the core-electron is excited to the continuum with sufficient photon energy. In this case, NXES only records the filling process of core-hole by X-ray fluorescence decay of valence electron. It provides the partial density of occupied states of element measured. On the other hand, the excitation energy in RIXS measurement is tuned just above the ionization threshold of core state of the element of interest, i.e., the core-electron is only excited to the bound or quasi-bound state. Then the electron excitation and subsequent decay process are highly correlated for RIXS process (**Figure 1-14**), of which the intensity of RIXS can be theoretically described by the Kramer-Heisenberg equation (**Equation 1-13**) [93,94]:

$$I(h\nu_{in}, h\nu_{out}) \propto \sum_{f} \left| \sum_{m} \frac{\langle f \mid T \mid m \rangle \langle m \mid T \mid i \rangle}{E_m - E_i - h\nu_{in} - i\Gamma / 2} \right|^2 \cdot \delta(E_f + h\nu_{out} - E_i - h\nu_{in}) \qquad (1\text{-}13)$$

Where $h\nu_{in}$ and $h\nu_{out}$ are the respective energies of incident photon and emitted fluorescence X-ray, $|i\rangle$, $|m\rangle$ and $|f\rangle$ are the initial, intermediate and final states with their corresponding energies E_i, E_m and E_f, T represents the dipole transition operator, and Γ is the lifetime broadening for the intermediate state. Note that the intermediate state of RIXS process is the final state of XAS. As shown in **Equation 1-13**, the δ function term is independent of the intermediate state, and $i\Gamma / 2$ is the resonant term for radiation damping as $h\nu_{in} = E_m - E_i$ in the resonant situation. Therefore, RIXS is a coherent second-order process consisting of the X-ray absorption from $|i\rangle$ to $|m\rangle$, and the X-ray emission from $|m\rangle$ to $|f\rangle$. RIXS process takes place when the final state $|f\rangle$ is different as the initial state $|i\rangle$, whereas the inverse case denotes the resonant elastic X-ray scattering, i.e., it has the same final and initial states. Experimentally, a detection of XAS spectrum is always ahead of RIXS in order to set the excitation energy for RIXS measurement. As the excitation energy is tuned at different XAS feature, RIXS would provide a specific information about the electronic structure of that particular atomic site as different excitation energy used in XAS accords with a particular electronic transition. Generally, apart from the presence of the NXES and resonant elastic X-ray scattering features, d-d excitations and charge transfer features are also able to be resolved in RIXS spectrum [94,95].

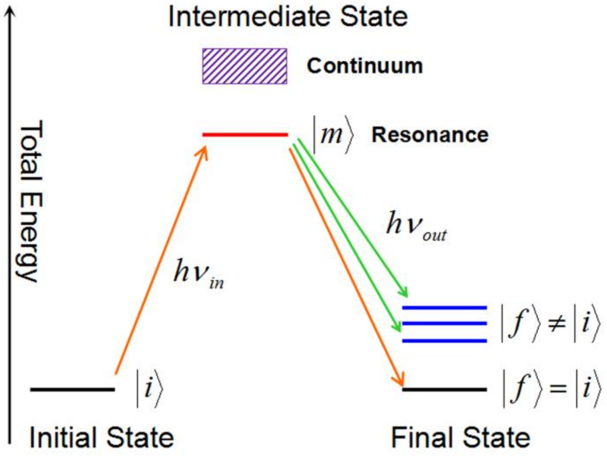

Figure 1-14 Schematic illustration of RIXS process.

1.4 Thesis Outline

The outline of the thesis is as follows. Chapter 1 provides a general introduction of TiO_2 nanomaterials, particularly TiO_2 nanotubes prepared by electrochemical anodization method, and an overview of SR together with a detailed description on the X-ray absorption, emission and related techniques. Chapter 2 describes the instrumentation of synchrotron facilities and the experimental methods. Chapter 3 discusses the morphology-dependent phase transition in anodic TiO_2 nanostructures as well as the anatase-to-rutile solid phase transition of TiO_2 nanotubes. Chapter 4 investigates the anion-doping effect on the electronic structure of TiO_2 nanotubes, where the N doping for the formation of black core-shell TiO_2 nanotube towards extraordinary photoabsorption as well as the self-doped F^- ions for the formation of TiO_2 defects, is mainly discussed. In Chapter 5, the optical, structural and chemical properties of TiO_2 nanotubes upon Pd decoration (coating) are thoroughly studied, where the synergistic effect between Pd and

TiO_2 is elucidated. Chapter 6 involves a mechanistic study of TiO_2 nanotube upon Na^+ uptake/release, of which the sodiation/desodiation effect on amorphous and anatase TiO_2 will be comparatively investigated. Chapter 7 includes the conclusions of the studies described in the thesis and a description of future work which shall be undertaken.

1.5 References

[1] X. B. Chen, L. Liu, P. Y. Yu, and S. S. Mao, *Science* **331**, 746 (2011).

[2] M. D. Ye, J. J. Gong, Y. K. Lai, C. J. Lin, and Z. Q. Lin, *J. Am. Chem. Soc.* **134**, 15720 (2012).

[3] J. J. Deng *et al.*, *ACS Nano* **9**, 5348 (2015).

[4] M. P. Liu et al., *Nature* **537**, 382 (2016).

[5] S. Gao, Y. Lin, X. C. Jiao, Y. F. Sun, Q. Q. Luo, W. H. Zhang, D. Q. Li, J. L. Yang, and Y. Xie, *Nature* **529**, 68 (2016).

[6] D. D. Zhu, J. L. Liu, and S. Z. Qiao, *Adv. Mater.* **28**, 3423 (2016).

[7] E. J. W. Crossland, N. Noel, V. Sivaram, T. Leijtens, J. A. Alexander-Webber, and H. J. Snaith, *Nature* **495**, 215 (2013).

[8] S. Lee, I. J. Park, D. H. Kim, W. M. Seong, D. W. Kim, G. S. Han, J. Y. Kim, H. S. Jung, and K. S. Hong, *Energy Environ. Sci.* **5**, 7989 (2012).

[9] G. K. Mor, K. Shankar, M. Paulose, O. K. Varghese, and C. A. Grimes, *Nano Lett.* **6**, 215 (2006).

[10] R. Asahi, T. Morikawa, T. Ohwaki, K. Aoki, and Y. Taga, *Science* **293**, 269 (2001).

[11] L. M. Wu, D. Bresser, D. Buchholz, G. A. Giffin, C. R. Castro, A. Ochel, and S. Passerini, *Adv. Energy Mater.* **5**, 1401142 (2015).

[12] K. T. Kim, G. Ali, K. Y. Chung, C. S. Yoon, H. Yashiro, Y. K. Sun, J. Lu, K. Amine, and S. T. Myung, *Nano Lett.* **14**, 416 (2014).

[13] J. Wei, J. X. Liu, Y. C. Dang, K. Xu, and Y. Zhou, *Adv. Mater. Res.***750**, 301 (2013).

[14] J. F. Ni, S. D. Fu, C. Wu, J. Maier, Y. Yu, and L. Li, *Adv. Mater.* **28**, 2259 (2016).

[15] A. Fujishima and K. Honda, *Nature* **238**, 37 (1972).

[16] K. Zhu, N. R. Neale, A. Miedaner, and A. J. Frank, *Nano Lett.* **7**, 69 (2007).

[17] H. Kim, M. Y. Cho, M. H. Kim, K. Y. Park, H. Gwon, Y. Lee, K. C. Roh, and K. Kang, *Adv. Energy Mater.* **3**, 1500 (2013).

[18] X. H. Lu, G. M. Wang, T. Zhai, M. H. Yu, J. Y. Gan, Y. X. Tong, and Y. Li, *Nano Lett.* **12**, 1690 (2012).

[19] Z. Liang, G. Y. Zheng, W. Y. Li, Z. W. Seh, H. B. Yao, K. Yan, D. S. Kong, and Y. Cui, *ACS Nano* **8**, 5249 (2014).

[20] G. Kim, C. Jo, W. Kim, J. Chun, S. Yoon, J. Lee, and W. Choi, *Energy Environ. Sci.* **6**, 2932 (2013).

[21] M. Z. Ge, C. Y. Cao, J. Y. Huang, S. H. Li, Z. Chen, K. Q. Zhang, S. S. Al-Deyabd, and Y. K. Lai, *J. Mater. Chem. A* **4**, 6772 (2016).

[22] M. Landmann, E. Rauls, and W. G. Schmidt, *J. Phys.: Condens. Matter* **24**, 195503 (2012).

[23] D. W. Su, S. X. Dou, and G. X. Wang, *Chem. Mater.* **27**, 6022 (2015).

[24] Y. H. Hu, *Angew. Chem., Int. Ed.* **51**, 12410 (2012).

[25] J. Li, T.K. Sham, Y. Ye, J. Zhu, and J. Guo, *J. Phys. Chem. C* **119**, 2222 (2015).

[26] J. Li *et al.*, *Chem. Mater.* **28**, 4467 (2016).

[27] Z. Luo, A. S. Poyraz, C. H. Kuo, R. Miao, Y. T. Meng, S. Y. Chen, T. Jiang, C. Wenos, and S. L. Suib, *Chem. Mater.* **27**, 6 (2015).

[28] A. Naldoni, M. Allieta, S. Santangelo, M. Marelli, F. Fabbri, S. Cappelli, C. L. Bianchi, R. Psaro, and V. Dal Santo, *J. Am. Chem. Soc.* **134**, 7600 (2012).

[29] Z. Wang *et al.*, *Adv. Funct. Mater.* **23**, 5444 (2013).

[30] M. Batzill, E. H. Morales, and U. Diebold, *Phys. Rev. Lett.* **96**, 026103 (2006).

[31] J. Hensel, G. M. Wang, Y. Li, and J. Z. Zhang, *Nano Lett.* **10**, 478 (2010).

[32] J. Wang, D. N. Tafen, J. P. Lewis, Z. L. Hong, A. Manivannan, M. J. Zhi, M. Li, and N. Q. Wu, *J. Am. Chem. Soc.* **131**, 12290 (2009).

[33] T. C. Jagadale, S. P. Takale, R. S. Sonawane, H. M. Joshi, S. I. Patil, B. B. Kale, and S. B. Ogale, *J. Phys. Chem. C* **112**, 14595 (2008).

[34] Z. D. Li, F. Wang, A. Kvit, and X. D. Wang, *J. Phys. Chem. C* **119**, 4397 (2015).

[35] S. Tosoni, D. F. Hevia, O. G. Diaz, and F. Illas, *J. Phys. Chem. Lett.* **3**, 2269 (2012).

[36] X. Chen, P. A. Glans, X. Qiu, S. Dayal, W. D. Jennings, K. E. Smith, C. Burda, and J. Guo, *J. Electron Spectrosc. Relat. Phenom.* **162**, 67 (2008).

[37] X. B. Chen and C. Burda, *J. Am. Chem. Soc.* **130**, 5018 (2008).

[38] J. C. Yu, J. G. Yu, W. K. Ho, Z. T. Jiang, and L. Z. Zhang, *Chem. Mater.* **14**, 3808 (2002).

[39] D. Li, H. Haneda, N. K. Labhsetwar, S. Hishita, and N. Ohashi, *Chem. Phys. Lett.* **401**, 579 (2005).

[40] A. Ghicov and P. Schmuki, *Chem. Commun.* 2791 (2009).

[41] M. S. Park, S. K. Kwon, and B. I. Min, *Phys. Rev. B* **65**, 161201 (2002).

[42] C. P. Cheney *et al.*, *Phys. Rev. Lett.* **112**, 036404 (2014).

[43] C. Diaz-Guerra, P. Umek, A. Gloter, and J. Piqueras, *J. Phys. Chem. C* **114**, 8192 (2010).

[44] T. Umebayashi, T. Yamaki, H. Itoh, and K. Asai, *J. Phys. Chem. Solids* **63**, 1909 (2002).

[45] N. Satoh, T. Nakashima, K. Kamikura, and K. Yamamoto, *Nat. Nanotechnol.* **3**, 106 (2008).

[46] M. Murdoch, G. I. N. Waterhouse, M. A. Nadeem, J. B. Metson, M. A. Keane, R. F. Howe, J. Llorca, and H. Idriss, *Nat. Chem.* **3**, 489 (2011).

[47] J. Y. Hwang, S. T. Myung, J. H. Lee, A. Abouimrane, I. Belharouak, and Y. K. Sun, *Nano Energy* **16**, 218 (2015).

[48] X. B. Chen *et al.*, *Sci. Rep.* **3**, 7, 1510 (2013).

[49] L. D. Li, J. Q. Yan, T. Wang, Z. J. Zhao, J. Zhang, J. L. Gong, and N. J. Guan, *Nat. Commun.* **6**, 5881 (2015).

[50] W. Chanmanee, A. Watcharenwong, C. R. Chenthamarakshan, P. Kajitvichyanukul, N. R. de Tacconi, and K. Rajeshwar, *J. Am. Chem. Soc.* **130**, 965 (2008).

[51] Y. C. Pu *et al.*, *Nano Lett.* **13**, 3817 (2013).

[52] J. Li, C. H. Liu, Y. F. Ye, J. F. Zhu, S. D. Wang, J. H. Guo, and T. K. Sham, *J. Phys. Chem. C* **120**, 4623 (2016).

[53] I. S. Cho, C. H. Lee, Y. Z. Feng, M. Logar, P. M. Rao, L. L. Cai, D. R. Kim, R. Sinclair, and X. L. Zheng, *Nat. Commun.* **4**, 1723 (2013).

[54] J. N. Nian and H. S. Teng, *J. Phys. Chem. B* **110**, 4193 (2006).

[55] D. Regonini, C. R. Bowen, A. Jaroenworaluck, and R. Stevens, *Mater. Sci. Eng., R* **74**, 377 (2013).

[56] C. J. Lin, W. Y. Yu, Y. T. Lu, and S. H. Chien, *Chem. Commun.* **45**, 6031 (2008).

[57] N. K. Shrestha, J. M. Macak, F. Schmidt-Stein, R. Hahn, C. T. Mierke, B. Fabry, and P. Schmuki, *Angew. Chem., Int. Ed.* **48**, 969 (2009).

[58] J. J. Gong, Y. K. Lai, and C. J. Lin, *Electrochim. Acta* **55**, 4776 (2010).

[59] C. K. Xu, P. H. Shin, L. L. Cao, J. M. Wu, and D. Gao, *Chem. Mater.* **22**, 143 (2010).

[60] T. Nonoyama, T. Kinoshita, M. Higuchi, K. Nagata, M. Tanaka, K. Sato, and K. Kato, *J. Am. Chem. Soc.* **134**, 8841 (2012).

[61] D. O. Scanlon *et al.*, *Nat. Mater.* **12**, 798 (2013).

[62] A. A. Melvin, K. Illath, T. Das, T. Raja, S. Bhattacharyya, and C. S. Gopinath, *Nanoscale* **7**, 13477 (2015).

[63] S. C. Zhu, S. H. Xie, and Z. P. Liu, *J. Am. Chem. Soc.* **137**, 11532 (2015).

[64] Y. B. Zhao, Y. F. Zhang, H. W. Liu, H. W. Ji, W. H. Ma, C. C. Chen, H. Y. Zhu, and J. C. Zhao, *Chem. Mater.* **26**, 1014 (2014).

[65] J. Li, L. J. Liu, and T. K. Sham, *Chem. Mater.* **27**, 3021 (2015).

[66] N. Satoh, T. Nakashima, and K. Yamamoto, *Sci. Rep.* **3**, 1959 (2013).

[67] V. N. Koparde and P. T. Cummings, *ACS Nano* **2**, 1620 (2008).

[68] A. S. Barnard and H. F. Xu, *ACS Nano* **2**, 2237 (2008).

[69] K. P. Kumar, K. Keizer, A. J. Burggraaf, T. Okubo, and H. Nagamoto, *J. Mater. Chem.* **3**, 1151 (1993).

[70] H. B. Li, X. C. Duan, G. C. Liu, and X. Q. Liu, *J. Mater. Sci.* **43**, 1669 (2008).

[71] S. H. Chang *et al.*, *ACS Nano* **8**, 1584 (2014).

[72] L. M. Wu, D. Buchholz, D. Bresser, L. G. Chagas, and S. Passerini, *J. Power Sources* **251**, 379 (2014).

[73] H. B. Wu, J. S. Chen, H. H. Hng, and X. W. Lou, *Nanoscale* **4**, 2526 (2012).

[74] D. N. Wang, L. J. Liu, X. L. Sun, and T. K. Sham, *J. Mater. Chem. A* **3**, 412 (2015).

[75] M. Assefpourdezfuly, C. Vlachos, and E. H. Andrews, *J. Mater. Sci.* **19**, 3626 (1984).

[76] V. Zwilling, E. Darque-Ceretti, A. Boutry-Forveille, D. David, M. Y. Perrin, and M. Aucouturier, *Surf. Interface Anal.* **27**, 629 (1999).

[77] D. Gong, C. A. Grimes, O. K. Varghese, W. C. Hu, R. S. Singh, Z. Chen, and E. C. Dickey, *J. Mater. Res.* **16**, 3331 (2001).

[78] O. K. Varghese, D. W. Gong, M. Paulose, C. A. Grimes, and E. C. Dickey, *J. Mater. Res.* **18**, 156 (2003).

[79] J. M. Macak, K. Sirotna, and P. Schmuki, *Electrochim. Acta* **50**, 3679 (2005).

[80] J. M. Macak, H. Tsuchiya, and P. Schmuki, *Angew. Chem., Int. Ed.* **44**, 2100 (2005).

[81] Y. X. Yin, Z. G. Jin, F. Hou, and X. Wang, *J. Am. Ceram. Soc.* **90**, 2384 (2007).

[82] M. Jarosz, A. Pawlik, J. Kapusta-Kolodziej, M. Jaskula, and G. D. Sulka, *Electrochim. Acta* **136**, 412 (2014).

[83] Y. Shin and S. Lee, *Nano Lett.* **8**, 3171 (2008).

[84] E. M. Rowe, and F. E. Mills, *Particle Accelerators* **4**, 211 (1973).

[85] Used with permission of the copyright holder: Copyright © EPSIM 3D/JF Santarelli, Synchrotron Soleil.

[86] H. Winick, Introduction and Overview. In *Synchrotron Radiation Sources: A Primer* edited by H. Winick (Stanford Synchrotron Radiation Lab. 1994)

[87] Adapted from: http://internal.physics.uwa.edu.au/~hammond/SyncRes/making-synchrotron-light.htm.

[88] T. K. Sham and M. L. Rivers, *Rev. Mineral. Geochem.* **49**, 117 (2002).

[89] Adapted from: http://physics.nist.gov/PhysRefData/XrayMassCoef/ElemTab/z78.html.

[90] F. de Groot, *Chem. Rev.* **101**, 1779 (2001).

[91] J. J. Rehr and R. C. Albers, *Rev. Mod. Phys.* **72**, 621 (2000).

[92] M. O. Krause and J. H. Oliver, *J. Phys. Chem. Ref. Data* **8**, 329 (1979).

[93] P. Glatzel *et al.*, *J. Am. Chem. Soc.* **126**, 9946 (2004).

[94] A. Kotani and S. Shin, *Rev. Mod. Phys.* **73**, 203 (2001).

[95] A. Augustsson, A. Henningsson, S. M. Butorin, H. Siegbahn, J. Nordgren, and J. H. Guo, *J. Chem. Phys.* **119**, 3983 (2003).

Chapter 2

2 Synchrotron Instrumentation

2.1 Synchrotron Facilities

2.1.1 Canadian Light Source (CLS)

Canadian Light Source (CLS) is Canada's national synchrotron light source facility located in Saskatoon, Saskatchewan, Canada. As a third-generation synchrotron source with a circumference of 171m, CLS has a 2.9 GeV storage ring operating at a current up to 500 mA, radio frequency of 500 MHz, and the emittance of 18.2 nm·rad. **Figure 2-1** shows the schematic layout of the CLS experimental hall. It includes 12 straights (9 available for insertion devices), 24 bending magnets, and over 40 possible beamlines. To date, 14 beamlines are in operation which provide photon energy range from Far infrared (IR) to hard X-ray [1].

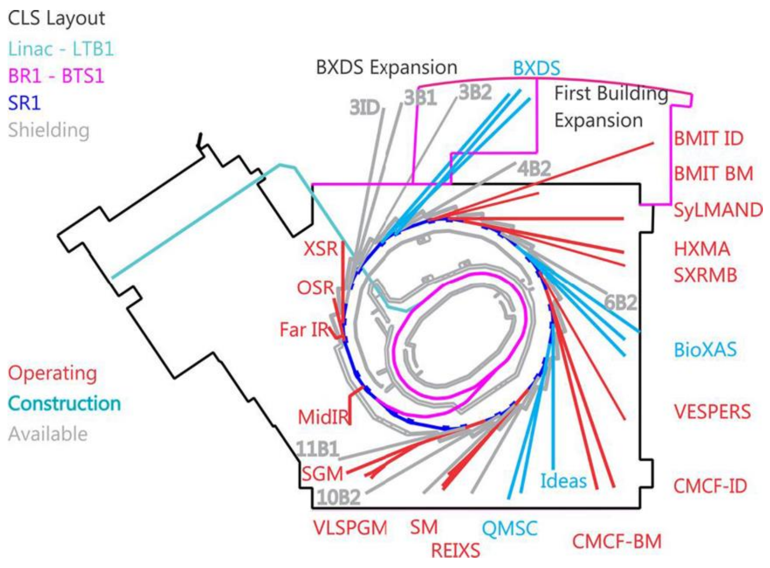

Figure 2-1 Schematic layout of the CLS Experimental Hall as of September, 2016 [1].

2.1.2 Advanced Light Source (ALS)

Advanced Light Source (ALS) is located at the Lawrence Berkeley National Laboratory (LBNL), Berkeley, California, USA. It is a third-generation synchrotron source with a circumference of ~200m. ALS has a 1.9 GeV storage ring operating at a current up to 500 mA, radio frequency of 500 MHz, and the emittance of 2.0 nm·rad. **Figure 2-2** shows the schematic layout of the ALS beamclock. It includes 17 insertion device beamlines, 18 bending magnets, and 9 superbend beamlines, of which 38 beamlines are currently in operation [2].

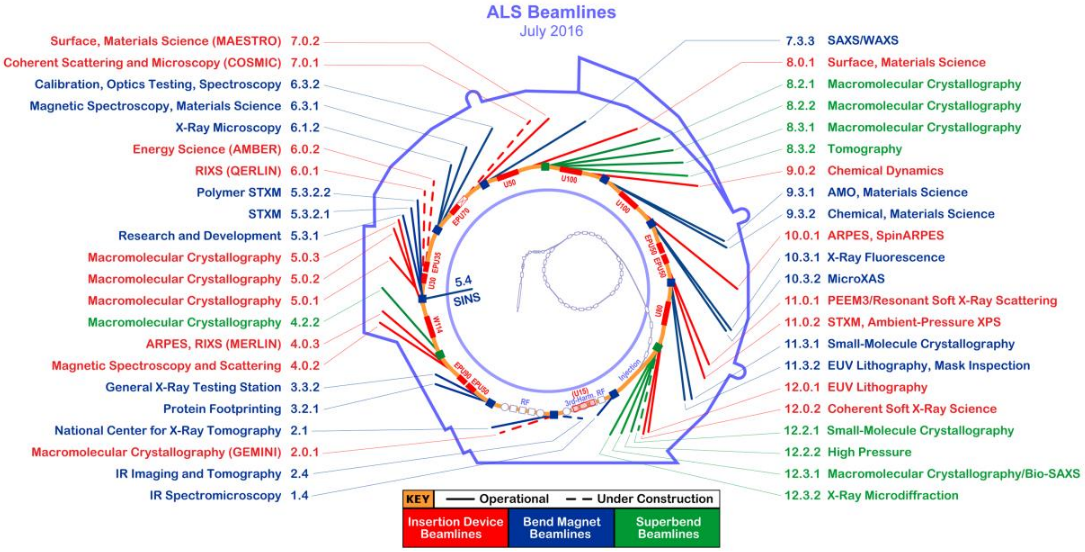

Figure 2-2 Schematic layout of the ALS beamclock as of July, 2016 [2].

2.2 Beamlines

2.2.1 SGM Beamline (11ID-1) at CLS

The high resolution Spherical Grating Monochromator (SGM) beamline (11ID-1) at CLS provides a very bright, highly monochromatic photon beam with a tunable energy between 250 and 2000 eV using the 45 mm planar undulator source. Three diffraction gratings are employed, of which the low, medium and high energy gratings correspond to the tunable energy ranges of 250 – 700 eV, 450 – 1250 eV, and 740 – 2000 eV, respectively. The typical operation condition at the SGM beamline include [3,4]: (1) a spot size (horizontal × vertical) of 1000 μm × 100 μm, (2) a wavelength of 62 – 6.5 Å, (3) an energy resolution ($E/\Delta E$) of ~5000 (below 1500 eV), (4) a flux (photons/s at 100 mA) of 4×10^{12} at 250 eV and ~1×10^{11} at 1900 eV. As shown in **Figure 2-3**, SGM contains two, in-line endstation areas (EA). Of which EA1 is built for X-ray photoemission and X-ray absorption studies, whereas EA2 allows for micro-focus experiments under ambient pressure conditions. XANES measurements at the Na K-, Ti L-, O K-, N K- and F K-edges together with XEOL experiments at the Ti L- and O K-edges of various specimens in this thesis were performed at EA1.

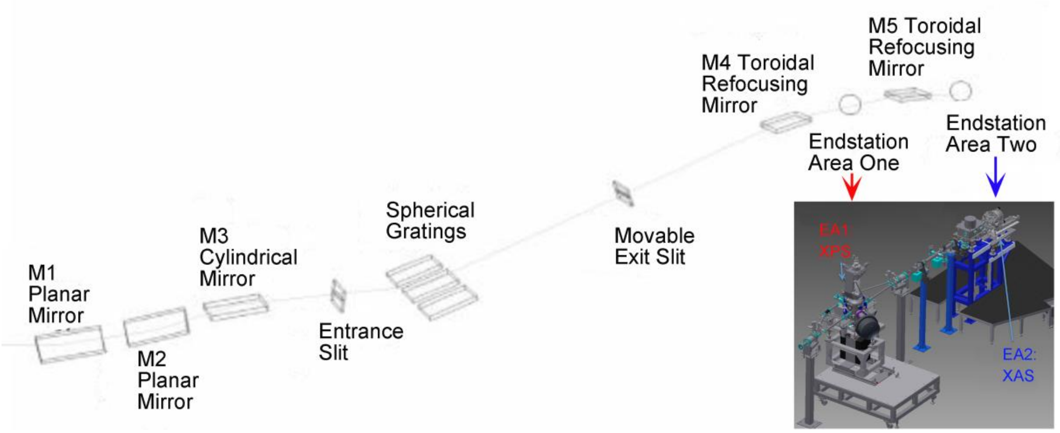

Figure 2-3 Layout of SGM beamline at CLS. The schematic view of two endstation areas at SGM is also shown [3,4].

2.2.2 SM Beamline (10ID-1) at CLS

The SpectroMicroscopy (SM) beamline (10ID-1) at CLS provides a high brightness, well resolved photon beam in the 130 – 2700 eV energy range with user-specified polarization (varying from an arbitrary inclined linear polarization to circular polarization) using a 75 mm generalized Apple II Elliptically Polarizing Undulator (EPU) source. The general SM beamline parameters contains a wavelength of 95 – 4.5 Å, and an energy resolution ($E/\Delta E$) of 3000 – 10000 [5,6]. As illustrated in **Figure 2-4**, SM beamline includes two microscopic endstations [6]: Scanning Transmission X-ray Microscope (STXM) and X-ray Photoemission Electron Microscope (X-PEEM). Whereas STXM coupled with a flux (at 100 mA) of ~10^8 photons/s in its 30 nm spot size, provides high quality imaging and spatially resolved spectroscopy with 30 nm spatial resolution, X-PEEM is a commercial X-ray photoemission electron microscope capable of better than 50nm spatial resolution with a flux (at 100 mA) as high as ~10^{12} photons/s in its 50 μm spot size. STXM experiments at the Ti L- and O K-edges in Chapter 3 were carried out at the STXM endstation.

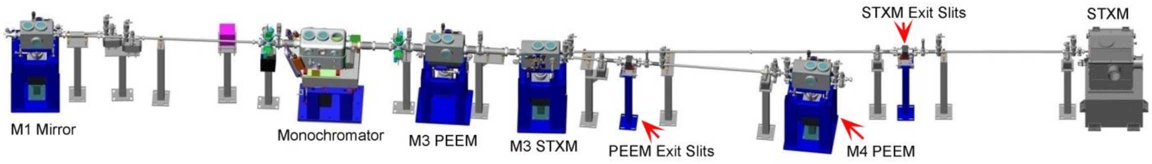

Figure 2-4 Layout of SM beamline at CLS [6].

2.2.3 SXRMB (06B1-1) at CLS

The Soft X-Ray Microcharacterization Beamline (SXRMB, 06B1-1) at CLS is a medium energy X-ray beamline with an energy range of 1.7 – 10 keV using the bending magnet source. **Figure 2-5** shows the two main XAFS and Microprobe endstations in the layout of SXRMB [7,8]. The common beamline specifications of these two endstations include a wavelength of 7.3 – 1.3 Å, and energy resolutions ($E/\Delta E$) of 3000 using InSb (111) crystal (energy range: 4 – 10 keV) and 10000 using Si (111) crystal (energy range: 1.7 – 4 keV). On the other hand, the flux and spot size of these two endstations are very different. Of which the XAFS endstation has a flux (at 100 mA) over 1×10^{11} photons/s in a spot size (horizontal × vertical) of ~1 mm × 4 mm, whereas the microprobe endstation holds a flux (at 100 mA) of 1×10^{9} photons/s with a spot size (horizontal × vertical) of ~10 μm × 10 μm. Specifically, SXRMB contains four endstations for general users: (1) solid state endstation is built for the bulk analysis of solid samples under high vacuum (10^{-7} torr); (2) microprobe endstation provides a 10 × 10 μm beamspot for use in elemental and chemical mapping experiment; (3) ambient table endstation is designed for bulk analysis of samples under ambient pressure, where liquid and solid in-situ experiments can be carried out; (4) highly energy XPS endstation (photon energy: 2000 – 10000) offers depth-profiling photoemission analysis by varying energies, particularly, it can provide information on surface and bulk properties of the material. In this thesis, XANES measurements at the Pd L_3-edge in Chapter 5 and the Ti K-edge in Chapter 6 were conducted at the solid state endstation of SXRMB.

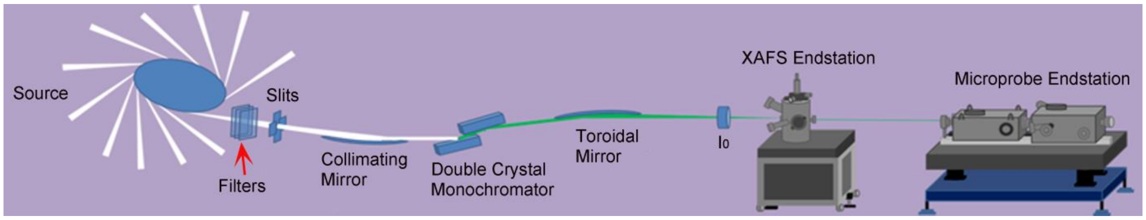

Figure 2-5 Layout of SXRMB beamline at CLS [7].

2.2.4 HXMA Beamline (06ID-1) at CLS

The Hard X-ray Micro-Analysis (HXMA) beamline (06ID-1) at CLS is a multipurpose hard X-ray beamline with an energy range of 5 – 40 keV using a 63 pole superconducting wiggler source. The general HXMA beamline parameters include [9]: (1) a spot size (horizontal × vertical) of 0.8 mm × 1.5 mm, (2) a wavelength of 2.5 – 0.3 Å, (3) an energy resolution ($E/\Delta E$) of 10000, and (4) a flux (at 100 mA) of 10^{12} photons/s at 12 keV. As illustrated in **Figure 2-6**, HXMA beamline consists of XAFS and XRD endstations [10]. Whereas XANES and EXAFS are the primary two types of experiments carried out at the XAFS endstation, XRD endstation is capable of performing various diffraction analysis such as high pressure powder XRD with diamond anvil cell, resonance X-ray diffraction and polarization analysis, grazing incidence small angle X-ray scattering, etc. XAFS (XANES and EXAFS) measurements at the Pd K-edge in Chapter 5 were performed at the XAFS endstation.

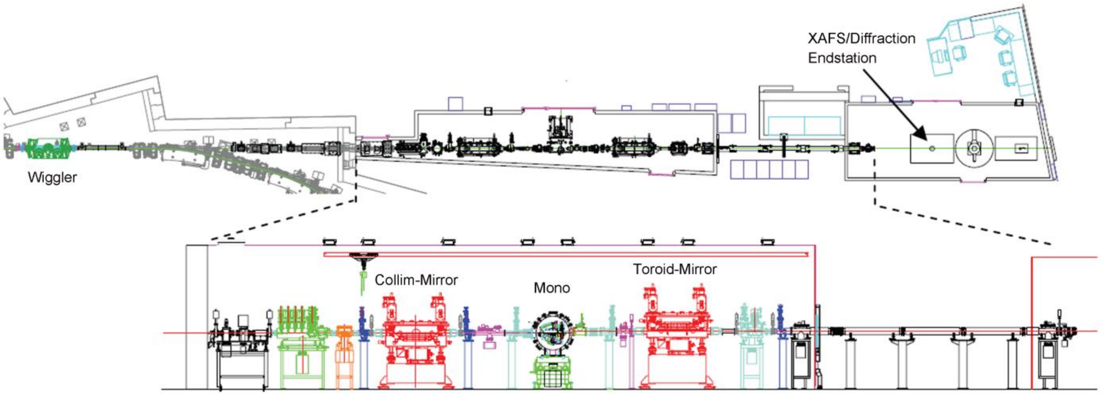

Figure 2-6 Layout of HXMA beamline at CLS [10].

2.2.5 Beamline 8.0.1 at ALS

The beamline 8.0.1 at ALS is a multipurpose soft X-ray beamline operating with an energy range of 80 – 1250 eV using a 5-cm period undulator (U5) source, which allows the variable first, third and fifth harmonics [11]. High resolution spherical grating monochromator operates with a resolving power ($E/\Delta E$) of 7000 with three interchangeable gratings (150, 380 and 925 lines/mm). The photon flux (at 400 mA) can reach from 10^{11} to 6×10^{15} photons/s depending on the resolution and photon energy used. **Figure 2-7** shows the schematic layout of beamline 8.0.1 at ALS [12]. Ti 2p RIXS measurements in Chapter 4 and 5 were conducted at the iRIXS endstation, which allows the measurement of soft X-ray absorption and emission spectroscopies as well as RIXS from solid samples with a dispersive grating spectrometer under ultra-high vacuum. The typical beam spot size (horizontal × vertical) at sample is 100 μm × 1000 μm.

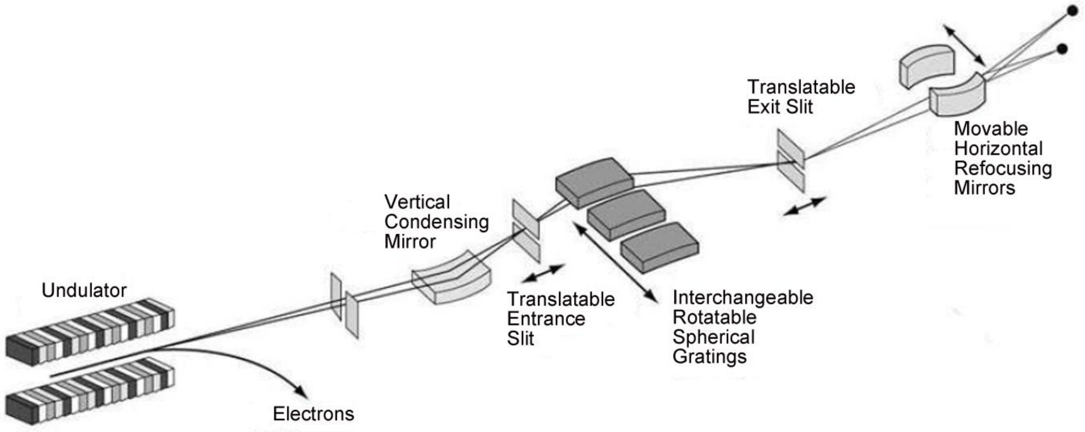

Figure 2-7 Layout of the beamline 8.0.1 at ALS [12].

2.2.6 Beamline Summary

The beamline facilities involved in this thesis are shown in **Table 2-1**.

Table 2-1 A summary of beamline facilities included in current thesis.

	Energy Range (eV)	Resolution ($E/\Delta E$)	Thesis Work
SGM at CLS	250-2000	5000	Ti $L_{3,2}$-, O K-, N K-, F K- and Na K-edges XANES and related XEOL analysis
SM at CLS	130-2700	3000-10000	Ti $L_{3,2}$- and O K-edges STXM-XANES analysis
SXRMB at CLS	1700-10000	3000-10000	Ti K- and Pd L_3-edge XANES analysis
HXMA at CLS	5000-40000	10000	Pd K-edge XAFS analysis
BL8.0.1 at ALS	80-1250	7000	Ti $L_{3,2}$-edge XANES and Ti 2p RIXS analysis

2.3 Detection Modes

The absorption of synchrotron light with matters follows the Beer-Lambert law (**Equation 1-4**): $I_t/I_0 = \exp(-\mu t)$, where I_0 and I_t are the intensity of incident and transmitted X-rays, respectively; μ is the absorption coefficient and t is the sample thickness. Clearly, absorption measurement with transmission mode is the most straightforward way as demonstrated in **Figure 2-8**. Nevertheless, the attenuation of light in probing materials constitutes a major limitation of sample thickness in order to use the transmission mode. Because if the sample is too thick, all incident photons will be absorbed. On the contrary, if the sample is too thin, the homogeneity of the sample (i.e., the sample thickness varies from region to region) will greatly affect the transmitted signal, resulting in inconsistent results. Hence, in order to collect synchrotron data with a good signal-to-noise ratio using the transmission mode, the ideal sample thickness should be close to the one-absorption-length, i.e., $t = 1/\mu$ (or $\mu t = 1$). In this case, the incident X-rays has already been attenuated by ~63.2 % as $I_t = I_0/e \approx 0.368\ I_0$. Therefore, the transmission mode is typically used in hard X-ray experiments for measuring sample with reasonable thickness, where the high energy of incident hard X-rays with its deeper penetration in materials compared to soft X-rays, allows the more practical sample thickness control. Alternatively, in most cases where the transmission mode is not feasible, total electron yield (TEY) and/or fluorescence yield (FY) as well as photoluminescence yield (PLY, or optical luminescence yield) detection modes as shown in **Figure 2-8** are used instead during synchrotron measurements. Specifically, as described in Chapter 1.3, when the energy of X-ray reaches the absorption threshold of the core level of an element of interest, a core electron can be excited and then a core–hole is created. Then de-excitation processes take place to annihilate the core–hole, resulting in the ejection of photoelectrons, Auger electrons and secondary electrons in the non-radiative way, or X-ray fluorescence emission in the radiative way. Since all these secondary processes are related to the probability of the presence of core–hole created by X-ray absorption, so that they are proportional to the absorption coefficient $\mu(E)$ of the element of measured.

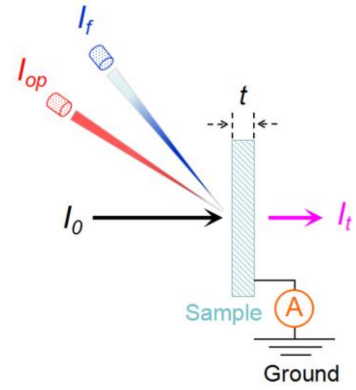

Figure 2-8 Illustration of synchrotron detection modes.

2.3.1 Total Electron Yield (TEY)

Total electron yield (TEY) is one of the detection modes in collecting XANES spectra, TEY collects all the ejected electrons (via core-hole excitation) from the sample and can be detected via monitoring the sample neutralization current (to ground, **Figure 2-8**) according to the **Equation 2-1**.

$$I_{TEY} = fcI_0(1-\mathrm{e}^{-\mu t}) \qquad (2\text{-}1)$$

Where I_{TEY} is the intensity of the TEY signal, f is the transmission efficiency for the detection of the electrons resulting from excitation and subsequent decay, c is a function proportional to photon energy, and $I_0(1–\mathrm{e}^{-\mu t})$ is the photons absorbed. TEY is a surface sensitive technique probing ~5 nm into the sample according to the universal curve of electron escape depth as shown in **Figure 2-9**. TEY is most desirable for soft X-ray measurement since soft X-ray has a shallow penetration depth and TEY does not suffer from thickness effect.

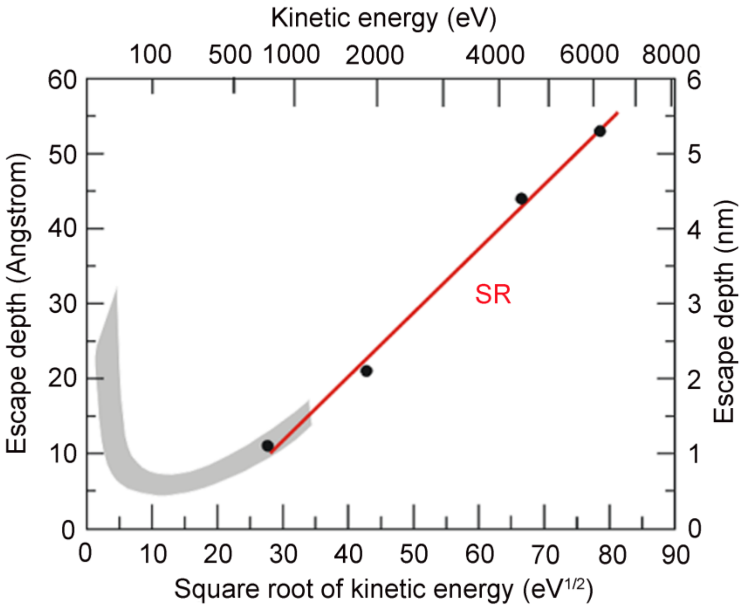

Figure 2-9 Recent electron escape depth via synchrotron radiation (SR) [13].

2.3.2 Fluorescence Yield (FY)

Fluorescence yield (FY), as another detection mode for measuring synchrotron spectra, however, is bulk sensitive compared with TEY because the attenuation length of fluorescence X-ray is comparatively larger; it can reach hundreds of nanometers or even microns depth. For example, the X-ray attenuation length of TiO_2 is shown in **Figure 2-10**, of which the attenuation length before Ti L-edge is ~1 μm while a lower value of ~200 nm is for the O K-edge, and the attenuation length before Ti K-edge can reach as high as ~12 μm. Similarly, the intensity of FY (I_f, **Figure 2-8**) follows the **Equation 2-1** as shown above whereas f is related to the probability of fluorescence detection instead of electrons in TEY. Normally, microchannel plates (MCPs) are used for FY detection, meanwhile, the prevention of electrons from impinging on the MCPs can be carried out by applying a large negative voltage to the first channel plate so that only fluorescence X-rays will be collected. An electron cascade will be created when X-ray photons enter the MCPs which can be detected as a current. FY can be recorded as a total-yield and/or partial-yield using a monochromator for the energy window selection of fluorescence X-ray.

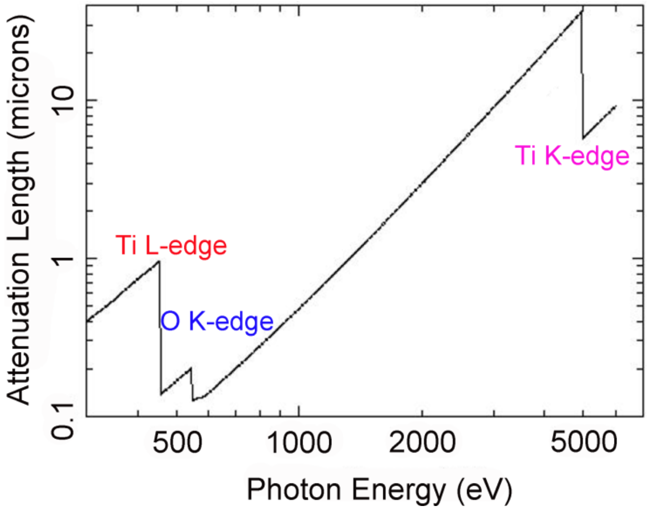

Figure 2-10 X-ray attenuation length of TiO_2 (density = 3.893 g cm^{-3}) at the Ti L-, O K, and Ti K-edges with an incident angle of 90 degree [14].

2.3.3 Photoluminescence Yield (PLY)

If the material is light-emitting, then a charge-coupled device (CCD) detector can be employed to collect the photoluminescence yield (PLY). Since PLY measures the yield of ejecting optical photons resulting from fluorescence X-ray with its favorable energy transfer in optical channels, thus the detection depth of PLY and FY are more or less comparable. Likewise, the intensity of optical luminescence (I_{op}, **Figure 2-8**) follows the **Equation 2-1** as indicated above whereas f is related to the probability of optical photons detection instead of electrons in TEY and fluorescence in FY. As the measurement of PLY accords with the simultaneous collection of energy-dependent XEOL spectra with a continuous energy scan across the absorption edge of interest, hence, PLY is also a reflection of XEOL intensity variation as a function of photon energy. In addition, like the case of FY detection mentioned above, PLY also can be measured as a total-yield and/or partial-yield using a monochromator or spectrophotometer for the wavelength window selection of photoluminescence.

2.4 References

[1] Adapted from: http://www.lightsource.ca/beamlines.html.

[2] Adapted from: https://www-als.lbl.gov/index.php/beamlines/beamlines-directory.html.

[3] Adapted from: http://sgm.lightsource.ca/.

[4] T. Regier, J. Paulsen, G. Wright, I. Coulthard, K. Tan, T. K. Sham, and R. I. R. Blyth, *AIP Conf. Proc.* **879**, 473 (2007).

[5] K. V. Kaznatcheev, C. Karunakaran, U. D. Lanke, S. G. Urquhart, M. Obst, and A. P. Hitchcock, *Nucl. Inst. Meth.* **582**, 96 (2007).

[6] Adapted from: http://exshare.lightsource.ca/sm/Pages/SM-Home.aspx.

[7] Adapted from: http://sxrmb.lightsource.ca/.

[8] Y. F. Hu *et al.*, *AIP Conf. Proc.* **1234**, 343 (2010).

[9] Adapted from: http://exshare.lightsource.ca/hxma/Pages/HXMAHome.aspx.

[10] D. T. Jiang, N. Chen, L. Zhang, K. Malgorzata, G. Wright, R. Igarashi, D. Beauregard, M. Kirkham, and M. McKibben, *AIP Conf. Proc.* **882**, 893 (2007).

[11] J. J. Jia *et al.*, *Rev. Sci. Instrum.* **66**, 1394 (1995).

[12] Adapted from: http://www-als.lbl.gov/als/als_users_bl/8.0.1-Overview.pdf.

[13] J. Zegenhagen, *Eur. Phys. J. Appl. Phys.* **70**, 20701 (2015).

[14] Adapted from: http://henke.lbl.gov/optical_constants/atten2.html.

Chapter 3

3 Unfolding the Solid Phase Transition of Anodic Titania Nanostructures

3.1 Introduction

In nature, TiO_2 polymorphs include anatase, rutile and brookite, of which anatase and rutile are most common and they are often the subjects of investigation for technological applications due to their photoactivity among others [1-4]. Between the two, anatase TiO_2 has been widely accepted as the desired phase in photocatalysis due to its slower charge recombination kinetics [5], higher charge carrier mobility [6] and many other merits over rutile [7-10], while the latter shows its superior activity in photocatalytic reduction reactions [8,11]. In fact, more often than not, anatase-rutile mixed phase with a proper ratio can deliver the synergistic efficiency in photocatalysis; the notion of mixed phase has led to a commercialized product (Degussa P25) and drives further studies on mixed-phase TiO_2 toward photo-performance optimization [12,13].

To engineer the desired anatase/rutile (mixed) phase for a specific application, the anatase-to-rutile solid phase transition of TiO_2 has been extensively investigated due to the fact that irreversible anatase-to-rutile transition (ART) can be initiated by annealing at elevated temperature [4,14,15]. The reported ART temperature varies from 400 ℃ to 1200 ℃ which is affected by numerous factors [16]. Of these, size is a factor for the ART of TiO_2. The general view of the size dependence of nanocrystals is that the phase transition temperature decreases with the reduction of grain size due to the direct correlation to the surface to volume ratio [17-19]. In the case of nano-TiO_2, same trend of size dependence to ART has been found [20,21] and the correlation between irreversible

*A version of this chapter has been published in *Chem. Mater.* **27**, 3021 (2015) and *J Phys. Chem. C* **120**, 22079 (2016).

ART temperature and size is hypothesized [22]. However, the grain growth of anatase and phase transition to rutile are two competing processes under thermal annealing. Because the large surface area of anatase nano-TiO_2 will either be the driving force for ART due to the high surface energy and rich interfaces for rutile nucleation, or result in the grain size growth of anatase by the coalescence of smaller neighboring grains [21,23]. Therefore, upon annealing at a high temperature, rutile nuclei will form among some of the grains whereas others will grow to the larger size grains to slow down the ART process; *i.e.*, that ART will be encumbered by the grain growth and thus increasing the ART temperature. In addition, recent reports show that the ART of TiO_2 nanocrystal (NC) exhibits an anisotropic behavior [15,24], in which the exposure of the thermodynamically unstable {001} facets of anatase TiO_2 NC would decrease the energy barrier for rutile nucleation, thus favoring the ART process. Particularly, Zhao et al. [24] pointed out that the ART temperature can be reduced by ~100 ℃ when the {001} facet percentage in anatase TiO_2 NC increases from 32 % to 63 %.

Nevertheless, unlike the size and crystal orientation dependence, research on the morphology-dependent ART study of anatase TiO_2 has only received sporadic attention. In particular, the mechanism of ART in the one-dimensional (1D) TiO_2 nanostructures remains elusive, although these 1D structures are usually regarded as the more preferable morphologies for the application of TiO_2 due to their unique architecture and relevant properties [25,26]. As a typical case, highly ordered TiO_2 nanostructure created by electrochemical anodization possesses a particularly high surface area by having the ordered tubular structure. Hence, great efforts have been made to reveal the anodic TiO_2 growth mechanism in order to achieve suitable morphology for various platforms [27,28], yet, only a few reports involving the ART of anodic TiO_2 are available [29-31]. In fact, literature results are inconclusive due to the lack of proper techniques which allow to reveal the spatial locations of co-existing anatase and rutile phases. Therefore, ART of anodic TiO_2 nanostructure certainly needs further work with the use of more advanced techniques, especially those with high spatial resolution.

Herein, in this chapter, we have synthesized two types of anodic TiO_2 nanostructures to investigate their morphology-dependent ART behaviors using the state-of-the-art synchrotron X-ray techniques, hence revealing the associated ART mechanism. A hierarchical TiO_2 nanostructure with close-ended nanotube (NT) layer on the bottom and a nanograss (NG) layer covered on the top was firstly prepared by an extended electrochemical anodization method. XANES analysis at the top NG and bottom NT layers, respectively, has conducted to look into the ART process with morphology dependence. Thereafter, a NT specimen (without the presence of NG) with an anatase-rutile mixed phase structure was fabricated to pinpoint the ART of highly ordered TiO_2 NT. Accordingly, scanning transmission X-ray microscopy (STXM) with its high spatial resolution was employed to unfold the associated anatase/rutile phase distribution. These results will help fulfill the promising applications with the fabrication of efficient TiO_2 nanostructures with desired morphology and phase component(s).

3.2 Experimental Section

3.2.1 Titania Nanostructure Synthesis

Hierarchical TiO_2 nanostructure was fabricated by an extended electrochemical anodization process using a custom-made two-electrode cell, Ti metal foil (Goodfellow, 0.1 mm thick) with a surface area of 2 cm × 0.5 cm was used as the anode for TiO_2 nanostructure growth, and a Pt wire was used as the cathode at a distance of ~2 cm from the anode. As fluoride is a necessity for TiO_2 nanotubular structure formation [28], electrolyte with a composition of 0.25 wt. % NH_4F (ACS, 98.0 % min, Alfa Aesar) and ethylene glycol was used. In order to obtain the nanograss layer, 50 V (Hewlett-Packard−6209B DC power supply) was applied to the electrodes with an extended anodization duration of 72 hours to allow the secondary anodization of nanotube to nanograss. Subsequently, the anodized Ti film was rinsed with ethanol for several times to remove the leftover electrolyte and dried with pure nitrogen gas. The anodic TiO_2 layers at both sides were easily removed from the Ti substrate and were divided into four pieces. One was kept as the original form, and the other three were annealed at 550 ℃, 850 ℃ and 900 ℃, respectively, for 2 hours using a furnace under the ambient condition. The ramping rates for all three annealing processes were 5 ℃ min^{-1}. The top and bottom sides of nanostructures with post-annealing at 550 ℃, 850 ℃ and 900 ℃ were denoted as nanograss-550 (NG500), nanotube-550 (NT550), nanograss-850 (NG850), nanotube-850

(NT850), nanograss-900 (NG900) and nanotube-900 (NT900), respectively. The as-prepared sample was denoted as as-prepared-nanograss (APNG) and as-prepared-nanotube (APNT).

To further look into the ART behavior of TiO_2 NT itself, i.e., without the interference of NG, highly ordered TiO_2 NTs were synthesized by a two-step electrochemical anodization process using the same two-electrode assembly as described above. Likewise, a pure Ti foil with a size of ~1 cm × 2 cm was used as the anode after ultrasonically rinsed with de-ionized (DI) water and ethanol, the cathode was a platinum wire. The electrolyte was composed by 0.3 wt % NH_4F, 2 vol % DI water and ethylene glycol. First, Ti was anodized under 50 V at room temperature (~20 ℃) for 4 h. Then the firstly anodized Ti foil was ultrasonically rinsed in 1 M HCl to remove the top NT layer. Next, the refreshed Ti foil was cleaned by DI water and ethanol for several times and used as the anode for the following anodization. At the second step, the refreshed (first-layer-removed) Ti foil was anodized for 30 min under 50 V using the same but fresh electrolyte. Afterwards, the as-grown NTs (AGNT) on the Ti substrate was rinsed with DI water and then ethanol several times to remove the remaining electrolyte on the NT surface. The AGNT was cut into 6 pieces. One of which was kept as was (AGNT), the other five were annealed at 500 ℃, 700 ℃, 750 ℃, 800 ℃ and 900 ℃ for 2 h under ambient air to induce crystallization, henceforth denoted as NT500, NT700, NT750, NT800 and NT900, respectively.

3.2.2 Material Characterization

Scanning electron microscopy (SEM, LEO 1540XB) and X-ray diffraction (XRD, Rigaku RU-200BVH, Co Kα radiation with $\lambda = 1.7892$ Å) were employed to track the morphology and crystal structure of various TiO_2 nanostructures. Synchrotron experiments were carried out at the Canadian Light Source (CLS, Saskatoon, SK, Canada). For the hierarchical NG-NT TiO_2 structure, the top (NG) and bottom (NT) sides of each sample were mounted on carbon tapes separately and attached to the sample holder with an angle of 45 degree toward the incident photon beam. The Ti $L_{3,2}$-edge and O K-edge XANES experiments were performed at the Spherical Grating Monochromator (SGM) beamline with a high resolution ($E/\Delta E$) over 5000 and an energy range of 250 −

2000 eV [32]. Two detection modes, total electron yield (TEY) and partial fluorescence yield (PFY), were used to collect absorption spectra. Whereas the TEY is surface-sensitive by measuring the specimen current, bulk-sensitive PFY collects the fluorescence X-rays using four silicon drift detectors. All spectra were normalized to the incident photon flux.

For the highly ordered TiO_2 NT specimen, Ti $L_{3,2}$-edge and O K-edge XANES measurements were also collected at the SGM beamline ($E/\Delta E > 5000$) [32]. In order to perform STXM analysis, a NT750 lamella (as-grown NTs annealed at 750 ℃) was prepared by the focused-ion beam (FIB) milling and thinning processes. The Zeiss 1540XB FIB/SEM at the Western Nanofabrication Facility was used to extract and thin the specimen. A gallium ion beam of 30 kV and beam currents ranging from 10nA to 200 pA were used for excavation and polishing. The sample was first made electrically conductive by coating it with 20 nm osmium metal via plasma deposition. Prior to FIB milling around the area of interest, a sacrificial band of platinum was deposited on the surface, first by electron beam then by focused ion beam decomposition of a platinum metal-organic precursor. The lamella was removed from the substrate using the Ascend nano-manipulator, a FIB-milled molybdenum end-effector grid. Once removed, the lamella was welded to the end-effector by electron beam driven platinum chemical vapor deposition (CVD). The final thinning and polishing was performed after lift-out to eliminate re-deposition artifacts.

STXM characterization was conducted at the soft X-ray spectromicroscopy (SM) beamline. The design and working principles of STXM have been reported elsewhere [33]. Briefly, a 25 nm outermost-zone zone plate (CXRO, Berkeley Lab) with a 30 nm diffraction-limited spatial resolution was applied to focus the monochromatic X-ray beam to a 30 nm spot on the region of interest (ROI) of sliced NT750 lamella. Then the selected ROI was raster-scanned to generate the absorption image a pixel at a time via recording the incident and transmitted X-rays simultaneously. A 500 l/mm plane grating monochromator (PGM) was employed for the STXM measurements at the Ti $L_{3,2}$-edge and O K-edge of the sliced NT750 lamella. Before the NT750 characterization, the incident X-ray beam was moved to an empty hole of the STXM sample plate, and then the incident photon fluxes (I_0) were tuned to be ~19 MHz at 475 eV with exit slits at 25/25 µm (dispersive/non-dispersive) for the Ti $L_{3,2}$-edge, and at 525 eV with exit slits at 23/23 µm for the O K-edge. The energy calibration was done by tracking the O K-edge XANES of gas phase CO_2, which was calibrated to its literature value at 535.4 eV [34,35]. During the test, the STXM transmission mode was applied, and two regions of interest (ROI) from the same sliced NT750 lamella with their different sizes were selected for STXM characterization. Of which a large size of ~2.2 µm × 7 µm and a small size of 1.5 µm × 1.5 µm were chosen. Image sequence (stack) scans over a range of photon energies were attained at both the Ti $L_{3,2}$-edge and O K-edge for the larger ROI but only at the Ti $L_{3,2}$-edge for the smaller ROI. For the Ti $L_{3,2}$-edge, image stacks covered an energy range of 452-475 eV with a fine energy step of 0.15 eV around the fine structures and a coarser energy step of 0.5 eV at the pre-edge and post-edge regions. An energy range of 526-553 eV with the finest energy size of 0.2 eV was used to compile the O K-edge image stacks. Typically, the scan area of ROI included some blank regions (without sample absorption) for I_0 measurement. The pixel sizes of 45 nm for the large ROI and 25 nm for the small ROI together with 1 ms dwell time per pixel were utilized for each image of a stack scan. A aXis2000 software package was used for STXM data analysis [36]. XANES from ROIs were extracted from image stacks using image mask. More details of STXM data analysis were reported elsewhere [34,35,37,38].

3.2.3 STXM Data Analysis

Optical Density and Attenuation Length. Since the thickness of sliced NT750 lamella is controlled to be below 100 nm, which is smaller than the X-ray attenuation length of both anatase and rutile TiO_2 (**Figure 3-1**), thus thickness effect due to absorption saturation can be ruled out in the STXM analysis. Accordingly, the STXM optical density (OD), also called absorbance (A), can be calculated using the Beer-Lambert law (**Equation 3-1**):

$$OD = A = -\ln T = \ln\left(\frac{I_0}{I}\right) = \mu t = \sigma\rho t \qquad (3\text{-}1)$$

Where T is the transmittance, I_0 (recorded from the blank region of ROI without X-ray absorption) and I are the incident and transmitted X-ray photon flux (photons/s), respectively, μ is the energy dependent absorption coefficient (cm^{-1}), σ is the energy dependent mass absorption cross section (cm^2/g), ρ is the sample density (g/cm^3), and t is the sample thickness.

Attenuation length (1/e) is defined when $\mu t = 1$ in Equation 3-1. Thus $I/I_0 = e^{-1} = 0.363$ is derived. Hence the attenuation length describes that the incident X-ray photon flux would be attenuated to 36.3 % with a sample thickness of $t = 1 / \mu$, which is also called the one absorption length.

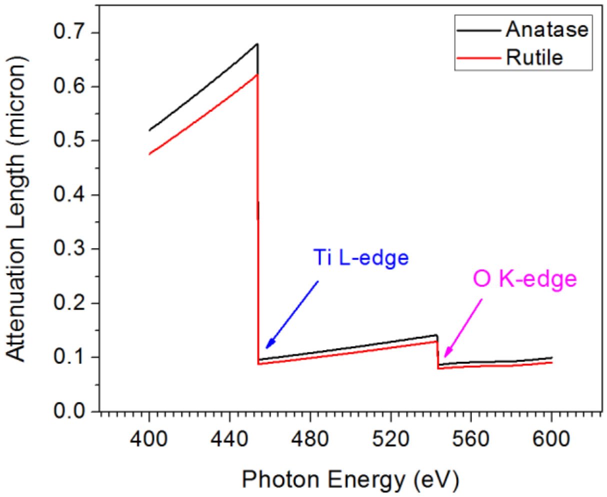

Figure 3-1 Calculated attenuation length of X-rays as a function of photon energy for bulk anatase TiO_2 (density = 3.89 g cm^{-3}; incident angle = 45 degree) and bulk rutile TiO_2 (density = 4.25 g cm^{-3}; incident angle = 45 degree). The calculation procedure can refer to [39].

Chemical Mapping. First, alignments, based on two dimensional Fourier transform cross-correlation technique, among all images as a function of photon energy from each image stack were performed to make sure that the chemical features from certain spatial location could be accurately superimposed from one image to the other. Next, by normalizing to the incident photon flux (I_0) spectra (as a function of photon energy) extracted from a black region on the same stack without sample X-ray absorption, the aligned image stacks were converted to optical density image stacks. Hence, chemical mapping at the Ti $L_{3,2}$-edge and O K-edge were generated by stack fitting with anatase and rutile XANES spectra as references. A colorful STXM map including multiple components was produced by superimposing their respective STXM map. The STXM mapping principle computes a least squares fit of optical density to a linear combination of reference spectra for each chemical component based on **Equation 3-2** shown below:

$$\mathrm{OD}_{(x,y,E)} = \mathrm{Constant}_{(x,y)} + \sum_{i} \mathrm{OD}_{i(x,y,E)} \qquad (3\text{-}2)$$

Where $\mathrm{OD}_{(x,y,E)}$ is the total optical density at each pixel of an image at energy E, $\mathrm{OD}_{i(x,y,E)}$ is the optical density at each pixel of an image at energy E of component i.

3.3 Results and Discussion

3.3.1 XANES Analysis of Hierarchical TiO_2 Nanostructure

SEM images of the as-prepared sample (**Figure 3-2a** and **2b**) show a hierarchical nanostructure with a NG layer on the top (a thickness of ~10 µm, inset of **Figure 3-2b**) and an ordered NT layer underneath (a thickness of ~70 µm), resulting in a vast surface area. Magnified SEM images (**Figure 3-2c**) at the top, side and bottom of as-prepared nanostructure show NG with a diameter of tens of nanometers covering the top surface, whereas rippled NTs are underneath with a close-ended pattern at the bottom side. It is worth mentioning that the NG and NT layers are spatially connected and tightly packed (inset of **Figure 3-2b**), and this hierarchical structure is very stable thus no observable change of its morphology is found under sonication for 10 min. After thermal-annealing at 550 ℃, 850 ℃ and 900 ℃ for 2 hours, the morphology evolution of the hierarchical nanostructure is from top-NG − bottom-NT (close-ended, 550 ℃, **Figure 3-2d**) structure to a compact film with a porous structure (850 ℃, **Figure 3-2e** and 900 ℃, **Figure 3-2f**). Of these, the top NG shrinks first and then melts to gain grain size whereas the NT structure persists first and then totally collapses to a bulk film, suggesting phase transformation is induced by high temperature annealing [40,41].

The Ti $L_{3,2}$-edge of TiO_2 has been investigated both experimentally and theoretically [41-43]. **Figure 3-3a** shows the surface sensitive XANES (TEY) associated with the local structure at the Ti site of the hierarchical TiO_2 nanostructures at both the NT and the NG layers in comparison with anatase and rutile standards. Of these, peaks a and c are electron transitions to Ti $3d\text{-}t_{2g}$ states from Ti $2p_{3/2}$ and $2p_{1/2}$ states, respectively, whereas the same core-electron transitions to Ti $3d\text{-}e_g$ states result in the features b and d. Further peak splitting into b_1 and b_2 is due to local distortion of Ti site from octahedral structure [43] as well as the inclusion of non-local distortion effect [44,45]. The intensity ratio of b_1 compared to b_2 (I_{b1}/I_{b2}) indicates the different local symmetry around the Ti atom and

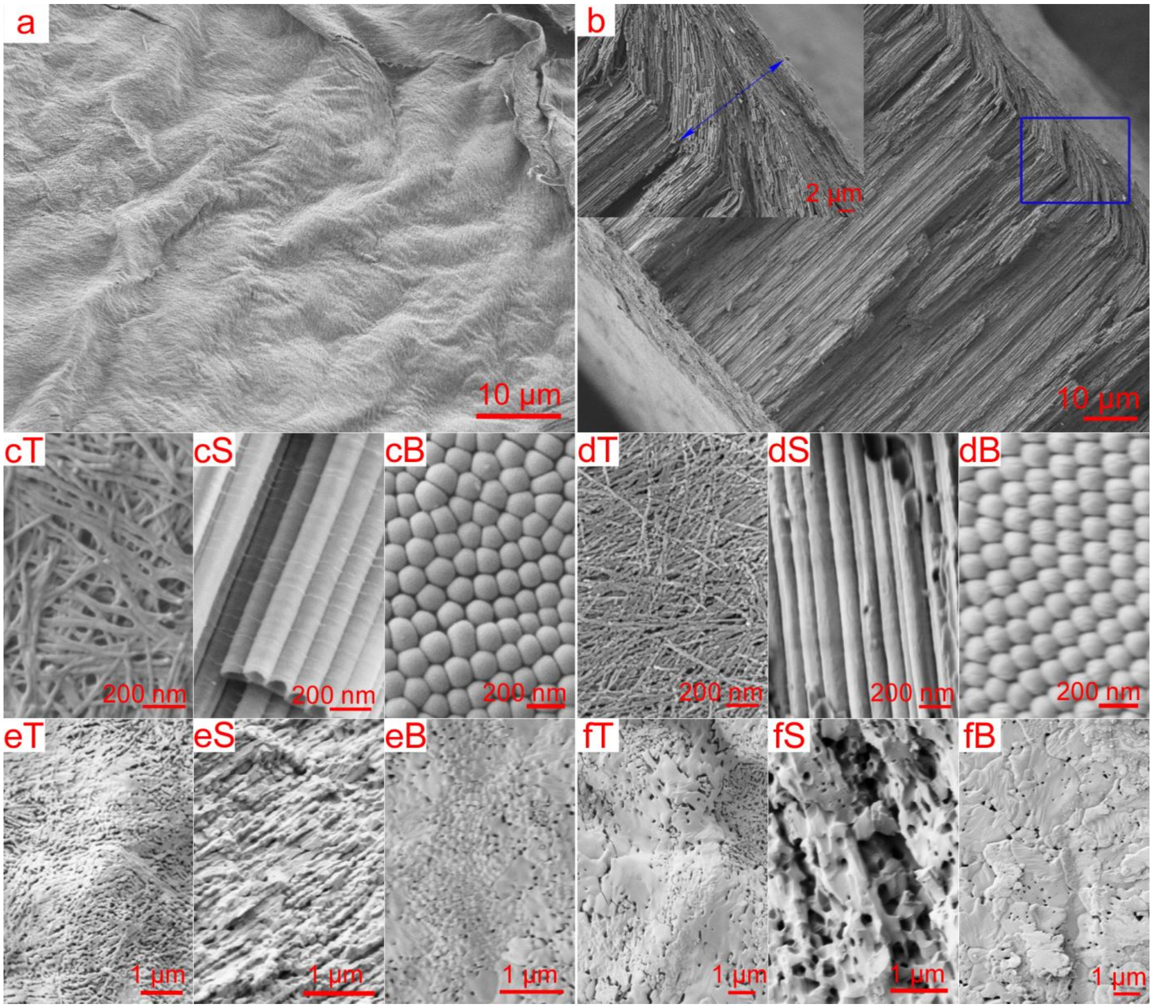

Figure 3-2 (a) Top and (b) side SEM images of as-prepared TiO_2 hierarchical nanostructure. Top, side and bottom (T, S, B) SEM images of TiO_2 hierarchical nanostructures obtained *via* as-prepared (c) and thermal annealing at 550 ℃ (d), 850 ℃ (e) and 900 ℃ (f); A magnified SEM image of the nanograss layer is shown in the inset of (b).

can be used as the fingerprint to differentiate between crystal structures. For example, $I_{b1}/I_{b2} > 1$ indicates the anatase-dominant TiO_2 with a D_{2d} local symmetry whereas $I_{b1}/I_{b2} < 1$ demonstrates the D_{2h} symmetry of rutile-dominant TiO_2. Meanwhile, the trend: $(I_{b1}/I_{b2})_{\text{rutile standard}} < (I_{b1}/I_{b2})_{\text{structure}} < (I_{b1}/I_{b2})_{\text{anatase standard}}$, usually shows the multiphase (anatase-rutile mixture) nature of the testing structure.

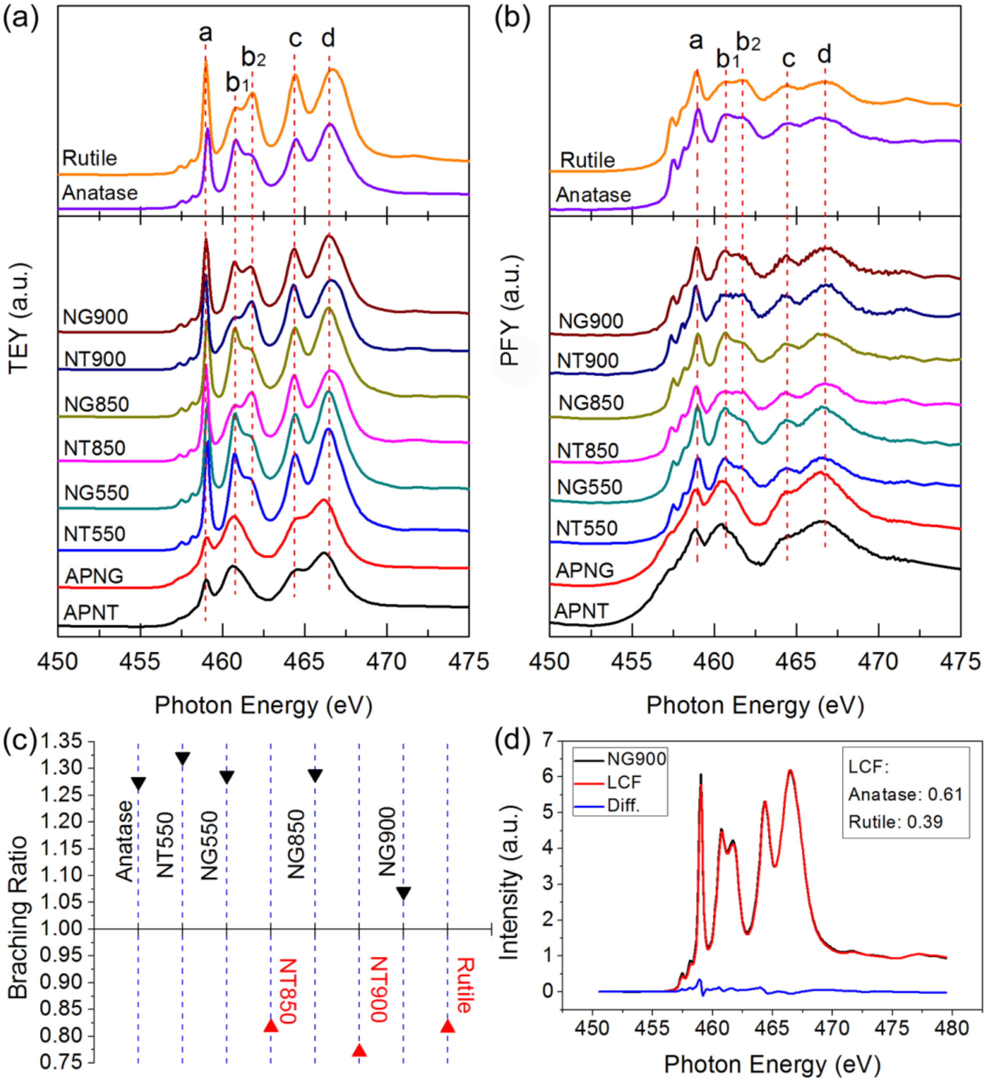

Figure 3-3 Ti $L_{3,2}$-edge XANES of hierarchical TiO_2 nanostructures in comparison with commercial anatase and rutile powder recorded in TEY (a) and PFY (b). (c) The intensity ratio of peak b_1 over b_2 as shown in (a). (d) A linear combination fitting (LCF) at the Ti $L_{3,2}$-edge of NG900, the difference curve between the Ti $L_{3,2}$-edge of NG900 and LCF curve is also included.

Compared to standard anatase and rutile structures, both APNT and APNG show a generally broad Ti $L_{3,2}$-edge XANES and the non-splitting of peak b_1, indicating the amorphous structure of the as-anodized TiO_2 nanostructure [41,42]. After annealing at 550 ℃, 850 ℃ and 900 ℃, all structures become crystalline and the intensity ratio of peak b_1 compared to b_2 is well displayed in **Figure 3-3c**. As discussed above, sample with I_{b1}/I_{b2} value higher than 1 is anatase-dominant, otherwise it is rutile-dominant. Thus both NT550 and NG550 exhibit the anatase-dominant structure. However, striking and intriguing difference in phase transformation between the bottom NT layer and the top NG layer can be observed with a high temperature annealing at 850 ℃: whereas NT850 is further crystallized to a thermal-stable rutile phase, NG850 still exhibits the anatase-dominant structure with a I_{b1}/I_{b2} value comparative to standard anatase, suggesting its mostly crystalline anatase structure. It is interesting to note that the I_{b1}/I_{b2} value of NG finally decreases sharply at 900 ℃ but it is still greater than 1, indicating its multiphase nature. A linear combination fitting process at the Ti $L_{3,2}$-edge was conducted to NG900 using the standard Ti $L_{3,2}$-edge XANES of anatase and rutile (**Figure 3-3d**), which shows that the structure of NG900 is composed of 61 % anatase and 39 % rutile − a stable high temperature anatase phase prepared by electrochemical anodization is born!

Phase transformation investigations in the bulk region of NT and NG layer, are monitored by PFY XANES measurement at the Ti $L_{3,2}$-edge (**Figure 3-3b**). Note that the probing depths of TEY and PFY mode are order of magnitude different: TEY mode collects the ejected photoelectrons, Auger electrons and other secondary electrons from sample surface with a general electron escape depth around several nanometers (universal curve), thus TEY can be detected by monitoring the sample neutralization current (to ground); PFY mode, on the other hand, usually can probe much deeper due to the comparatively larger attenuation length of the fluorescent X-rays although PFY often suffers from self-absorption especially in the soft X-ray region when the specimens are optically thick. As shown in **Figure 3-1**, the attenuation length above the Ti L-edge is ~100 nm. Similar PFY XANES compared with corresponding TEY XANES, as shown in **Figure 3-3b**, indicates both the surface and bulk have the same structure although the general PFY spectra are broadened due to the self-absorption [41], suggesting phase transformation is not only on the surface but also in the bulk, and incurs at the NT and NG layer independently.

Further evidence is provided by the characterization at the O K-edge. As shown in **Figure 3-4**, the two dominant pre-edge peaks A_1 and A_2 are attributed to electronic transitions from O 1*s* to O 2*p* states covalently hybridized with Ti 3*d*-t_{2g} and Ti 3*d*-e_g states, respectively [41,42]. The broad character of A_1 and A_2 is observed for APNT and APNG, indicating their amorphous structure which is supported by the absence of feature C because its presence usually is an indicator of the long range order [42]. Several different features between anatase and rutile can be found at the O K-edge XANES: compared to anatase, the additional peak B_2 shows up in rutile phase and the energy locations of both peaks B_1 and C shift to the high energy region as indicated by black and red arrows, respectively. Thus NT550, NG550 and NG850 clearly show the anatase-dominant structure whereas NT850 and NT900 display the rutile-dominant structure, and the presence of shoulder feature B_2 together with a general anatase XANES profile

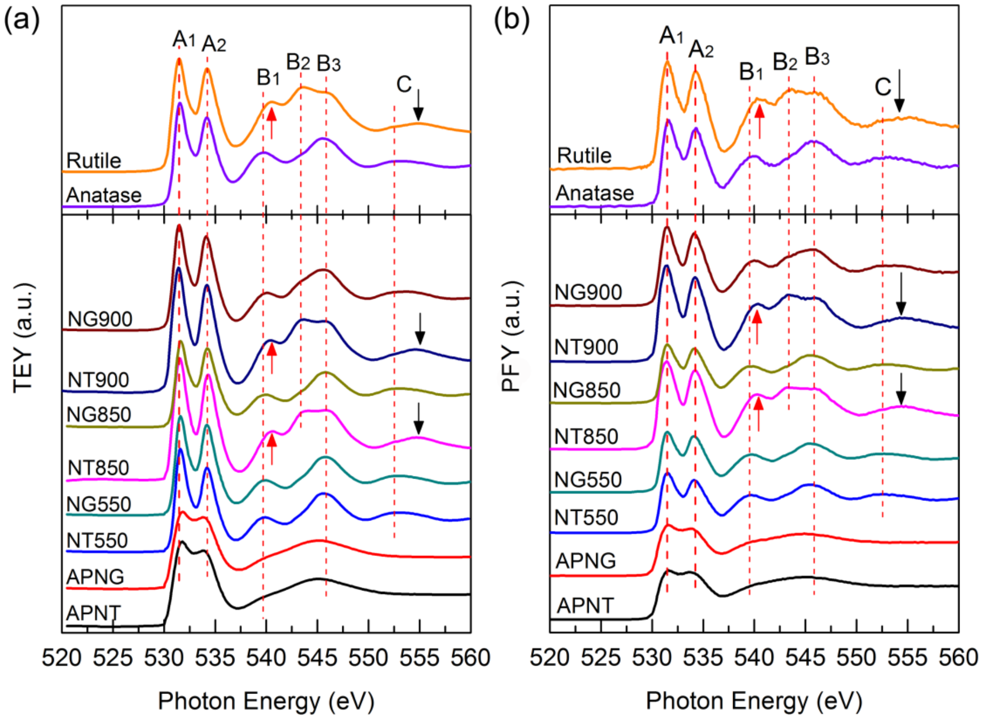

Figure 3-4 O K-edge XANES of TiO_2 hierarchical nanostructure in comparison with commercial anatase and rutile powder standards recorded in TEY (a) and PFY (b).

illustrates the multiphase nature of NG900 with major anatase component. Similar results from TEY and PFY XANES at the O K-edge of NT and NG layer also indicate the same local environment of O ligands both on the surface and in the bulk. Note that the O K-edge PFY and TEY XANES are nearly identical as compared to the different PFY and TEY XANES patterns at the Ti $L_{3,2}$-edge, because the O Kα X-ray has higher energy hence larger escape depth than those of Ti Lα X-rays, suggesting the negligible thickness effect at the O K-edge. Therefore, results from both TEY and PFY XANES at the O K-edge are in good accordance with analysis at the Ti $L_{3,2}$-edge as addressed above.

Therefore, it is certain from the above analysis that in this type of hierarchical TiO_2 nanostructure, the phase transformation process at the NT and NG layer is different, *i.e.*, that the phase transformation is morphology-dependent. It is apparent that the NG layer is much more anatase stable than the NT layer.

The mechanism of ART of TiO_2 has been studied [23,46,47], and it is well documented that the thermal stability of anatase can be improved by downsizing TiO_2 nanostructures to nanoscale. However, previous size dependence study of anatase TiO_2 NPs also indicates that the decrease of the ART temperature correlates with the decrease of particle size [20,22], *i.e.*, that TiO_2 NPs with an ultrafine size have a lower ART temperature than larger NPs. Because smaller NPs with large specific surface area have higher surface energy which will be the driving force for rutile nucleation. Noticeably, Satoh et al. [22] performed the well-designed experiment by first using the atomic-level precise titania to support the above hypothesis. By applying their established model to our system that contains a nanograss layer with anatase stable at 900 ℃, a grain size of ~6 nm is determined; whereas a smaller grain size of ~1.3 nm is calculated for the nanotube layer based on its decreased, anatase-stable temperature at 600 ℃, as stated in a previous report [41]. Nevertheless, SEM results show that the grain size of nanotube layer is comparatively larger than that of nanograss layer with its ultrafine size. This apparent contradictory result, as noted above, is due to the fact that the anodic TiO_2 nanostructure holds the multi-grain nature and the ART involves two competing processes: rutile nucleation and the grain growth of anatase. Although the ART is reported to be instantaneous once the rutile nuclei are present from agglomerated anatase TiO_2 NPs

[20,46], Ding et al. [21] found that anatase TiO_2 NPs with the ultrafine size prepared by sol-gel method can be much more anatase-stable than larger ones.

Consistent with Ding's report, the morphology-dependent ART at the NT and NG layer indicates their different energetics for the phase transformation processes: NT layer can be considered analogous to highly agglomerated TiO_2 NPs in which the presence of the small particles (estimated grain size is ~1.3 nm) as contaminates will initiate the ART and trigger the following phase transformation of larger grains to rutile instantaneously due to their close contact. Results from a previous similar study focusing on TiO_2 NTs show that ordered NTs grown from one-step anodization method tend to be anatase-unstable and transform to rutile and become rutile dominant with a post-annealing temperature at 500 ℃ and 600 ℃, respectively [41]. NTs with a better alignment prepared with a multi-step anodization process also will transform to rutile with a mild annealing temperature at 650 ℃ [48]. On the other hand, NG layer can be treated as well-separated TiO_2 NPs with ultrafine size due to their loose contact resulting from unzipping of top NT layer. Upon high temperature annealing (e.g., 850 ℃), the high surface energy of NG arising from its high surface to volume ratio will be the thermodynamic driven force for the grain growth of anatase instead of ART although a slight amount of rutile nuclei might form. The larger grains grown should transform to rutile very slow due to the size dependence [21,22], which is why the NG900 still has the major anatase component after a grain growth process in NG850. Furthermore, because the rutile nucleation starts from certain sites at the interface of anatase NPs and the passivation of those sites can essentially retard the formation of rutile nuclei and ART [20]. Thus, in our case, these rutile nucleation sites seem to be effectively passivated along with the NG morphology formation due to the comparatively loose contact of unzipped NTs (*i.e.*, NG) than the intact NTs, which is consistent with the SEM results. Therefore, this specific NG morphology with ultrafine size can effectively retard the ART to achieve certain types of nano-heterostructure with the much more anatase-stable property on the top layer.

3.3.2 STXM Analysis of Highly Ordered TiO_2 Nanotube

To further look into the ART behavior of the NT itself, we have synthesized highly ordered TiO_2 NT specimen. The top, side and bottom SEM views of as-grown NTs

(AGNT) and NTs annealed at 750 ℃ (NT750) are shown in **Figure 3-5a ~ 5c** and **Figure 3-5d ~ 5f**, respectively. Apparently, AGNT shows a homogeneous porous structure on the top (inner tube diameter is ~80 nm; tube wall thickness is ~30 nm) and ordered NTs underneath together with closed-end caps at the bottom. After annealing, NT750 suffers from sintering effect and exhibits the shrinkage of entire NT structure. Although it maintains the nanotubular architecture, the top surface of NT750 becomes more coarsened with rich cracks growing along the NT wall, and more interestingly, the

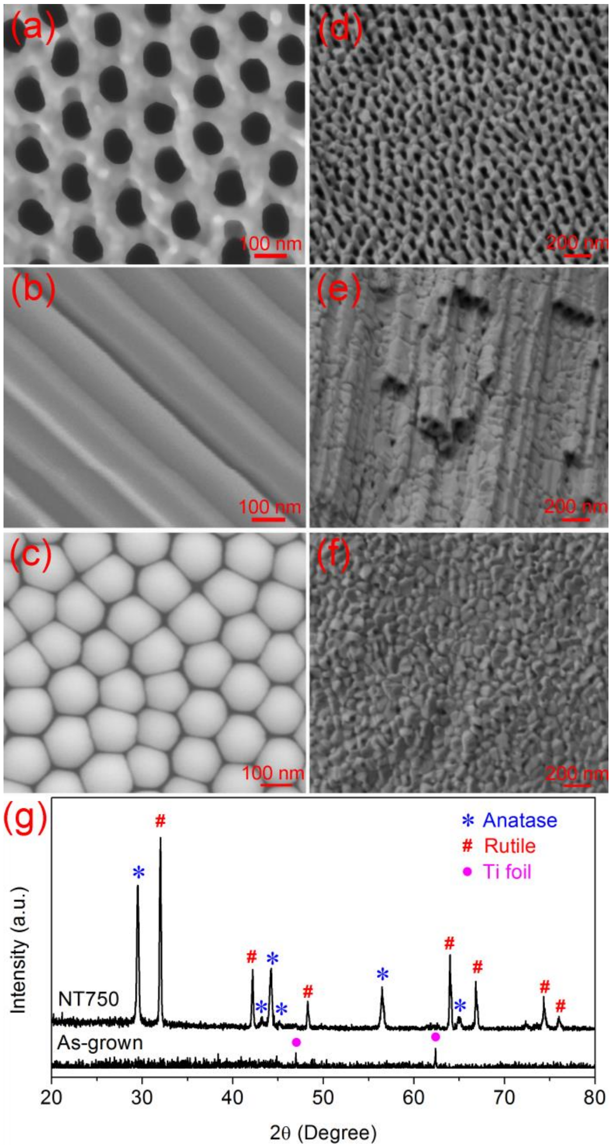

Figure 3-5 SEM (top, side and bottom) views of as-grown NTs (a~c) and NT750 (d~f) together with their XRD patterns (g).

bottom caps completely collapsed and transformed to nanoparticles (NPs) with a size of ~50 nm. X-ray diffraction (XRD) analysis in **Figure 3-5g** shows that AGNT is amorphous, in agreement with previous results [4,49], whereas NT750 presents an anatase-rutile mixed phase with its dominant rutile character.

STXM with its high spatial resolution has been employed to disclose the spatial locations of these co-existing anatase and rutile components in NT750. **Figure 3-6a** shows the SEM view at the cross section of a NT750 lamella prepared by FIB milling and further thinning (**see 3.2.2**). Note that the top region of the NT750 is facing up and covered by a layer of deposited platinum (darker band at the top) for the FIB performance. Clearly, the cross section view of NT750 depicts its two-layered structure with a layer of homogeneous NTs (with a length of ~3 μm) stacked upon a dense structure. In addition, the thickness of the lamella is controlled to be thinner than 100 nm, which is smaller than the attenuation length of X-rays (**see 3.2.3**) with photon energies at the Ti $L_{3,2}$-edge and O K-edge (**Figure 3-1**). Hence, thickness effect on the XANES is negligible [35]. At first, STXM scans across the Ti $L_{3,2}$-edge and O K-edge have been taken separately at the same region of interest (ROI) as indicated with a green rectangle in **Figure 3-6a**. By performing the chemical imaging using the Ti $L_{3,2}$-edge and O K-edge XANES spectra of anatase and rutile standards as references (**see 3.2.3**), the chemical maps of the selected ROI at the Ti $L_{3,2}$-edge and O K-edge are shown in **Figure 3-6b** and **6c**, respectively. Two maps manifest the persistent results, which evidently demonstrate that the pure anatase phase structure (red) resides at the top nanotubular region, whereas the bottom dense layer contains pure rutile structure (green). Notably, a slim yellow band due to color mixing locates between those two layers, indicating the possible anatase-rutile mixed phase at this interface region. To corroborate the speculation, the Ti $L_{3,2}$-edge (**Figure 3-6d**) and O K-edge (**Figure 3-6e**) XANES spectra of those three regions (color-coded with the STXM maps) are extracted directly from their respective STXM optical density image stack (**see 3.2.3**). It is clear to see that clean anatase and rutile XANES profiles at both edges are attained from the homologous red and green ROIs (**Figure 3-6b** and **3-6c**). Interestingly, the yellowish spectra at both edges extracted from the interface region deliver the XANES patterns resembling to both anatase and rutile. Particularly, the intensity ratio value of peak A over B in **Figure 3-6d** sets between that of anatase (red) and rutile (green), which unambiguously illustrates the anatase-rutile mixed nature of this interface layer (**Figure 3-3d**) [4].

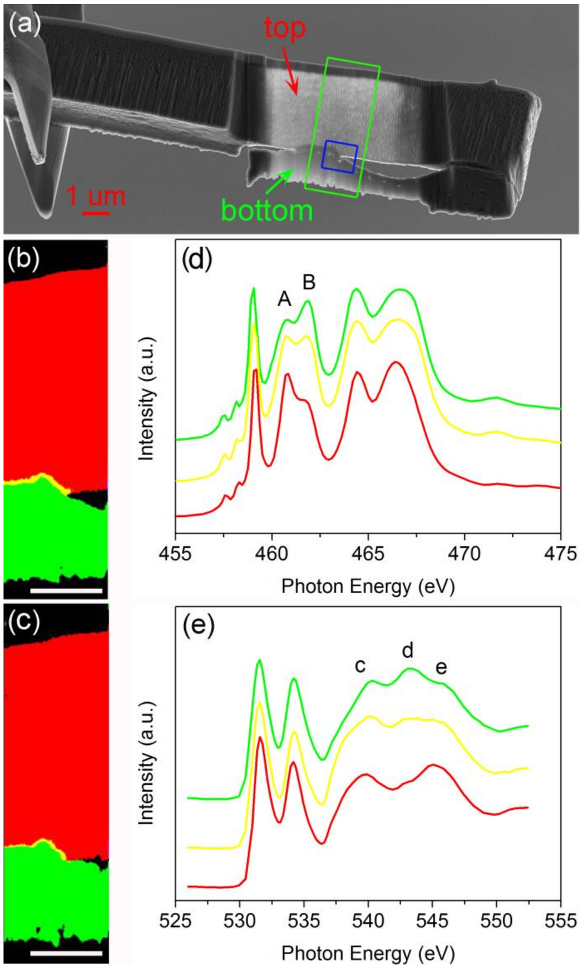

Figure 3-6 (a) SEM views of the as-made NT750 lamella. STXM chemical map at the (b) Ti $L_{3,2}$-edge and (c) O K-edge. (d) Ti $L_{3,2}$-edge XANES extracted from color-coded ROIs in (b). (e) O K-edge XANES extracted from color-coded ROIs in (c). The selected ROI for STXM analysis in (b) and (c) is indicated by a green rectangle in (a). The scale (white) bars in (b) and (c) are 1 µm.

To further reveal the structure of the interface region, a finer STXM scan with high spatial resolution on a narrower ROI marked by a blue rectangle (**Figure 3-6a**) is performed at the Ti $L_{3,2}$-edge. **Figure 3-7a** shows the corresponding optical density (**see 3.2.3**) image.

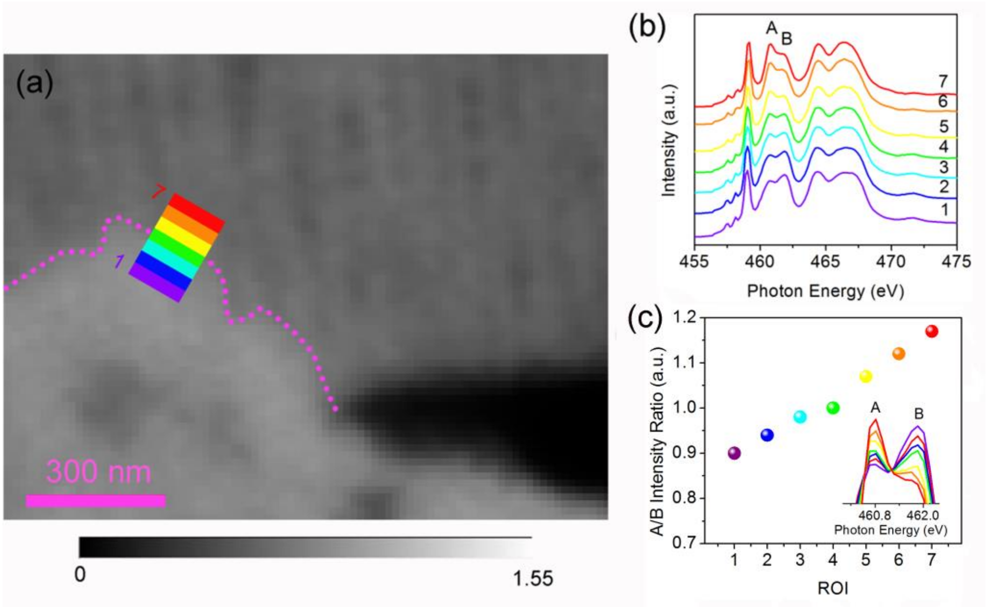

Figure 3-7 (a) A STXM optical density image at 462 eV of ROI marked by the blue rectangle in Figure 3-6a, the optical density bar is included underneath. The scale bar is 300 nm. (b) Ti $L_{3,2}$-edge XANES extracted from color-coded ROIs indicated by mini slabs in (a) with a size of ~ 30 nm × 130 nm. (c) peak intensity ratio of A over B from ROI-1 to ROI-7 shown in (b).

To pinpoint the variation across the interface layer, we selected seven ROIs stacking as mini slabs from the dense (ROI-1) to the tubular (ROI-7) area. The corresponding XANES (color-coded) extracted from the respective ROI are displayed in **Figure 3-7b**. **Figure 3-7c** depicts the relevant A/B intensity ratio across the interface region. Clearly, the XANES evolve from plain rutile (ROI-1) to anatase-rutile mixtures with different ratio (ROI-2 to ROI-6), and eventually to plain anatase (ROI-7) together with the linear trend of peak A/B intensity ratio, suggesting that the interface region involves a gradual phase transition from bottom rutile to top anatase. This finding holds the greatest significance. It reveals that the ART in ordered NTs is triggered at the bottom layer, followed by rutile nucleation upward and continuing rutile growth by making contact with the upper NT layer, resulting in the breakdown of NTs and transformation from nanotubular anatase (~3.8 g cm^{-3}) to a dense rutile (~4.2 g cm^{-3}) layer at the bottom via structure reconstruction. The pure anatase phase on the top NT layer is further confirmed here from two perspectives. First, examinations on seven parallel ROIs (**Figure 3-8a ~**

8c) show their unmistakable anatase characteristics with the same peak A/B intensity ratio in their Ti $L_{3,2}$-edge XANES. Second, another seven ROIs selected with vertically across the top NT layer (**Figure 3-8d ~ 8f**) also exhibit the homogeneous anatase phase for the whole nanotubular region.

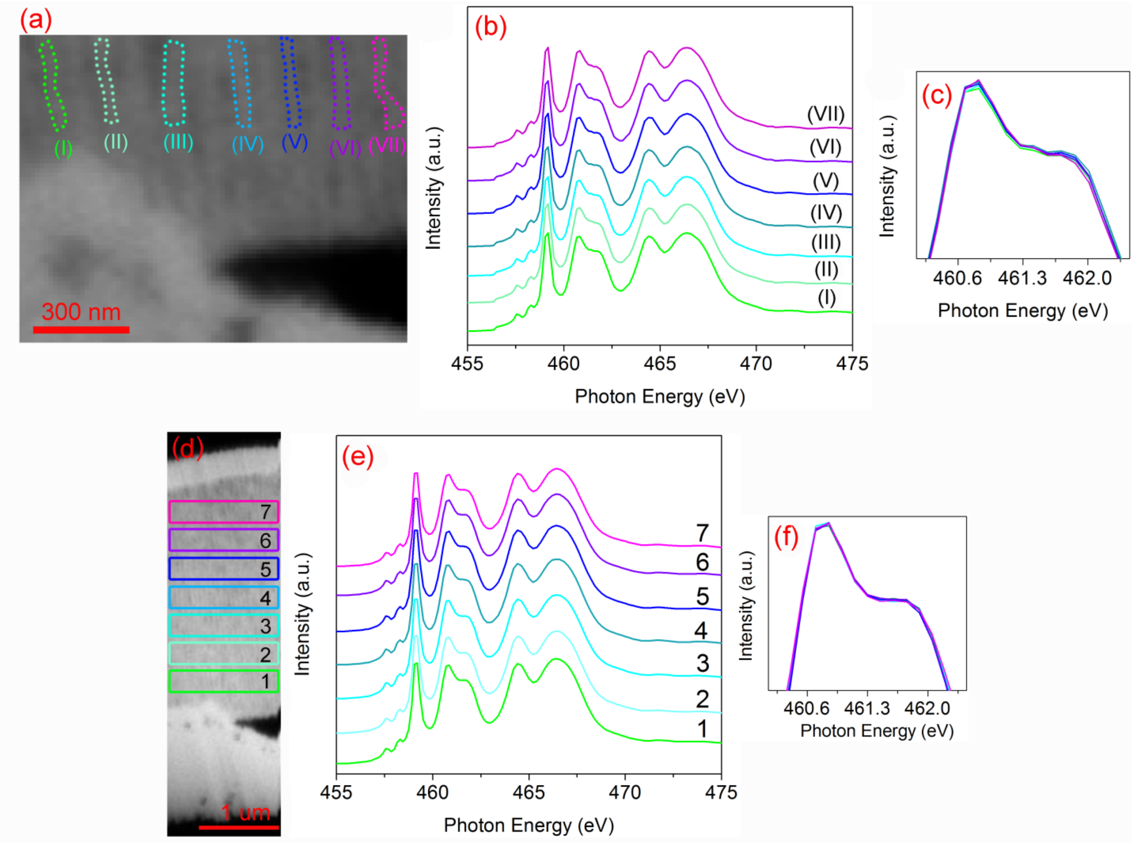

Figure 3-8 (a) A STXM optical density image at 462 eV of ROI indicated by the blue rectangle in Figure 3-6a. (b) Ti $L_{3,2}$-edge XANES extracted from color-coded ROIs indicated by circled dotted lines in (a). (c) A close observation at the Ti L_3-e_g XANES region with the overlay of seven ROIs in (b). (d) A STXM optical density image at 462 eV of ROI indicated by a green rectangle in Figure 3-6a. (e) Ti $L_{3,2}$-edge XANES extracted from seven ROIs indicated by color-coded rectangles in (d), each ROI has a size of ~400 nm × 1.8 μm. (f) A close observation at the Ti L_3-e_g XANES region with the overlay of seven ROIs in (e).

Thereby, we propose a "bottom-up" ART model of anodic TiO_2 NT based on this work. NT specimens, NT500 (as-grown NTs annealed at 500 ℃), NT700, NT800 and NT900, are also prepared and examined to corroborate our model. The associated XRD analysis (**Figure 3-9**) of these four NT speciemens suggests that NT500 holds a pure anatase structure, whereas NT700 and NT800 possess the anatase-dominant and rutile-dominant anatase-rutile mixed structures, respectively, and a pure rutile phase is found in NT900.

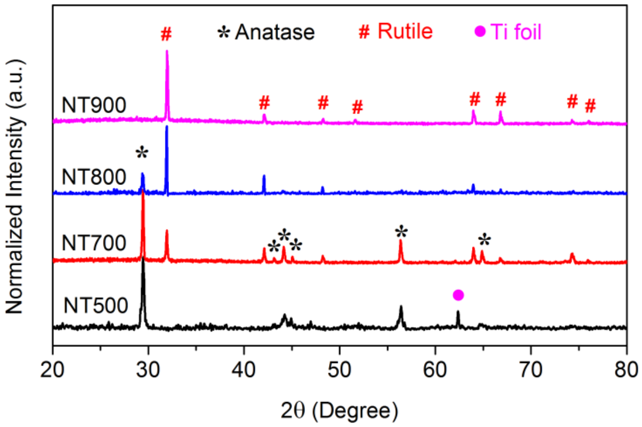

Figure 3-9 XRD of NT500, NT700, NT800 and NT900.

As shown in **Figure 3-10a**, five different stages are used to illustrate how phase transition occurs during thermal annealing at elevated temperatures. From stage 1 to 2, anatase crystallization from as-grown amorphous NTs occurs. Morphologically, **Figure 3-10b** and **10c** show the side and bottom SEM views of anatase NT500. The sintering effect is noticeable, in which NT500 exposes a large amount of cracks along the NT wall compared to the crack-free surface of as-grown NTs (**Figure 3-5b**). The presence of those cracks results from diffusion of bulk defects to the NT surface during structural ordering (i.e., crystallization) and the strain-relief inside the NT structure during annealing. In contrast, the bottom view (**Figure 3-10c**) of NT500, rather than showing cracks, shows the formation of tens of small NPs with the size of ~20 nm on each NT cap. Thus anatase NCs formed in the bottom caps deliver a smaller grain size than that formed in the upper NT walls. This can be attributed to the slightly different chemical nature between the bottom caps and the upper tube walls. Typically, a fluorine rich layer is formed at the bottom of anodic TiO_2 NTs due to the accumulation of F^- ions (from electrolyte) at the metal-oxide ($Ti\text{-}TiO_2$) interface (NT caps) for further NT growth [27,50]. A previous study shows that F^- ions in the as-grown NTs are strongly correlated

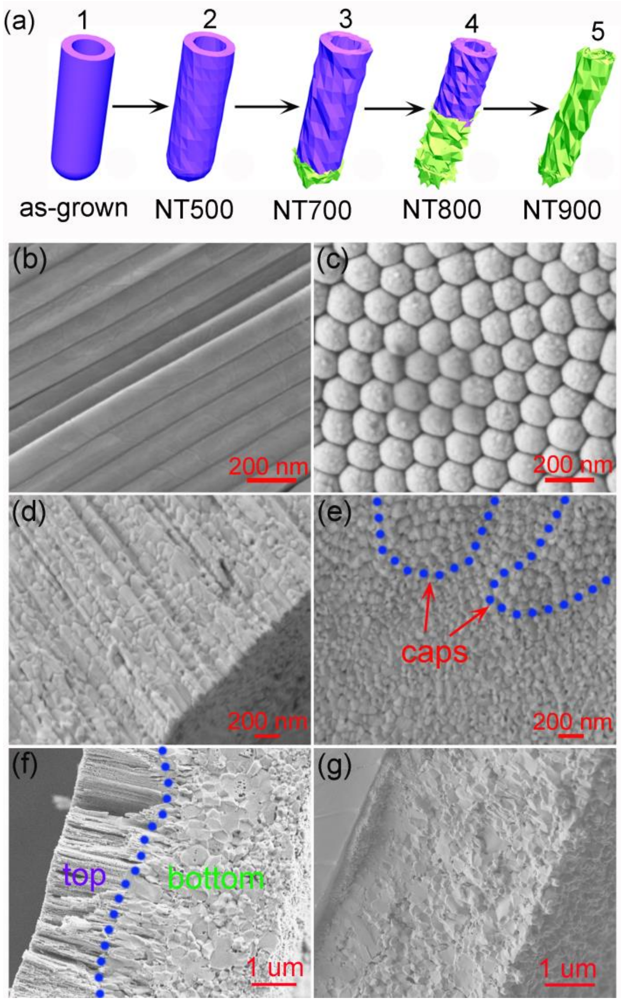

Figure 3-10 (a) Schematic view of the "bottom-up" ART model. (b) Side and (c) bottom SEM views of NT500. (d) Side and (e) bottom SEM views of NT700. (f, g) Side SEM views of NT800 and NT900, respectively.

with the titania lattice and replace some of the oxygen substitutionally to form both surface and bulk Ti-F bonds [51]. In turn, these F impurities can exert a morphology-tailoring effect during anatase crystallization via annealing, which exposes the thermodynamically unstable {001} facet of anatase NC but prevents its stable {101} facet from forming [52,53]. In fact, F-containing reagents have been widely applied to engineer the {001} faceted anatase NCs [54,55]. A high F^- ion concentration usually facilitates the fromation of smaller anatase NC with a high percentage of {001} facets because of the strong interaction of F 2p electron with both Ti 3d and O 2p electrons, resulting in the stabilization of Ti and O atoms on the {001} facet [54,55]. Interestingly, Zhao et al. [24] found that the {001} facet of anatase NC can easily accumulate defects from the bulk via annealing and thus it appears much more defective than the {101} facet, which is due to the high surface energy of {001} facet with its distorted Ti-O-Ti bond angle and a high percentage of 5-coordination Ti [55]. Therefore, anatase NCs in the bottom caps presumably would have a smaller size with a greater percentage of defective {001} facets than NCs in the upper tube walls where the bulk defects diffuse to the tube wall surface as cracks bewteen NCs other than the detention of defects on NC surface. Consistent evidence is provided by Chen et al. [56] who suggested the formation of electronically defective (Ti^{3+} states) anatase phase at the bottom cap layer after anatase crystallization by showing a yellow color, ranther than the natural white color of anatase TiO_2 presented on the top layer. Besides, Yang et al. [31] claimed that the anatase {101} only appears on the tube wall of anodic TiO_2 NTs.

From stage 2 to 3, the rutile nucleation and growth from pure anatase NTs take place from the bottom caps. This can be rationalized in the following. First, the size effect plays an important role. Note that the size-dependency in ART of TiO_2 NPs has been well documented [14,22,46,57], of which the ART temperature is proportional to the size of anatase NPs. Because the smaller size of NP coupled with its accompanying higher surface area and energy not only offers more interfaces for rutile nucleation, but also provides the thermodynamic driving force for ART [4,20]. Consequently, the closely packed small NPs in the bottom caps would trigger the ART. Second, ART in anatase NC exhibits an anisotropic behavior. Zhu et al. [15] recently conducted a comprehensive analysis on the rutile nucleation site of anatase NC at the beginning of ART using the density functional theory (DFT) calculation. They claimed that the exposed {001} facet on anatase NC would significantly reduce the ART energy barrier. Hence, it energetically favors the rutile nucleation. Also, the higher percentage of {001} facet can further lower the ART energy barrier. Zhao et al. [24] echoed that the ART temperature can drop by ~100 ℃ once the {001} facet concentration increases from 32 % to 63 %. By contrast, rutile nucleation on thermodynamically stable {101} facet would be much more difficult. It is caused by the endothermic nature of ART process and a much greater energy barrier for the rutile nucleation from the {101} facet [15]. In our case, as shown in **Figure 3-10d** and **10e**, NT700 with its major anatase and minor rutile phase (**Figure 3-9**) structure exhibits its heavily cracked tube walls as well as the dense nanoparticulate bottom. On one hand, the defective anatase NCs in the bottom caps proposed above with their comparatively higher percentage of {001} facets would trigger the rutile nucleation much easier than anatase NCs in the upper tube walls. Thus the formation of rutile nucleus and further rutile crystal growth proceed favorably at the capped bottom region by aggregation and coalescence (i.e., Ostwald Ripening) [15]. Meantime, the significant local compressive strain induced by structure reconstruction during ART leads to the severely external deformation of the bottom caps and finally results in the total collapse of the cap layer. On the other hand, the {101} anatase in the tube walls are energetically less favorable for rutile nucleation [15,31]. Furthermore, the geometry constraints imposed by the tube wall would impede the ART process [58,59]. Thus the tubular morphology containing the anatase phase would retain at the upper tube wall region although cracks develop into larger ones due to further defect exposure and strain-relief at elevated temperature annealing. In addition, previous studies also show the involvement of Ti substrate in thermal oxidation during annealing, enhancing the rutile nucleation at the NT bottom [29,30,58].

Transformation from stage 3 to 4 depicts further rutile growth from the bottom toward the top at the expense of the tubular anatase structure, where ART in the upper anatase NT layer takes place by making contact at the interface region with the bottom dense rutile crystals. At the interface, further rutile crystal growth occurs by either at the rutile-anatase interface or merging with another rutile crystals [30]. Thus there will not be an abrupt interface. Evidence is provided in **Figure 3-10f** where NT800, together with its rutile-predominant anatase-rutile mixed phase (**Figure 3-9**), manifests a two-layered structure with anatase NT bundles on the top while a dense rutile layer underneath.

Finally, from stages 4 to 5, the full rutile growth prevails at the expense of total annihilation of top nanotubular anatase (**Figure 3-10g**). As a result, NT900 exhibits its pure rutile structure (**Figure 3-9**). It is worth mentioning that, beyond the bottom-up ART model given in **Figure 3-10a**, the rutile nucleation directly in the tube wall between stage 3 and stage 5 is also possible once the energy provided by elevated annealing temperature is high enough. Nevertheless, this possibility is ruled out in this study, because the portion of the as-formed rutile nucleus is too small to be competitive with the bottom-up mechanism.

3.4 Conclusions

Electronic structure associated with phase transformation of hierarchical TiO_2 nanostructure synthesized by an extended electrochemical anodization process and then annealed under elevated temperature, has been thoroughly investigated with the application of XANES analysis at both the top nanograss and bottom nanotube layers. Morphology-dependent phase transformation process has been observed: whereas the bottom NT layer is comparatively anatase-unstable and transforms to compact rutile phase with the total collapse of nanotubular structure at moderate temperature, the top NG layer shows a surprisingly thermal-stable anatase structure due to its ultra-fine grain size resulting from the secondary anodization (unzipping) of the tip NT layer. Based on this finding, several benefits from this hierarchical nanostructure design are noted. First, vast surface area is provided due to the formation of ultra-fine NG layer. Second, anatase-stable nanostructure under high temperature annealing is well achieved compared to TiO_2 nanostructures (mostly TiO_2 NTs) prepared by the similar condition using electrochemical anodization. In particular, hierarchical TiO_2 nanostructure (especially the top NG layer) in this study can retard the ART phase transformation temperature to as high as 850 ℃. Thus potential applications using anatase-stable nanostructures can be developed for high temperature applications. Third, the great potential of this hierarchical TiO_2 nanostructure is that spatially separated top-bottom heterostructures, such as anatase-multiphase, anatase-rutile and multiphase-rutile heterostructures, can be easily fabricated by controlling the thermal-annealing temperature.

Furthermore, a following study regarding the anatase-to-rutile transition (ART) behavior of highly ordered TiO_2 NTs has been carried out using spatially resolved STXM. The as-grown amorphous NTs system annealed at 750 ℃ with its anatase-rutile mixed phase structure is taken as the representative sample of interest for characterizations. STXM examination on the sliced NT750 lamella discloses its double-layered heterostructure. Of which the nanotubular anatase structure resides on the top layer whereas a dense rutile layer forms underneath, and a thin interface layer with a gradual ART is located in-between. Therefore, based on the rationalization of size and the anisotropy dependence of the ART process for TiO_2 NC, a “bottom-up” ART model for the ordered TiO_2 NT is proposed: rutile nucleation initiates from the NT bottom caps and rutile structure growth proceeds further from bottom to the top at the expense of the nanotubular anatase phase via structural reconstruction. In addition, we also want to note that, powerful advanced spectroscopy and microscopy, such as the applications of XANES and STXM in this chapter using synchrotron radiation, are becoming more readily available for the research community and they will be able to play an ever increasing role in tracking fundamental processes in materials research.

3.5 References

[1] X. B. Chen, L. Liu, P. Y. Yu, and S. S. Mao, *Science* **331**, 746 (2011).

[2] L. D. Li, J. Q. Yan, T. Wang, Z. J. Zhao, J. Zhang, J. L. Gong, and N. J. Guan, *Nat. Commun.* **6**, 5881 (2015).

[3] N. Satoh, T. Nakashima, K. Kamikura, and K. Yamamoto, *Nat. Nanotechnol.* **3**, 106 (2008).

[4] J. Li, L. J. Liu, and T. K. Sham, *Chem. Mater.* **27**, 3021 (2015).

[5] M. C. Xu, Y. K. Gao, E. M. Moreno, M. Kunst, M. Muhler, Y. M. Wang, H. Idriss, and C. Woll, *Phys. Rev. Lett.* **106**, 138302 (2011).

[6] H. Tang, K. Prasad, R. Sanjines, P. E. Schmid, and F. Levy, *J. Appl. Phys.* **75**, 2042 (1994).

[7] M. Murdoch, G. I. N. Waterhouse, M. A. Nadeem, J. B. Metson, M. A. Keane, R. F. Howe, J. Llorca, and H. Idriss, *Nat. Chem.* **3**, 489 (2011).

[8] W. Kim, T. Tachikawa, G. H. Moon, T. Majima, and W. Choi, *Angew. Chem., Int. Ed.* **53**, 14036 (2014).

[9] T. Luttrell, S. Halpegamage, J. G. Tao, A. Kramer, E. Sutter, and M. Batzill, *Sci. Rep.* **4**, 4043 (2014).

[10] L. J. Liu, H. L. Zhao, J. M. Andino, and Y. Li, *ACS Catal.* **2**, 1817 (2012).

[11] J. Ryu and W. Choi, *Environ. Sci. Technol.* **42**, 294 (2008).

[12] Z. Luo, A. S. Poyraz, C. H. Kuo, R. Miao, Y. T. Meng, S. Y. Chen, T. Jiang, C. Wenos, and S. L. Suib, *Chem. Mater.* **27**, 6 (2015).

[13] D. Tsukamoto, Y. Shiraishi, Y. Sugano, S. Ichikawa, S. Tanaka, and T. Hirai, *J. Am. Chem. Soc.* **134**, 6309 (2012).

[14] V. N. Koparde and P. T. Cummings, *ACS Nano* **2**, 1620 (2008).

[15] S. C. Zhu, S. H. Xie, and Z. P. Liu, *J. Am. Chem. Soc.* **137**, 11532 (2015).

[16] D. A. H. Hanaor and C. C. Sorrell, *J. Mater. Sci.* **46**, 855 (2011).

[17] K. Dick, T. Dhanasekaran, Z. Y. Zhang, and D. Meisel, *J. Am. Chem. Soc.* **124**, 2312 (2002).

[18] C. L. Cleveland, W. D. Luedtke, and U. Landman, *Phys. Rev. Lett.* **81**, 2036 (1998).

[19] A. N. Goldstein, C. M. Echer, and A. P. Alivisatos, *Science* **256**, 1425 (1992).

[20] J. Zhang, Q. Xu, M. J. Li, Z. C. Feng, and C. Li, *J. Phys. Chem. C* **113**, 1698 (2009).

[21] X. Z. Ding and X. H. Liu, *J. Mater. Res.* **13**, 2556 (1998).

[22] N. Satoh, T. Nakashima, and K. Yamamoto, *Sci. Rep.* **3**, 1959 (2013).

[23] J. Zhang, M. J. Li, Z. C. Feng, J. Chen, and C. Li, *J. Phy. Chem. B* **110**, 927 (2006).

[24] Y. B. Zhao, Y. F. Zhang, H. W. Liu, H. W. Ji, W. H. Ma, C. C. Chen, H. Y. Zhu, and J. C. Zhao, *Chem. Mater.* **26**, 1014 (2014).

[25] K. Shin, S. Il Seok, S. H. Im, and J. H. Park, *Chem. Commun.* **46**, 2385 (2010).

[26] J. Hensel, G. M. Wang, Y. Li, and J. Z. Zhang, *Nano Lett.* **10**, 478 (2010).

[27] A. Ghicov and P. Schmuki, *Chem. Commun.* 2791 (2009).

[28] D. Regonini, C. R. Bowen, A. Jaroenworaluck, and R. Stevens, *Mater. Sci. Eng. R-Rep.* **74**, 377 (2013).

[29] M. Jarosz, K. Syrek, J. Kapusta-Kolodziej, J. Mech, K. Malek, K. Hnida, T. Lojewski, M. Jaskula, and G. D. Sulka, *J. Phys. Chem. C* **119**, 24182 (2015).

[30] O. K. Varghese, D. W. Gong, M. Paulose, C. A. Grimes, and E. C. Dickey, *J. Mater. Res.* **18**, 156 (2003).

[31] B. Yang, C. K. Ng, M. K. Fung, C. C. Ling, A. B. Djurisic, and S. Fung, *Mater. Chem. Phys.* **130**, 1227 (2011).

[32] T. Regier, J. Paulsen, G. Wright, I. Coulthard, K. Tan, T. K. Sham, and R. I. R. Blyth, *AIP Conf. Proc.* **879**, 473 (2006).

[33] A. L. D. Kilcoyne *et al.*, *J. Synchrotron Radiat.* **10**, 125 (2003).

[34] J. G. Zhou, J. Wang, H. T. Fang, C. X. Wu, J. N. Cutler, and T. K. Sham, *Chem. Commun.* **46**, 2778 (2010).

[35] J. Li, Z. Q. Wang, A. K. Zhao, J. Wang, Y. Song, and T. K. Sham, *J. Phys. Chem. C* **119**, 17848 (2015).

[36] http://unicorn.mcmaster.ca/aXis2000.html.

[37] J. G. Zhou, J. Wang, C. L. Sun, J. M. Maley, R. Sammynaiken, T. K. Sham, and W. F. Pong, *J. Mater. Chem.* **21**, 14622 (2011).

[38] Z. Q. Wang, W. Wang, T. K. Sham, and S. G. Yang, *Nanoscale* **6**, 9783 (2014).

[39] http://henke.lbl.gov/optical_constants/atten2.html.

[40] P. I. Gouma and M. J. Mills, *J. Am. Ceram. Soc.* **84**, 619 (2001).

[41] L. J. Liu, J. Chan, and T. K. Sham, *J. Phys. Chem. C* **114**, 21353 (2010).

[42] J. G. Zhou *et al.*, *J. Mater. Chem.* **19**, 6804 (2009).

[43] F. M. F. Degroot, M. O. Figueiredo, M. J. Basto, M. Abbate, H. Petersen, and J. C. Fuggle, *Phys. Chem. Miner.* **19**, 140 (1992).

[44] P. Kruger, *Phys. Rev. B* **81**, 125121 (2010).

[45] P. Guttmann, C. Bittencourt, S. Rehbein, P. Umek, X. X. Ke, G. Van Tendeloo, C. P. Ewels, and G. Schneider, *Nat. Photon.* **6**, 25 (2012).

[46] K. Sabyrov, N. D. Burrows, and R. L. Penn, *Chem. Mater.* **25**, 1408 (2013).

[47] G. H. Lee and J. M. Zuo, *J. Mater. Sci.* **46**, 1780 (2011).

[48] J. J. Gong, Y. K. Lai, and C. J. Lin, *Electrochim. Acta* **55**, 4776 (2010).

[49] J. Li, T. K. Sham, Y. Ye, J. Zhu, and J. Guo, *J. Phys. Chem. C* **119**, 2222 (2015).

[50] S. P. Albu, A. Ghicov, S. Aldabergenova, P. Drechsel, D. LeClere, G. E. Thompson, J. M. Macak, and P. Schmuki, *Adv. Mater.* **20**, 4135 (2008).

[51] J. Li, C. H. Liu, Y. F. Ye, J. F. Zhu, S. D. Wang, J. H. Guo, and T. K. Sham, *J. Phys. Chem. C* **120**, 4623 (2016).

[52] Y. Alivov and Z. Y. Fan, *Nanotechnology* **20**, 405610 (2009).

[53] J. Naduvath, P. Bhargava, and S. Mallick, *J. Phys. Chem. C* **119**, 9574 (2015).

[54] T. R. Gordon, M. Cargnello, T. Paik, F. Mangolini, R. T. Weber, P. Fornasiero, and C. B. Murray, *J. Am. Chem. Soc.* **134**, 6751 (2012).

[55] H. G. Yang, C. H. Sun, S. Z. Qiao, J. Zou, G. Liu, S. C. Smith, H. M. Cheng, and G. Q. Lu, *Nature* **453**, 638 (2008).

[56] C. L. Chen *et al.*, *Phys. Chem. Chem. Phys.* **17**, 22064 (2015).

[57] A. S. Barnard and H. F. Xu, *ACS Nano* **2**, 2237 (2008).

[58] O. K. Varghese, M. Paulose, K. Shankar, G. K. Mor, and C. A. Grimes, *J. Nanosci. Nanotechnol.* **5**, 1158 (2005).

[59] K. P. Kumar, K. Keizer, A. J. Burggraaf, T. Okubo, and H. Nagamoto, *J. Mater. Chem.* **3**, 1151 (1993).

Chapter 4

4 Unraveling the Origin of Visible Light Capture by Core–Shell Titania Nanotubes

4.1 Introduction

As one of the most promising photocatalysts, TiO_2 recently has been treated as one of the foremost significant materials in the environmental and energy realm [1-4]. However, the large band gap of TiO_2 (~3 eV) only allows absorption in the ultraviolet (UV) and thus constitutes severe limitation for its applications in photocatalysis, as UV just holds a small fraction (~5%) of solar energy compared to visible (~43%) and near-infrared (~52%) [2,5]. In developing novel TiO_2 nanostructures to extend their photoabsorption to the visible and near-infrared regions, narrowing the band gap of TiO_2 by properly altering the band energy will establish a benchmark for engineering sunlight-driven functional materials.

Generally, chemical doping by appropriate introduction of metal and nonmetal impurities is the popular way for tailoring the TiO_2 band gap [1,3,6,7]. Among them, N doping is a typical example and N-doped TiO_2 indeed has shown some success in extending its optical response to the visible region [3,8]. The involvement of substitutional N doping is considered to be indispensable for TiO_2 band gap narrowing by upshifting the valence band maximum as a result of the mixing between N 2p and O 2p states [3]. Besides, synergistic interaction between N dopant and the concomitant Ti^{3+} is also believed as the key for the improved photoabsorption and associated photoactivity of N-doped TiO_2 [3,8,9]. Nevertheless, the insufficient visible and near infrared absorption of N-doped TiO_2 reported so far makes it less than satisfactory for solar energy utilization [1].

*A version of this chapter has been published in *Chem. Mater.* **28**, 4467 (2016) and *J Phys. Chem. C* **120**, 4623 (2016).

Recently, Chen *et al.* [1] applied high pressure hydrogen treatment to obtain the core–shell black TiO_2, of which the introduction of disorder on the surface shows its decisive role in reducing the TiO_2 band gap, resulting in considerable improvement in visible and infrared absorption of black TiO_2. Since then, vast efforts have been made to investigate this type of disordered TiO_2 nanostructures and to reveal the origin of visible light absorption [1,10-14]. The creation of two band tail states by surface disorder associated with their merging with the valence band maximum and conduction band minimum of TiO_2, has long been believed to be responsible for the band gap narrowing of highly reduced black TiO_2 [1,14]. Yet, this nonspecific ascription does not pinpoint the chemical nature of the outermost amorphous layer, and the mechanism for the optical absorption remains inconclusive. Alternatively, a very recent report by Tian *et al.*[12] provides the evidence of Ti_2O_3 formation in the surface layer *via* interstitial diffusion of Ti ions from the bulk rutile TiO_2. The distinct points are the narrow band gap of Ti_2O_3 and its robust structure for preserving the surface Ti^{3+} [8,10,12]. However, two issues still need to be addressed. First, the amorphous layer grown on top of the anatase TiO_2 is the one which exhibits superior photoactivity, and the surface amorphization behavior between anatase and rutile is certainly different [1,13]. Therefore, it is crucial to understand the chemical nature of the surface disordered layer above the anatase TiO_2. Second and more importantly, the amorphous shell with a single phase on its own could not achieve the broad light absorption at both the visible and the near-infrared regions [1], so the synergistic interaction between the amorphous shell and anatase core corresponding to the enhanced photoabsorption of black TiO_2 needs to be clarified.

In this chapter, we show that NH_3 annealing of vertically aligned TiO_2 nanotubes (NTs) in the amorphous phase can create such a disordered shell on the crystalline anatase core. Oriented TiO_2 NTs are chosen due to their high aspect ratio and unidirectional alignment, making them the ideal structure for diverse applications [2,15,16]. A distinct advantage of this method to fabricate ordered black TiO_2 NTs over others such as high-pressured hydrogenation [1], pulsed laser vaporization [12] and electrochemical reduction [17], is its simplicity and excellent control of crystallinity without breaking the nanoarrays. The black TiO_2 NTs thus obtained significantly enhance the optical response with a continuous spectrum of photoabsorption from UV to near-infrared. To fully understand the origin of this outstanding photo-response, we have conducted careful surface and bulk characterization of these black TiO_2 NTs. X-ray absorption near-edge structure (XANES) and resonant inelastic scattering (RIXS) in combination with X-ray photoelectron spectroscopy (XPS), are employed to reveal the electronic and structural properties of and the differences between the amorphous shell and the crystalline core of the black TiO_2 NTs. Of which surface-sensitive XANES (using total electron yield) coupled with XPS is used to provide chemical information of the amorphous shell, whereas bulk-sensitive XANES (using X-ray partial fluorescence yield) in combination with RIXS is utilized to elucidate the photoabsorption properties, hence structure and bonding of the anatase core.

4.2 Experimental Section

4.2.1 Sample Preparation

Vertically aligned TiO_2 NTs with preferred geometry and alignment were prepared using a two-step electrochemical anodization process. A custom-made two-electrode cell was constructed using a Ti foil (0.1 mm in thickness, Goodfellow) with a surface area of 1 cm × 2 cm as the anode while a Pt wire as the cathode. The Ti foil was first rinsed by deionized water followed by absolute ethanol, then Ti anodization was conducted at 50 V (Hewlett-Packard 6209B DC power supply) for 4 h to initiate the first NT layer growth with an electrolyte consisting of 0.3 wt % NH_4F (98 %, Alfa Aesar), 2 vol % H_2O and ethylene glycol. Once finished, the Ti sheet was soaked in 1 M HCl for 5 min to peel off the first NT layer then rinsed with deionized water and absolute ethanol. Subsequently, the refreshed sheet was used for the second Ti anodization at 50 V for 30 min using the same but a fresh batch of the electrolyte as in the first step. Finally, the product NT was rinsed with absolute ethanol several times to remove the excessive electrolyte then dried with N_2 gas. The as-prepared (or as-grown) NT is denoted APNT. Then it was cut into 4 pieces: two were kept as APNT, two were annealed in ambient air under 450 ℃ for 2 h with a ramping rate of 5 ℃/min to induce the crystallization of NTs, which are denoted NT450; after that, the annealing of NT450 (one piece) and APNT (one piece) in NH_3 was carried out simultaneously at 450 ℃ for 2 h to obtain N-doped NT450 and N-doped as-prepared NT, henceforth denoted NNT450 and NNT, respectively. NH_3 annealing was performed using a tube furnace: the tube was first purged with pure Ar with a gas flow of 10 mL/min for 10 min and then the samples (one NT450 and one APNT) were heated under an NH_3 gas flow of 100 mL/min to atmospheric pressure with a ramping rate of 5 ℃/min. Excessive NH_3 gas was bubbled through water.

4.2.2 Characterization

Scanning electron microscopy (SEM) images were recorded using a LEO (Zeiss) 1540 XB SEM. The microscopic NT structure was examined by high-resolution transmission electron microscopy (HRTEM, FEI Quanta FRG 200F) operating at 200 kV. X-ray diffraction (XRD, PANalytical Empyrean) was used to characterize the crystal structures of various NT samples. Room temperature UV-vis absorbance spectroscopy was recorded in the wavelength range of 300-800 nm using a Lambda 750 spectrophotometer (Perking Elmer). X-ray photoemission spectroscopy (XPS, Kratos Axis Ultra DLD, monochromatic Al Kα) was performed in an ultrahigh vacuum to characterize the electronic structures of various samples, the binding energy was calibrated to the C 1s reference peak at 284.5 eV. The resulting XPS data was fitted using software XPS PEAK 4.1.

Synchrotron experiments were performed at both the Canadian Light Source (CLS, Saskatoon, SK, Canada) and the Advanced Light Source (ALS), Lawrence Berkeley National Laboratory (LBNL, Berkeley, CA, US). Ti $L_{3,2}$-edge, F K-edge, O K-edge and N K-edge XANES were measured using the Spherical Grating Monochromator (SGM) beamline at CLS with an energy resolution $E/\Delta E > 5000$ [18]. Total electron yield (TEY) and partial fluorescence yield (PFY, collected from the element-specific fluorescence channel using a SSD detector) were used for data collection. All XANES spectra were normalized to the incident photon flux. Ti 2p RIXS spectra and some of the Ti $L_{3,2}$-edge and O K-edge XANES were collected at beamlines 6.3.2.1 and 8.0.1 of the ALS, where a high resolution grazing-incidence grating spectrometer with a 0.4 eV resolution was used [19].

4.3 Results and Discussion

4.3.1 SEM, TEM and UV-Visible Spectroscopy

The morphologies of NT450, NNT450 and NNT were characterized using SEM. As shown in **Figure 4-1a** ~ **1f**, NTs exhibit the compact porous nanotubular structure with an inner diameter of ~ 60 nm, a tube wall thickness of ~ 30 nm, and a length of ~ 3.2 μm as indicated in the inset of **Figure 4-1b**. Both the top and side SEM views of NTs do not show any observable change among these three specimens. A further analysis of NT morphology and crystal structure is demonstrated by their relevant TEM and high-resolution TEM (HRTEM) images. As illustrated in **Figure 4-1g** ~ **1*l***, all NT specimens show the well-shaped nanotubular morphology with a tube wall thickness of ~30 nm, consistent with their SEM results. By air annealing of the as-prepared NTs (APNT) at 450 ℃, NT450 (**Figure 4-1g** and **1h**) displays the full crystallized NTs. NNT450 (**Figure 4-1i** and **1j**) obtained by a further annealing of NT450 at 450 ℃ in NH_3 maintains its crystallinity compared to NT450. In contrast, NH_3 annealing of the as-grown NTs at 450 ℃ directly without air annealing, NNT, yields an amorphous outer layer with a thickness of ~ 4 nm (on both the inner and outer wall of the tube) encapsulating a crystalline core, as shown in **Figure 4-1k** and **1*l***. The corresponding diffraction patterns of APNT, NT450, NNT450 and NNT are illustrated in **Figure 4-1m**. APNT only shows diffraction peaks from the Ti foil (JCPDS 44-1294), indicating the amorphous nature of these as-grown NTs. Once annealed, NT450, NNT450 and NNT all exhibit the anatase TiO_2 (JCPDS 65-5714) characteristic peaks as well as the strong signal from Ti substrate, no trace of a secondary phase (e.g., titanium oxynitride or titanium nitride) is observed in both NNT450 and NNT. However, the anatase peak intensity in NNT is much weaker than that of NT450 and NNT450, which suggests the decrease of crystallinity due to the surface amorphization of NTs, consistent with the HRTEM result in **Figure 4-1*l***.

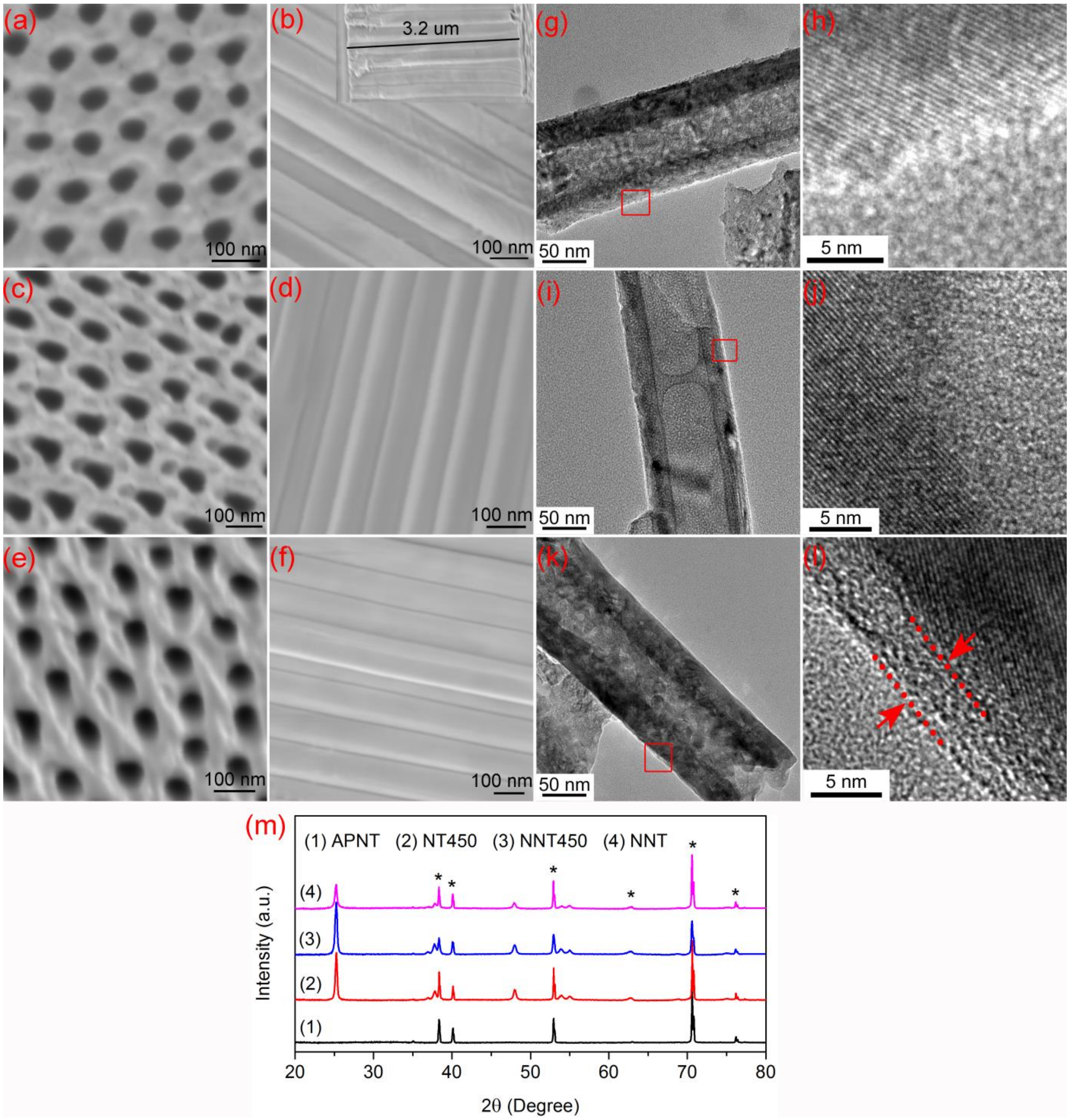

Figure 4-1 Top/side SEM images of (a/ b) NT450, (c/d) NNT450 and (e/f) NNT; the inset of (b) shows the ~3.2 µm thickness of the as-obtained NT film. TEM/HRTEM images of (g/h) NT450, (i/j) NNT450 and (k/*l*) NNT where the location of shown HRTEM images are indicated in their corresonding TEM images with red rectangulars. (m) XRD patterns of (1) APNT, (2) NT450, (3) NNT450 and (4) NNT. Diffraction peaks labelled with star (*) are attributed to Ti substrate (JCPDS 44-1294).

Herein, the first important innovation of this work is the synthesis of anatase-core–amorphous-shell TiO_2 NTs by NH_3 annealing from amorphous phase. **Figure 4-2** illustrates the main steps for the growth of TiO_2 NTs and post-annealing for crystallization. The first step is the growth of vertically aligned amorphous NTs by electrochemical anodization on a refreshed Ti foil. Clearly, after air annealing at 450 ℃ followed by NH_3 annealing at 450 ℃, both NT450 and NNT450 are fully crystallized to the anatase TiO_2 phase. In comparison, NH_3 annealing of amorphous NTs (APNT) at 450 ℃ produces the newly core–shell heterostructure of NNT with an amorphous surface (inner and outer shells) and a crystalline anatase core.

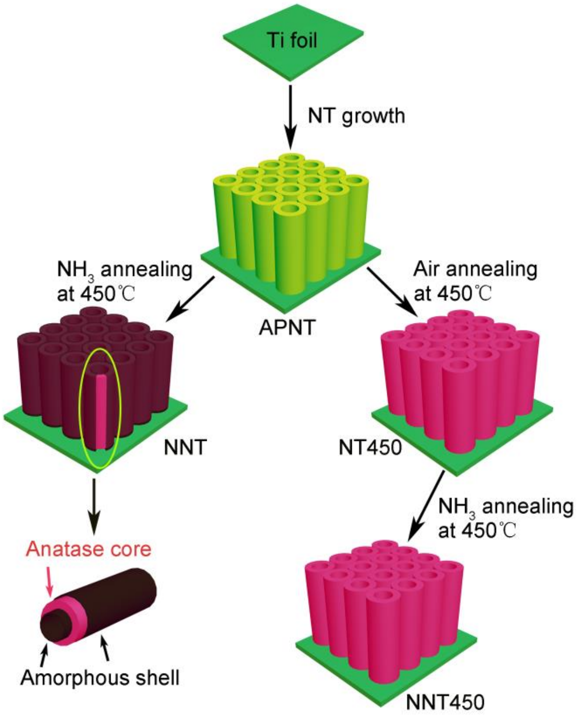

Figure 4-2 Schematic diagram of TiO_2 NTs growth together with subsequent air and NH_3 annealing to fabricate NT450, NNT450 and NNT.

UV-vis absorbance spectroscopy was performed to examine the photoabsorption capability of core–shell NTs. As shown in **Figure 4-3a**, bare anatase TiO_2 NTs (NT450) mainly absorb UV light where the absorption edge is located at ~380 nm associated with the typical band gap of pure anatase TiO_2 (~3.2 eV). After NH_3 annealing of NT450, NNT450 exhibits a slight enhancement of UV absorption and a sharp increase of absorption in the visible region, showing a broad band centered at ~600 nm. By contrast, NNT with a core–shell heterostructure significantly harvests the entire visible wavelength. It starts to absorb continuously from the UV region and extends to the visible then the near-infrared region, suggesting the presence of significant state in the band gap and band gap reduction of NNT compared to NT450 and NNT450 [1,8,14,20]. Such light absorption enhancement is consistent with the dark black color of NNT as shown in the inset of **Figure 4-3a**. In addtion, it is worth noting that the black color of NNT remains unchanged over 10 months after its synthesis, in line with its photoabsorption behavior (**Figure 4-3b**), suggesting the robust air-stability of the as-made black TiO_2 NTs.

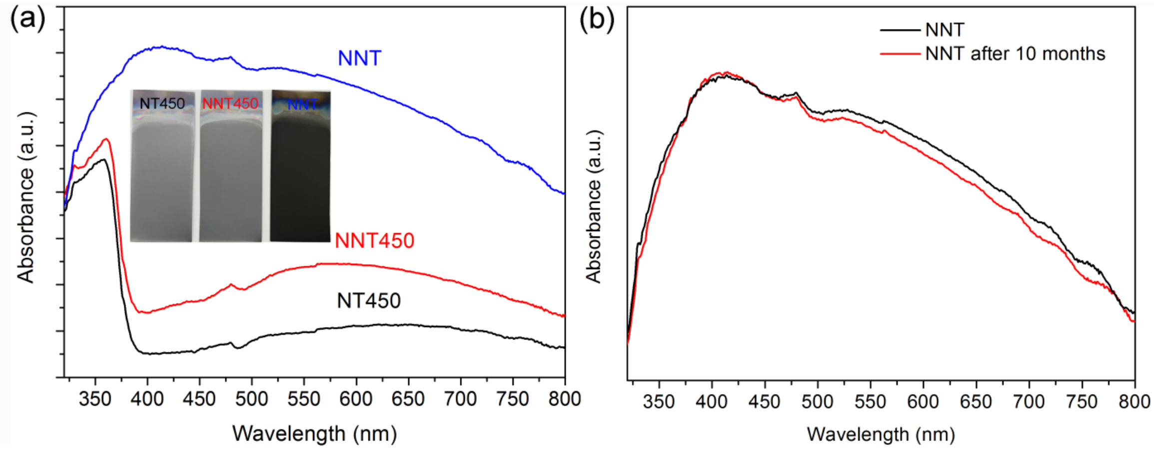

Figure 4-3 (a) UV-vis absorbance spectra of NT450, NNT450 and NNT. The inset shows their different colors. (b) UV-vis absorbance spectra of NNT and the same NNT after air-aging for 10 months.

4.3.2 XANES, XPS and RIXS

The intense light absorption accomplished by NNT evidently suggests the establishment of a synergistic interaction between its amorphous shell and anatase crystalline core. To unravel the origin of its excellent visible light capture, characterizations on the surface and in the bulk should be conducted carefully and preferentially. Here, we utilize X-ray absorption near-edge structure (XANES) with detection modes of total electron yeild (TEY) and partial fluorescence yield (PFY). TEY is surface-sensitive since it collects mainly secondary electrons from the NTs surface with a electron escape depth of ~4 nm (a dimension matches the thickness of the amorphous phase in **Figure 4-1*l***), whereas PFY is bulk-sensitive collecting element-specific fluorescent X-rays with an attenuation length at least two orders of magnitude larger than secondary electrons [21]. Therefore, TEY and PFY XANES in the soft X-ray region as in this case can be applied to comparatively analyze the electronic structure corresponding to the amorphous shell and the anatase core of NNT, respectively.

TEY and PFY XANES spectra of relevant samples at the Ti $L_{3,2}$-edge are shown in **Figure 4-4**, in which samples of Ti_2O_3 ($3d^1$, *Sigma-Aldrich*), anatase and rutile TiO_2 ($3d^0$, *Sigma-Aldrich*) are used as standards for comparison. It should be mentioned that the PFY XANES in **Figure 4-4b** get damped compared to TEY in **Figure 4-4a** due to the self-absorption [21]. Generally, Ti $L_{3,2}$-edge probes electron transitions from Ti 2p core states to unoccupied states of Ti 3d character. It includes the two pre-edge features (peak m and n) where their origin can be assigned to core-hole–d-electron interactions [22,23], and the Ti L_3-edge (peak a, b and c) and L_2-edge (peak d and e) due to electronic transitions from the spin-orbit split Ti $2p_{3/2}$ and $2p_{1/2}$ initial states, respectively, to the Ti 3d final states. Peak splitting into two well-resolved t_{2g} and e_g peaks within both the Ti L_3-edge and L_2-edge results from crystal field splitting. Most importantly, the further splitting of e_g peak (into peak b and c) at the Ti L_3-edge is attributed to the local tetragonal distortion at the Ti site of the TiO_6 octahedron [24] or alternatively the long-range (non-local) distortion of TiO_6 octahedron connectivity [25]. Besides, the extent of the e_g peak splitting is also related to the oxidation state of Ti, *i.e.*, that experimentally, the lesser resolved peaks b and c indicates a lower Ti oxidation which implies the presence of some Ti 3d character [26]. Indeed, **Figure 4-4a** shows that different local distortion of TiO_6 from O_h symmetry yields different Ti L_3-edge e_g peak splitting behavior between anatase (D_{2d}) and rutile (D_{2h}) TiO_2. While the former shows a more intense feature b over c, the latter exhibits a reverse trend. Furthermore, with the decrease of Ti oxidation from TiO_2 ($3d^0$ for both anatase and rutile) to Ti_2O_3 ($3d^1$), the nominal gains of 0 and 1 electron occur, respectively, in the Ti 3d-t_{2g} orbital (or d band). These electron filling processes result in the decrease of Ti 3d-t_{2g} unoccupied states and further reduction in symmetry due to Jahn-Teller distortion, which together with exchange interaction would result in peak width broadening [27]. Concomitantly, the relevant t_{2g}

(peaks a and d) intensity decreases, then the reduction of t_{2g}/e_g intensity ratio as well as the less resolved e_g peak splitting at the Ti L_3-edge of Ti_2O_3 are clearly shown in **Figure 4-4a** [26]. Nevertheless, it is worth mentioning that although the Ti_2O_3 standard in this work is purchased freshly from *Sigma-Aldrich* and used for the first time, it appears to be oxidized on its surface by clearly presenting the distinct TEY XANES (**Figure 4-4a**) with its PFY spectrum (**Figure 4-4b**) from the bulk which shows a more consistent XANES profile with previous studies [12,28], suggesting the severe instability of Ti_2O_3 standard in ambient air.

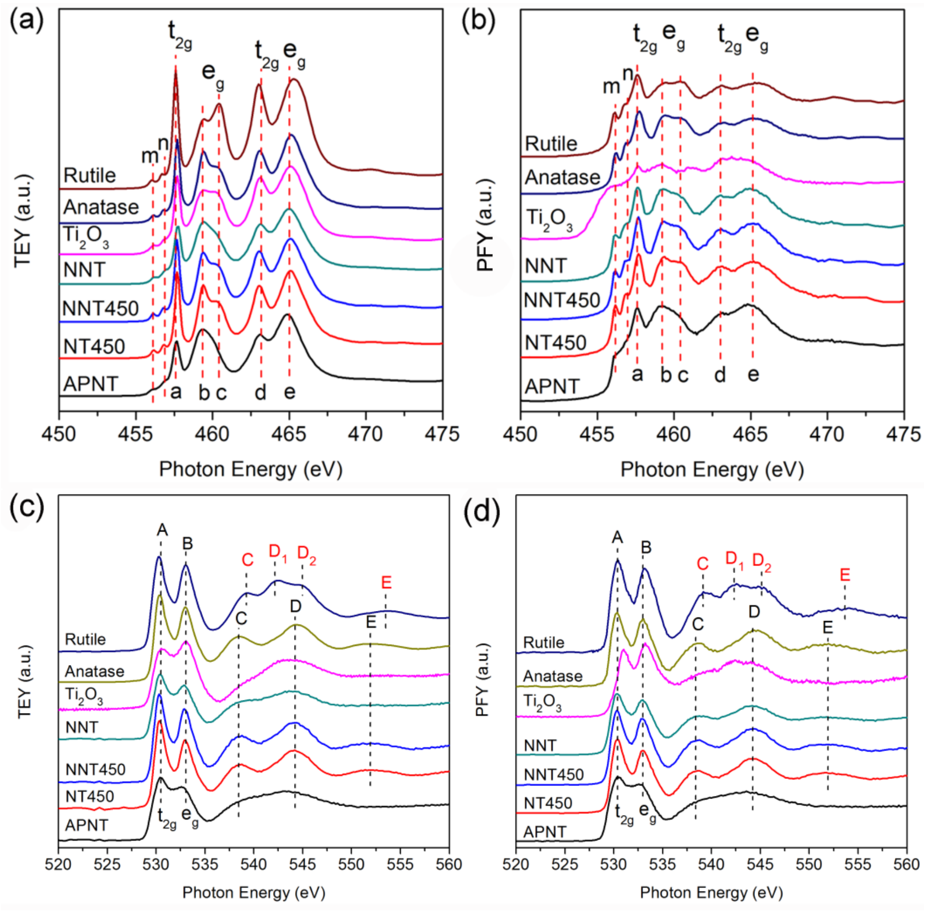

Figure 4-4 Ti $L_{3,2}$-edge XANES spectra of APNT, NT450, NNT450 and NNT in comparison with that of Ti_2O_3, anatase and rutile standards as recorded in TEY (a) and PFY (b) modes. O K-edge XANES spectra of APNT, NT450, NNT450 and NNT in comparison with those of Ti_2O_3, anatase and rutile standards as recorded in TEY (c) and PFY (d).

Comparing to the standards, both NT450 and NNT450 in **Figure 4-4** display the anatase fine structure both on the surface and in the bulk, which, in line with XRD analysis (**Figure 4-1m**), demonstrates their crystalline anatase structure. As for the core–shell NNT, while its core presents an anatase PFY XANES as expected, its amorphous shell, together with APNT, exhibits a TEY XANES pattern which resembles that of oxidized Ti_2O_3 standard, showing the absence of Ti L_3-e_g peak splitting and the decrease of the t_{2g}/e_g intensity ratio. It confirms that the Ti oxidation state on the NNT surface is partially reduced from Ti^{4+}. Also, note that the reduction of Ti^{4+} in APNT is due to the self-doped F^- ions from Ti anodization which we will address later.

Results of TEY and PFY XANES recorded at the O K-edge echo the above analysis at the Ti $L_{3,2}$-edge. As shown in **Figure 4-4c** and **4d**, fine structures at the O K-edge are mainly due to electronic transitions from O 1s to the unoccupied states of O 2p character. Two pre-edge features A and B correspond to transitions from O 1s to O 2p states (bands) covalently hybridized with the t_{2g} and e_g states of Ti 3d orbitals, while peaks C and D are assigned to transitions from O 1s to O 2p antibonding states and O 2p-Ti 4sp hybridized states, respectively. The presence of feature E is usually taken as a signature of the long range order of TiO_2 structures [21,29]. Compared to the O K-edge XANES of standard anatase (D_{2d}), the splitting of peak D (into D_1 and D_2) together with the positive energy shifts of peaks C and E clearly shows the D_{2h} local symmetry of standard rutile. As for Ti_2O_3 standard, the difference between its TEY and PFY XANES at the O K-edge accords the analysis at the Ti $L_{3,2}$-edge XANES (**Figure 4-4a** and **4b**), indicating the surface oxidization of Ti_2O_3. In line with the results at the Ti $L_{3,2}$-edge XANES, O K-edge XANES of NT450 and NNT450 presents the homogeneous anatase fine structure in the whole NTs (both on the surface and in the bulk). By contrast, NNT together with APNT develops a TEY XANES pattern similar to oxidized Ti_2O_3 with their broad features C and D as well as the absence of peak E (*i.e.*, a sign of short rang order). Note that the stronger intensity of peak B than A in Ti_2O_3 suggests its different Ti-O coordination with the surface structures of NNT and APNT [30]. Additionally, PFY XANES of NNT indicates its anatase nature, which is in agreement with the analysis at the Ti $L_{3,2}$-edge, further demonstrating that NNT is an anatase-core–amorphous-shell heterostructure.

The areas under the curve in the resonance just above the threshold of the Ti $L_{3,2}$-edge and O K-edge XANES represent the densities of the unoccupied states of orbitals being probed. For example, Ti 3d unoccupied states or d holes is proportional to the area under 2p-to-3d resonance at the Ti $L_{3,2}$-edge. Since the first two strong resonances A and B (**Figure 4-4c** and **4d**) at the O K-edge originate from electrons transitions from O 1s states to O 2p-Ti 3d hybridized unoccupied states [21], so areas under relevant resonances at both the Ti $L_{3,2}$-edge and the O K-edge are proportional to the unoccupied states of the Ti 3d character (d holes). Thus the larger the area, the higher the density of the Ti 3d unoccupied states, hence the higher the Ti oxidation state.

A detailed analysis has been performed by comparing the Ti $L_{3,2}$-edge and O K-edge XANES (normalized to unity at the same energy above the edge) of NNT to those of NNT450 and NT450. The results are shown in **Figure 4-5**, the areas underneath the Ti $L_{3,2}$-edge and O K-edge resonances integrated over the same region exhibits a trend of increasing intensity from NNT, NNT450 and NT450. Areas integrated from NNT450 are slightly lower than those of NT450 whereas the areas of NNT, especially revealed from the TEY XANES (**Figure 4-5a** and **5c**), are sharply reduced compared to those of the other two. Therefore, it is clear that the Ti oxidation state in both the amorphous shell and anatase core of NNT has been reduced from Ti^{4+}, especially in the amorphous shell. Additionally, the difference revealed by the TEY and PFY XANES of NNT at the Ti $L_{3,2}$-edge (**Figure 4-4a** and **4b**) and O K-edge (**Figure 4-4c** and **4d**) clearly demonstrates the dissimilar electronic structure of its amorphous shell and crystalline core. While the latter shows a long range order and typical characteristics of anatase TiO_2 with a slight reduction of Ti^{4+}, the former exhibits a more dramatic effect with the presence of a larger amount of Ti^{3+}. Accordingly, the production of those Ti^{3+} has been assigned to a color center and mainly responsible for visible light absorption [8,31-33], consistent with the dark black color of NNT and its continuous UV-to-near-infared absorption spectrum (**Figure 4-3**).

To further confirm the average chemical compostion of the reduced amorphous surface of NNT, X-ray photoelectron spectroscopy (XPS) was performed. Note that the typical detection depth of XPS is on the order of ~ nanometers [34], which is only sensitive to

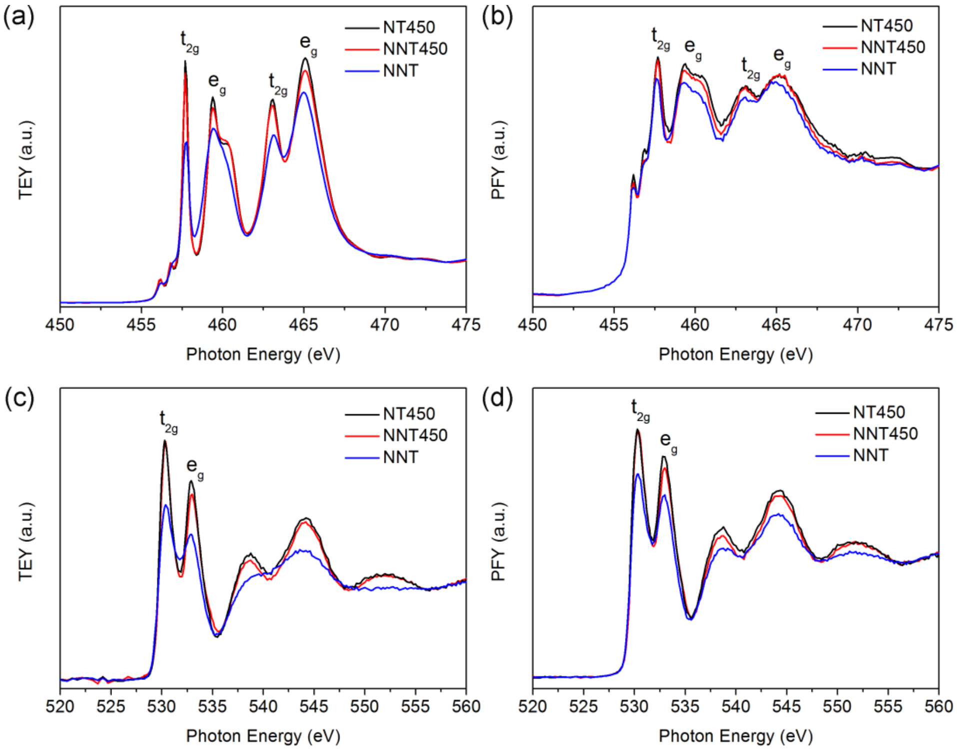

Figure 4-5 Overlay of Ti $L_{3,2}$-edge (a) TEY and (b) PFY XANES, and O K-edge (c) TEY and (d) PFY XANES spectra of NT450, NNT450 and NNT.

the amorphous shell (**Figure 4-1*l***). Three regions of interest (Ti, O and N) were mainly examined and their corresponding spectra are shown in **Figure 4-6**. A comparison among the normalized Ti 2p XPS spectra of NNT, NNT450 and NT450 is illustrated in **Figure 4-6a**. A sharp peak centered at ~458.9 eV and a broader peak at ~464.7 eV are the characteristic Ti $2p_{3/2}$ and $2p_{1/2}$ peaks of Ti^{4+}, rspectively [1,35,36], they are clearly presented in both NT450 and NNT450. In contrast, NNT shows a distinct shift to the lower binding energy region compared to the former two, indicating Ti of a lower oxidation state is present in the amorphous surface layer. To unravel this difference, we subtracted the normalized Ti 2p spectrum of NNT (black) by that of NT450 (blue) and the difference curve is shown at the bottom of **Figure 4-6a** [35]. Clearly, two peaks are located at 458.2 and 463.7 eV in the difference spectrum, which are in accord with the characteristic Ti $2p_{3/2}$ and $2p_{1/2}$ peaks of Ti^{3+} [35,37]. To evaluate the amount of Ti^{3+} ions in the amorphous shell of NNT, deconvolution of its Ti 2p XPS (**Figure 4-6b**) shows a Ti^{3+}/Ti^{4+} atomic ratio of ~1.2, illustrating that the amorphous shell has a composition close to the Magneli phase of Ti_4O_7. For the sake of comparison, Ti 2p XPS deconvolutions of NNT450 (**Figure 4-6c**) and NT450 (**Figure 4-6d**) are also shown. As expected, only pure Ti^{4+} states are found in these two speices.

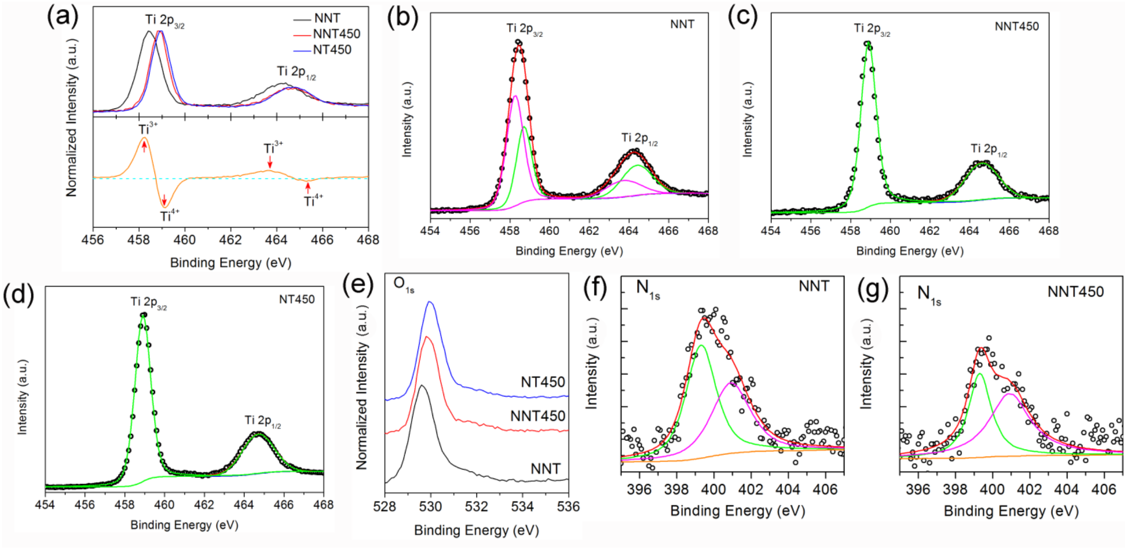

Figure 4-6 (a) Overlay of normalized (to maximum intensity) Ti 2p XPS spectra of NNT (black), NNT450 (red) and NT450 (blue) together with the difference spectrum by subtracting NNT with NT450. Curve fitting results of the Ti 2p XPS spectra of (b) NNT, (c) NNT450 and (d) NT450, of which the green peaks represent Ti^{4+} whereas the magenta fitted peaks correspond to the reduced Ti^{3+} species. (e) Display of normalized O 1s XPS spectra of NNT, NNT450 and NT450 where the spectra of the latter two are vertically shifted for clarity. N 1s XPS spectra of (f) NNT and (g) NNT450. Black circles are the experimental data while the red curves are the fitted XPS spectra in which the XPS spectra of NNT and NNT450 are deconvoluted into two peaks centered at 399.3 eV (green curve) and 400.9 eV (magenta curve). No N 1s signal is detected from NT450.

Figure 4-6e displays the O 1s XPS spectra of NNT, NNT450 and NT450. All samples show the asymmetry where the O 1s XPS spectrum of NT450 can be decomposed into a sharp peak at ~530 eV and a broad shoulder peak at ~531.4 eV, which have been assigned to be the characteristic peaks of TiO_2 and Ti-OH, respectively [1,35,36,38]. Moreover, a closer observation of the O 1s XPS spectra indicates a negative shift in binding energy of O in NNT, which is probably due to the more negative charge states of O by N incorporation (*via* NH_3 annealing) as the change of bonding environment from O-Ti-O to O-Ti-N, and O is more electronegative than N. Similar findings also have been reported before [33].

The N 1s XPS spectra of NNT and NNT450 (**Figure 4-6f** and **6g**) can be deconvoluted into two peaks at 399.3 eV and 400.9 eV. The former can be assigned to anionic N-doping in TiO_2 as O-Ti-N linkages (substitutional), while the latter is attributed to oxidized N in the form of Ti-O-N or Ti-N-O linkages (interstitial) [39,40]. No sign of TiN is observed as its typical binding energy value is at ~397 eV for N 1s states [31,39], consistent with XRD results in **Figure 4-1m**. The approximate atomic percentages of doped N in NNT and NNT450 are determined to be ~5.1 % and ~4.7 %, respectively, by calculating with individual peak areas of Ti, O and N, and their respective atomic sensitivity factor. The area ratio of substitutional N peak to the interstitial N peak for NNT is ~1.24, and this ratio decreases to ~0.72 for NNT450, suggesting that substitutional doping is dominant in NNT while interstitial doping is prevailing in NNT450.

To truly unveil the local structure and bonding of the incorporated N in TiO_2 matrix (both on the surface and in the bulk region), TEY and PFY XANES at the N K-edge are measured as shown in **Figure 4-7**. For standard TiN, there are two pre-edge features A and B, which is in accord with electronic transitions from N 1s to N 2p states covalently hybridized with t_{2g} and e_g states of the Ti 3d orbital, unequivocally providing strong evidence for Ti-N bonding. Above the edge, peaks C and D associate with transitions from N 1s to N 2p-Ti 4sp hybridized states [41]. By comparison, both the TEY and PFY spectra of NNT exhibit similar XANES profiles as TiN, suggesting the doping sites (both on the surface and in the bulk region) of N in TiO_2 lattice are mainly substitutional. *i.e.*, O^{2-} is substituted by N^{3-} with a bonding environment change from Ti-O-Ti to Ti-N-Ti. On the other hand, the absence of the two features A and B on the surface of NNT450 clearly indicates the absence of Ti-N bonding after NH_3 annealing. Instead, both of those two components are presented in the PFY XANES of NNT450 with an inverted intensity ratio of peak A/B compared to TiN, which is assigned to the formation of interstitial N_2

molecules which remains dissolved in the bulk of TiO_2 matrix by physical or chemical adsorption [41,42].

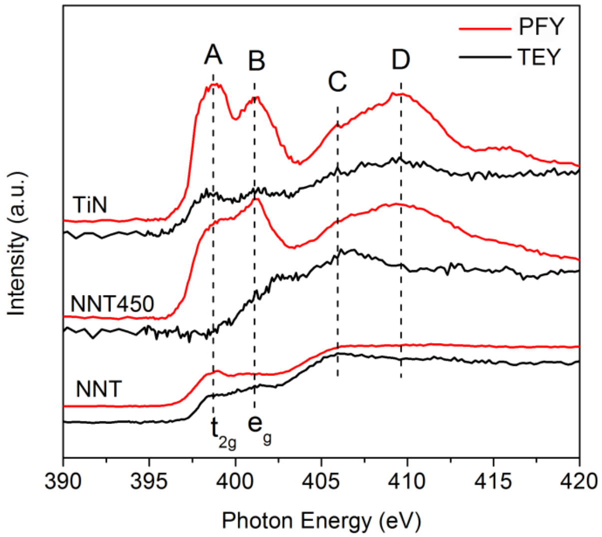

Figure 4-7 N K-edge XANES spectra of NNT and NNT450 in comparison with that of standard TiN recorded in both TEY and PFY modes.

As for the crystalline core of NNT, although it displays the similar anatase structure with NNT450 and NT450, as revealed by PFY XANES (**Figure 4-4b** and **4d**), the decrease of the density of Ti unoccupied states in the bulk of NNT (**Figure 4-5b** and **5d**) still shows its different electronic nature (e.g., oxygen-deficient TiO_2) with the other two. Hence, we further characterize the bulk of NNT, NNT450 and NT450 using bulk-sensitive resonant inelastic X-ray scattering (RIXS). As a photon-in–photon-out technique, RIXS usually can be used to characterize the bulk electronic structure (occupied densities of states) of material at a few micrometers by the collection of characteristic X-ray emission from valance to shallow core transition (L_α and K_α from Ti $L_{3,2}$-edge and O K-edge, respectively) upon the creation of the core hole with excitation channels at or in the vicinity just above the edge [19,43].

Figure 4-8 shows the four sets of RIXS spectra of NT450, NNT450 and NNT (bottom panel) with their corresponding excitation energies at the Ti L_3-edge XANES (top panel). All RIXS spectra are calibrated and displayed in an energy loss scale by subtracting their relevant excitation energy with the measured emission energy [19,43-45]. As noted in the

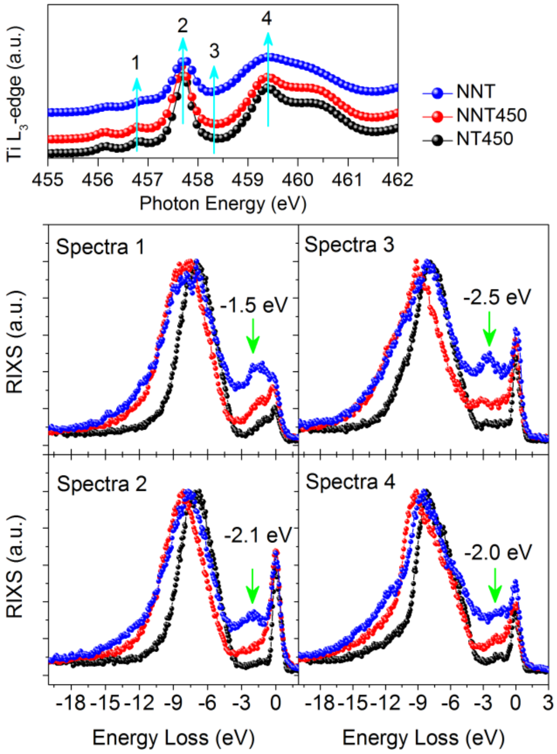

Figure 4-8 Ti 2p RIXS spectra (bottom) of NT450, NNT450 and NNT excited with selected photon energies corresponding to the Ti L_3-edge TEY XANES as shown on the top. The peak intensity of the four sets of RIXS spectra are normalized to their relevant Ti 3d→Ti 2p X-ray fluorescence.

literature [19,44], once the excitation energy reaches the Ti 2p absorption threshold, two types of inelastic emission features are present in the Ti 2p RIXS spectrum in addition to the the elastic peak with an energy loss at 0 eV. RIXS takes place in the regime of the cross over of the resonant Raman scattering (energy loss is a constant) and X-ray fluorescence (energy loss exhibits a disperson since fluorescence X-ray has a constant energy when excited above the threshold in the sudden regime) [19,43,44,46]. As shown in **Figure 4-8**, the presence of a series of peaks below the elastic RIXS peak at 0 eV pictures the inelastic RIXS characters. The broad feature with an energy loss scale from 4 eV to 18 eV is attributed to contributions from both the Ti 3d→Ti 2p X-ray fluorescence (constant emission energy) and associated charge transfer excitations (constant energy loss) from O 2p to Ti 3d states. Note that those two components overlap with excitation energies at the Ti L_3-edge, and will split into two once the excitation energy reaches the

Ti L_2-edge (not shown here) [19,44]. Most interestingly, a broad peak at ~2 eV is also observed in both NNT and NNT450 but it is weak or nearly absent in NT450.

With the absence of these low energy inelastic scattering peaks in NT450, a noticeable increase of those features is observed in NNT450 at the energy loss scale between 0 and 4 eV. A further sharp increase in intensity of those peaks can be seen in NNT, especially for spectra 1 and 3 where their excitation energies locate at the pre-edge and the non-resonant absorption region of Ti L_3-edge between t_{2g} (point 2) and e_g (point 4) resonances, respectively. Apparently, the emergence of those extra low inelastic scattering features is facilitated by N incorporation. Since RIXS is analogous to resonant Raman scattering which can detect energy transfers by electron transitions on the same atomic site [6], thus these low inelastic energy peaks at ~2 eV can be unambiguously traced to Ti d-d interband transtions from Ti^{3+} ions reduced from Ti^{4+} in TiO_2 upon N doping [19,44]; *i.e.* that the Ti 3d orbital is partially occupied as a pseudo-$3d^1$ system. Further evidence, both experimentally and theoretically, is provided by a Ti 2p RIXS study of TiF_3 ($3d^1$) showing an energy loss feature at ~2 eV [45]. Additionally, as suggested by previous works [12,19], the energy locations of point 1 and 3 are on the t_{2g} and e_g absorption resonances of Ti^{3+}, respectively. It explains the more intense d-d excitations observed in spectra 1 and 3 compared with spectra 2 and 4. The comparatively larger amount of N dopants in NNT than in NNT450 together with their dominant substitutional character disclosed in N 1s core level XPS (**Figure 4-6f** and **6g**) and N K-edge XANES (**Figure 4-7**), accounts for the higher intensity of the Ti^{3+} RIXS d-d transition feature in NNT. The slight energy loss variation (indicated by the green arrows) together with the broad character of these d-d excitation peaks suggest a distribution of as-obtained Ti^{3+} states [47]. It is believed that Ti^{3+} states in oxygen deficient TiO_2 nanomaterials act as the photoabsorption centers, where electronic transitions from Ti^{3+} intraband states to conduction band of TiO_2 results from light absorption in the visible [9,32,33]. Nevertheless, solid evidence regarding energy absorption by Ti^{3+} has not been provided experimently until a recent study by Wang *et al.* [32] using two-photon photoemission spectroscopy (2PPE). Alternatively, this work using RIXS also demonstrates the energy absorption by Ti^{3+}. *i.e.* that d-d excitations show a dispersive energy transfer of ~2 eV which mainly contributes to the visible light capture of NNT450 with a broad absorption at ~600 nm (Figure 3), and the comparatively large amount of Ti^{3+} bulk species of NNT coupled with the amorphous shell establishes the synergistic interaction with a continuous light absorption from UV to near-infrared.

Until now, conventional wisdom treats the disordered TiO_2 surface as the direct but nonspecific origin for the band gap narrowing and the corresponding visble light absorption of black TiO_2. In contrast to this notion, our results show that the amorphous shell has an average chemical composition of Ti_4O_7, which is a small band gap titanium oxide and establishes the synergistic photoabsorption with the bulk, oxygen deficient anatase TiO_2. We propose here that the composition of the amorphous surface of NNT resembles a highly disordered Magneli phase of Ti_4O_7, instead of the stoichiometric TiO_2 (TiO_{2-x}) as it is commonly referred to. Because surface Ti^{3+} in stoichiometric TiO_2 is not stable in air as it is easily oxidized, so only its bulk Ti^{3+} is observed accounting for the enhanced visible light absorption [8,9,48]. Consistent evidence is shown in NNT450 of this work where only bulk Ti^{3+} from N doping is detected by Ti 2p RIXS. Those bulk Ti^{3+} species exhibit an absorption energy associated with its visible light absorption. On the other hand, both TEY XANES (**Figure 4-4a** and **4c**) and Ti 2p XPS (**Figure 4-6a** and **6b**) of NNT suggest that an equal amount of Ti^{3+} and Ti^{4+} is stablizing the NT surface. The black color of NNT (**Figure 4-3**) unequivocally coincides with the high stability of Ti^{3+} in the amorphous shell as it is known to be the color center of titanium oxide species [8,32,33]. Therefore, the formation of Ti_4O_7 can be justified. First of all, Ti_4O_7 with its mixed nature of Ti^{3+} and Ti^{4+} can preserve its Ti^{3+} with high stability. In fact, Magneli phase Ti_4O_7 can be obtained *via* reduction of both anatase and rutile TiO_2 [49,50], which makes our proposal more convincing since this Ti_4O_7 layer is grown on the top of bulk anatase TiO_2. Second, whereas the attribution of band gap narrowing of black TiO_2 to the merging of band tail states with the valence band maximum and conduction band minimum, is still controversial [1,12], our proposed Ti_4O_7 is more resonable due to its much smaller band gap (~1.5 eV) than anatase TiO_2 (~3.2 eV) [51]. Accordingly, the excellent visible light capture of NNT can mainly be attributed to the small band gap absorption of Ti_4O_7 in the amorphous surface synergetically coupled with photoabsorption by the distributed bulk Ti^{3+} intraband states. Namely, it is likely that the amorphous surface layer stablized by the anatase core provides a distribution of electronic states between these two band gap energies, leading to continuous absorption in the UV-to-near-infrared wavelength region. Admittedly, the involvement of slightly doped N (**Figure 4-6f**) on the surface of NNT can also contribute to its visible-infrared absorption as secondary [3,9,31,52].

It is also important to mention that the crystallization of amorphous NTs in ambient NH_3 is the key for this functional dark black TiO_2 NTs preparation, in which amorphous NTs (APNT) prepared by NH_4F-containing electrolyte have a large amount of F^- ions included. In order to reveal the chemical nature of these F^- ions in APNT and, hence, to address the unique capability of the amorpous form with F^- ions for the formation of black core-shell TiO_2 NT, the surface chemical states of APNT and NT450 were comparatively examined by X-ray photoelectron spectroscopy (XPS), in which the Ti 2p and F 1s were tracked. As shown in **Figure 4-9a**, the Ti 2p XPS spectrum of NT450, as mentioned above (**Figure 4-6a**), displays two peaks at 458.9 eV and 464.7 eV, corresponding to the Ti^{4+} $2p_{3/2}$ and $2p_{1/2}$, respectively. For APNT, the two Ti 2p peaks are broader and skew towards lower binding energy. Curve fitting of the XPS profile of APNT reveals shoulder features at 458.2 eV and 463.7 eV, which are attributed to the $2p_{3/2}$ and $2p_{1/2}$ of Ti^{3+}, respectively, as suggested in **Figure 4-6a**. The F 1s XPS spectra of APNT and NT450 are illustrated in **Figure 4-9b**. It is clear that APNT displays an intense F 1s peak at 684.3 eV associated with surface fluorination of TiO_2 (formation of surface Ti-F bond) [53,54], whereas the F 1s XPS signal from NT450 becomes unnoticeable, indicating that all the F species are driven out from the NT surface after annealing at 450 ℃. The formation of surface Ti-F bonds in APNT is not a total surprise considering the rich F^- environment during TiO_2 NT formation and the almost identical ionic radius between O^{2-} and F^- ions. Concomitantly, a compatible amount of Ti^{3+} surface states are formed to maintain the electronuetrality of $TiO_{2-x}F_x$ system according to the polaron theory [53].

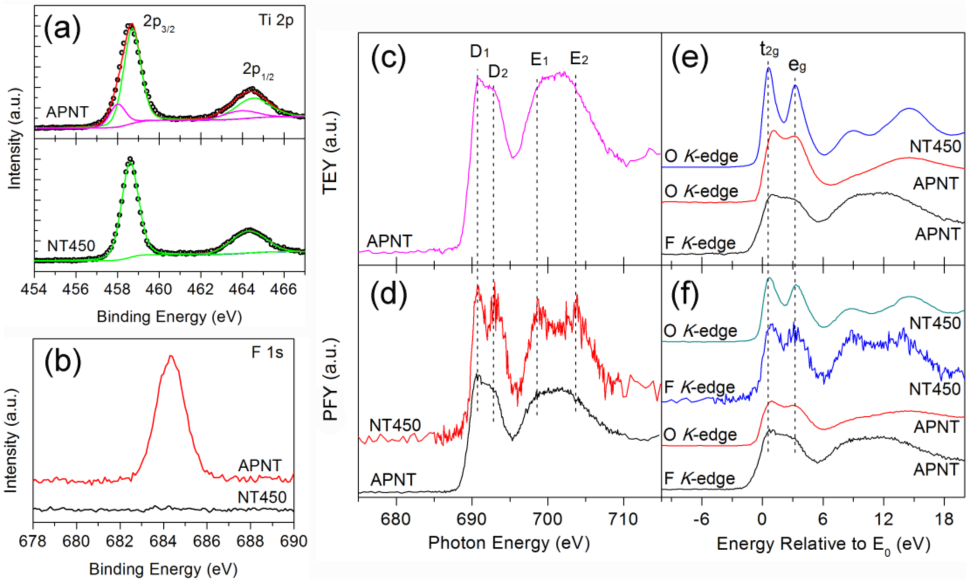

Figure 4-9 (a) Normalized Ti 2p XPS spectra of APNT (top) and NT450 (bottom), in which the black circles are the experimental data whereas the solid lines are fitted XPS spectra. (b) F 1s XPS spectra of APNT and NT450. (c) TEY and (d) PFY XANES of APNT and NT450 recorded at the F K-edge. Alignments between O K-edge and F K-edge XANES of APNT and NT450 are recorded in (e) TEY and (f) PFY by subtracting the O K-edge and F K-edge photon energies to the O 1s and F1s absorption thresholds (E_0), respectively. The lack of the TEY spectrum at the F K-edge of NT450 in both (c) and (e) is due to the release of F^- ions on the surface of NT450 after annealing.

To further gain insights of the doping site (*i.e.*, surface or bulk) and the chemical environment of F in the titania matrix, XANES at the F K-edge in comparison with those at the O K-edge are recorded in both TEY (surface-sensitive) and PFY (bulk-sensitive) modes as shown in **Figure 4-9c** ~ **9f**. Two interesting observations are noted. First, **Figure 4-9c** and **9d** show that while the F K-edge XANES of APNT is collected in both detection modes, only PFY XANES of F is present in NT450 albeit with poor statistics. It indicates that F^- ions are self-doped both on the surface and in the bulk of the amorphous structure (APNT) during anodization whereas only a small amount of self-doped F^- ions is left in the bulk of the anatase phase (NT450) after annealing at 450 °C. Second, as the electronic transition from F 1s to F 2p is involved in the F K-edge XANES, four resonant peaks are shown. Both the unresolved twofold structures (D_1 and D_2; $E_1$and E_2) in APNT are well resolved after phase transformation from amorphous to anatase. The spectral pattern of the F K-edge shares the similar XANES profile with that of the O K-edge XANES when both sets of spectra are calibrated to the absorption threshold (inflection point of the rising edge). As shown in **Figure 4-9e** and **9f**, the XANES at the F K-edge and O K-edge are well aligned, providing concrete evidence for the formation of Ti-F bonds with F^- ions being in the similar local environment as O^{2-} ions, *i.e.*, the substitutional replacement of O^{2-} by F^- ions. Thus the origins of the two peaks D_1 and D_2 can be unambiguously assigned to electronic transitions from F 1s to F 2p states hybridized with Ti t_{2g} and e_g manifolds (unoccupied densities of states of F 2p-Ti 3d character), respectively, whereas the twofold features E_1 and E_2 are attributed to electronic transitions from F 1s to F 2p states covalently hybridized with Ti 4sp characters, as in the case of O K-edge XANES in TiO_2 as demonstrated in **Figure 4-4c** and **4d**.

Henceforth, the above fluorine-related analysis suggests that the as-grown amorphous NTs using NH_4F as the electolye are substitutionally self-doped with F^- ions both on the surface and in the bulk titania lattice. The release of those F species by breaking the Ti-F bonds can be achieved by thermal annealing (e.g., 450 ℃ in this study). Thus annealing of amorphous NTs in NH_3 (oxygen deficient) atomosphere can help the creation of massive oxygen vacancies *via* the breakage of Ti-F bonds. As a result, compared to N doping in pure TiO_2, the introduction of N dopant in oxygen deficient TiO_2 lattice during the removal of F will become more convenient, since these two processes occur simultaneously during NH_3 annealing. Concomitantly, N incorporation into TiO_2 lattice *via* O subsittution will significantly lower the formation energy of oxygen vacancy to maintain the charge neutralization [9]. Oxygen vacancies in TiO_2 from all these pathways will propagate and accumulate toward the NT surface during crystallization [12]. Consequently, Ti_4O_7 is attained on the NT surface once the stoichiometric TiO_2 no longer sustains due to the excessive oxgyen vacancies. Therefore, the amorphous nature of the NT surface mainly results from two processes: first, N doping together with oxygen vacancy formation causes the local distortion of TiO_6; second, the accumulation of massive oxygen vacancies on the surface region could prevent its crystalization (long range ordering) [20], thus the NT surface keeps its original amorphous character with a short range order although the connectivity of TiO_6 will change adopting transitional configuration between the two (TiO_2 and Ti_4O_7).

4.4 Conclusions

We have suceeded in using NH_3 annealing of the as-grown TiO_2 NTs prepared by Ti anodization to fabricate black TiO_2 NTs. Compared with the well-crystallized anatase TiO_2 NTs annealed at ambient air, then in NH_3, black TiO_2 NTs exhibit degradation in crystallinity on the surface, having a heterostructure of anatase core wrapped by an amorphous shell. This unique configuration of black TiO_2 NTs exhibits extraordinary light absorption behaviour covering continuously the wavelength from UV to near-infrared. TEY (surface-sensitive) and PFY (bulk-sensitive) XANES analysis show that Ti in both the amorphous shell and the anatase core are heavily reduced. The former displays severe distortions of TiO_6 octahedra with a short range order, whereas the latter maintains crystalline anatase. XPS confirms the TEY XANES result which shows that the chemical composition is Ti_4O_7 in the amorphous shell. Ti 2p RIXS provides the concrete evidence for the presence of bullk Ti^{3+} by the observation of d-d excitations which is absent in defect-free TiO_2. The energy loss at ~2 eV with broadening corresponds to the broad visible light absorption at ~600 nm. Consequently, the assembly of the Ti^{3+} containing core of the anatase TiO_2-x NT and its amorphous Ti_4O_7 surface establishes the significance of the synergistic effect responsible for the light absorption of black TiO_2 NTs. The key observation is the formation of amorphous Ti_4O_7 on the NT surface as a result of excessive accumulation of oxygen vacancies, which has the high stability for preserving surface Ti^{3+} and efficient light capture due to its variable band gap energy. This work provides new insights for the chemical nature of core–shell black TiO_2 NTs and thus will help develop more efficient nanostructures suitable for solar energy utilization. For example, the optimization of the light capture of this core-shell system is underway, in which the variation of N dopant concentration and the thickness of the amorphous shell will be examined by controlling the reaction temperature, time and the NH_3 gas flow.

4.5 References

[1] X. B. Chen, L. Liu, P. Y. Yu, and S. S. Mao, *Science* **331**, 746 (2011).

[2] M. D. Ye, J. J. Gong, Y. K. Lai, C. J. Lin, and Z. Q. Lin, *J. Am. Chem. Soc.* **134**, 15720 (2012).

[3] R. Asahi, T. Morikawa, T. Ohwaki, K. Aoki, and Y. Taga, *Science* **293**, 269 (2001).

[4] G. M. Wang, H. Y. Wang, Y. C. Ling, Y. C. Tang, X. Y. Yang, R. C. Fitzmorris, C. C. Wang, J. Z. Zhang, and Y. Li, *Nano Lett.* **11**, 3026 (2011).

[5] Y. H. Hu, *Angew. Chem., Int. Ed.* **51**, 12410 (2012).

[6] C. P. Cheney *et al.*, *Phys. Rev. Lett.* **112**, 036404 (2014).

[7] Y. Q. Gai, J. B. Li, S. S. Li, J. B. Xia, and S. H. Wei, *Phys. Rev. Lett.* **102**, 036402 (2009).

[8] S. Hoang, S. P. Berglund, N. T. Hahn, A. J. Bard, and C. B. Mullins, *J. Am. Chem. Soc.* **134**, 3659 (2012).

[9] S. Livraghi, M. C. Paganini, E. Giamello, A. Selloni, C. Di Valentin, and G. Pacchioni, *J. Am. Chem. Soc.* **128**, 15666 (2006).

[10] A. Naldoni, M. Allieta, S. Santangelo, M. Marelli, F. Fabbri, S. Cappelli, C. L. Bianchi, R. Psaro, and V. Dal Santo, *J. Am. Chem. Soc.* **134**, 7600 (2012).

[11] L. Liu, P. Y. Yu, X. B. Chen, S. S. Mao, and D. Z. Shen, *Phys. Rev. Lett.* **111**, 065505 (2013).

[12] M. K. Tian *et al.*, *ACS Nano* **9**, 10482 (2015).

[13] N. Liu *et al.*, *Angew. Chem, Int. Ed.* **53**, 14201 (2014).

[14] X. Chen, D. X. Zhao, K. W. Liu, C. R. Wang, L. Liu, B. H. Li, Z. Z. Zhang, and D. Z. Shen, *ACS Appl. Mater. Interfaces* **7**, 16070 (2015).

[15] H. T. Fang, M. Liu, D. W. Wang, T. Sun, D. S. Guan, F. Li, J. G. Zhou, T. K. Sham, and H. M. Cheng, *Nanotechnology* **20**, 7, 225701 (2009).

[16] G. K. Mor, K. Shankar, M. Paulose, O. K. Varghese, and C. A. Grimes, *Nano Lett.* **6**, 215 (2006).

[17] P. L. Yan, G. J. Liu, C. M. Ding, H. X. Han, J. Y. Shi, Y. Gan, and C. Li, *ACS Appl. Mater. Interfaces* **7**, 3791 (2015).

[18] T. Regier, J. Paulsen, G. Wright, I. Coulthard, K. Tan, T. K. Sham, and R. I. R. Blyth, *AIP Conf. Proc.* **879**, 473 (2006).

[19] A. Augustsson, A. Henningsson, S. M. Butorin, H. Siegbahn, J. Nordgren, and J. H. Guo, *J. Chem. Phys.* **119**, 3983 (2003).

[20] H. Q. Tan, Z. Zhao, M. Niu, C. Y. Mao, D. P. Cao, D. J. Cheng, P. Y. Feng, and Z. C. Sun, *Nanoscale* **6**, 10216 (2014).

[21] J. Li, L. J. Liu, and T. K. Sham, *Chem. Mater.* **27**, 3021 (2015).

[22] J. P. Crocombette and F. Jollet, *J. Phys.: Condens. Matter* **6**, 10811 (1994).

[23] G. S. Henderson, X. Liu, and M. E. Fleet, *Phys. Chem. Miner.* **29**, 32 (2002).

[24] F. M. F. Degroot, J. C. Fuggle, B. T. Thole, and G. A. Sawatzky, *Phys. Rev. B* **42**, 5459 (1990).

[25] S. O. Kucheyev *et al.*, *Phys. Rev. B* **69**, 245102 (2004).

[26] C. X. Kronawitter *et al.*, *Nano Lett.* **11**, 3855 (2011).

[27] T. K. Sham, *J. Chem. Phys.* **83**, 3222 (1985).

[28] E. Stoyanov, F. Langenhorst, and G. Steinle-Neumann, *Am. Mineral.* **92**, 577 (2007).

[29] J. G. Zhou *et al.*, *J. Mater. Chem.* **19**, 6804 (2009).

[30] J. Li, Z. Q. Wang, A. K. Zhao, J. Wang, Y. Song, and T. K. Sham, *J. Phys. Chem. C* **119**, 17848 (2015).

[31] Z. D. Li, F. Wang, A. Kvit, and X. D. Wang, *J. Phys. Chem. C* **119**, 4397 (2015).

[32] Z. Q. Wang *et al.*, *J. Am. Chem. Soc.* **137**, 9146 (2015).

[33] J. Wang, D. N. Tafen, J. P. Lewis, Z. L. Hong, A. Manivannan, M. J. Zhi, M. Li, and N. Q. Wu, *J. Am. Chem. Soc.* **131**, 12290 (2009).

[34] M. P. D. Seah, W. A., *Surf. Interface Anal.* **1**, 10 (1979).

[35] X. H. Lu, G. M. Wang, T. Zhai, M. H. Yu, J. Y. Gan, Y. X. Tong, and Y. Li, *Nano Lett.* **12**, 1690 (2012).

[36] T. K. Sham and M. S. Lazarus, *Chem. Phys. Lett.* **68**, 426 (1979).

[37] F. Werfel and O. Brummer, *Phys. Scr.* **28**, 92 (1983).

[38] X. H. Lu, D. Z. Zheng, T. Zhai, Z. Q. Liu, Y. Y. Huang, S. L. Xie, and Y. X. Tong, *Energy Environ. Sci.* **4**, 2915 (2011).

[39] T. C. Jagadale, S. P. Takale, R. S. Sonawane, H. M. Joshi, S. I. Patil, B. B. Kale, and S. B. Ogale, *J. Phys. Chem. C* **112**, 14595 (2008).

[40] M. Sathish, B. Viswanathan, R. P. Viswanath, and C. S. Gopinath, *Chem. Mater.* **17**, 6349 (2005).

[41] L. Soriano, M. Abbate, H. Pen, M. T. Czyzyk, and J. C. Fuggle, *J. Electron Spectrosc. Relat. Phenom.* **62**, 197 (1993).

[42] Y. F. Hu, T. K. Sham, Z. Zou, G. Q. Xu, L. Chan, B. W. Yates, and G. M. Bancroft, *J. Synchrotron Radiat.* **8**, 860 (2001).

[43] M. M. van Schooneveld *et al.*, *J. Phys. Chem. Lett.* **4**, 1161 (2013).

[44] T. Higuchi *et al.*, *Phys. Rev. B* **60**, 7711 (1999).

[45] M. Matsubara, T. Uozumi, A. Kotani, Y. Harada, and S. Shin, *J. Phys. Soc. Jpn.* **69**, 1558 (2000).

[46] J. Li, C. H. Liu, Y. F. Ye, J. F. Zhu, S. D. Wang, J. H. Guo, and T. K. Sham, *J. Phys. Chem. C* **120**, 4623 (2016).

[47] K. J. Zhou, M. Radovic, J. Schlappa, V. Strocov, R. Frison, J. Mesot, L. Patthey, and T. Schmitt, *Phys. Rev. B* **83**, 201402 (2011).

[48] Y. Wang, C. X. Feng, M. Zhang, J. J. Yang, and Z. J. Zhang, *Appl. Catal., B* **104**, 268 (2011).

[49] C. Tang, D. B. Zhou, and Q. Zhang, *Mater. Lett.* **79**, 42 (2012).

[50] C. Hauf, R. Kniep, and G. Pfaff, *J. Mater. Sci.* **34**, 1287 (1999).

[51] X. Zhong, I. Rungger, P. Zapol, and O. Heinonen, *Phys. Rev. B* **91**, 115143 (2015).

[52] S. Kurian, H. Seo, and H. Jeon, *J. Phys. Chem. C* **117**, 16811 (2013).

[53] A. M. Czoska, S. Livraghi, M. Chiesa, E. Giamello, S. Agnoli, G. Granozzi, E. Finazzi, C. Di Valentin, and G. Pacchioni, *J. Phys. Chem. C* **112**, 8951 (2008).

[54] W. Q. Fang, X. L. Wang, H. M. Zhang, Y. Jia, Z. Y. Huo, Z. Li, H. J. Zhao, H. G. Yang, and X. D. Yao, *J. Mater. Chem. A* **2**, 3513 (2014).

Chapter 5

5 Revealing the Synergy of Palladium-Decorated Titania Heterostructure for Enhanced Photoactivity

5.1 Introduction

As arguably one of the most versatile semiconductors, TiO_2 has drawn a great deal of attentions due to its low-cost, non-toxic and superior photocatalytic properties among many other desirable properties. These properties of TiO_2 make it a robust material for solar cells [1-3], and photocatalysis [4-6] applications among many others [7-13]. Particularly, one-dimensional (1D) TiO_2 nanomaterials, such as nanowires (NWs), nanorods (NRs), nanobelts (NBs) and nanotubes (NTs) are of great scientific interests due to their unique architecture and associated intrinsic properties which can effectively improve photocatalytic efficiency [14,15]. Of the above mentioned morphologies, TiO_2 NTs have been widely used as the effective 1D nanostructure to enhance photocatalytic property of TiO_2. This is because the nanotubular structure can facilitate electron mobility along the tube axis, thus greatly reducing interface recombination [1]. However, the intrinsic defects (e.g., oxygen vacancies) within crystalline TiO_2 NTs impose significant restrictions on their photocatalytic performance. Recently, construction of TiO_2 NTs-based heterojunctions with noble metals attract great attention in photocatalysis, exemplars using silver, gold and platinum achieve the great successes [16-18]. The reason is that once the TiO_2 absorbs light and produces electrons and holes, the involvement of noble metals which have strong electron affinity will be the electron trap sites, thus retarding the recombination of photo-excited electron–hole pairs to mediate photocatalytic performance. In addition, palladium, as another noble metal, has been widely used as an industrial photocatalyst. For example, the decoration of Pd onto TiO_2 has been founded recently to retard the electron–hole recombination, thus enhancing photocatalysis in water-splitting [6].

*A version of this chapter has been published in *J Phys. Chem. C* **119**, 2222 (2015).

To achieve the synergetic effect between Pd and TiO_2 NTs for the design of efficient photocatalyst, the control of physical and chemical properties of TiO_2 NTs as a substrate is crucial. The morphology and crystal phase of TiO_2 NTs are the top two key factors for Pd modification and photocatalysis performance. While TiO_2 NTs synthesized under conventional techniques like sol-gel [19,20] and hydrothermal method [21,22] suffer the severely morphological limitation (disordered nanostructures and small surface area) resulting in the fast recombination of photoelectrons on the conduction band and holes on the valence band of TiO_2. In contrast, electrochemical anodization, as a productive and growth-controllable synthesis technique of TiO_2 NTs, can grow vertically aligned TiO_2 NTs on Ti substrate in only one direction. These anodic NTs can provide not only well-ordered unidirectional electrical channel but also a large surface area, contributing to the superior photocatalytic properties [4-6]. Since the photocatalytic performance of TiO_2 NTs is particularly related to its geometry and alignment, TiO_2 NTs with smooth top surface and good nanotubular arrangement are desired to further enhance the photoactivities. However, it is an experimental challenge to obtain the ideal geometry prepared by a single step anodization, in which the ideal NT morphology can be hardly achieved and the disordered architecture severely limits the photocatalytic properties of TiO_2 NTs [4]. Therefore a multi-step anodization method is widely used for TiO_2 NTs growth since the ordered hexagonal imprints can be left behind on Ti substrate after the removal of the previously anodized film. Subsequently, the following NTs can grow favorably along with these hexagonal imprints, leading to the extremely ordered TiO_2 NTs which show the superior photocatalytic performance and can be used as the ideal substrate for noble metal decoration [4,6].

In addition, anatase and rutile are the two well-known and photoactive phases of TiO_2. The different distortions of the octahedral environment at the Ti site result in the local symmetry D_{2d} and D_{2h} for anatase and rutile, respectively. While rutile (density 4.23 g cm^{-3}) is the thermodynamically stable phase, the metastable anatase phase (density 3.78 g cm^{-3}) is the more preferable phase in nanoscale and possesses an overall lower surface energy, thus anatase is more bioactive and robust for photocatalysis. Usually, the as-prepared TiO_2 NTs have the amorphous structure under room temperature anodization and can be crystallized to different phases (anatase and rutile) using a thermo-controllable method via annealing at different temperatures. The amorphous to anatase transformation temperature, which is mostly dependent on the morphology and defects of TiO_2, varies from 200 ℃ ~ 600 ℃ and a better crystallinity can be achieved using a higher annealing temperature [23,24]. However, the anatase phase will transform to rutile phase if the annealing temperature is too high whence the NTs will collapse and shrink to form the compact rutile structure [25]. Thus the phase control of TiO_2 NTs is a very important issue because different phase can result in a different photo-reaction mechanism. Previous studies indicate that anatase phase of TiO_2 is more stable in closely packed NTs than in loosely packed ones. For example, NTs synthesized by a multi-step anodization can retard the anatase-to-rutile phase transformation temperature to as high as 650℃ [4] while NT prepared by single-step anodization shows a noticeable rutile phase and becomes rutile dominant after annealing at 500℃ and 600℃, respectively [25]. Therefore, a multi-step electrochemical anodization method can be used to grow unidirectionally ordered TiO_2 NTs and becomes an easier way to control and retain the anatase phase. The obtained NT structure is highly favorable for Pd modification to achieve a better photocatalytic performance [6].

It is well documented that the existence of Schottky potential barrier at the interface between Pd NPs (metal) and TiO_2 (semiconductor) facilitates electron transfer from the conduction band of TiO_2 to Pd as the electron affinity of anatase (~4.2 eV) [26] is lower than the work function of Pd (~5.12 eV) [27], which can effectively reduce the electron–hole recombination so that enhanced photoactivity can be achieved [6,28]. Although many works have been reported to achieve superior photocatalytic performance of TiO_2 upon Pd decoration [6,29-31], to the best of our knowledge, a comprehensive understanding of the synergetic effect between noble metal and TiO_2 is lacking. Thus the objective of this work is to provide insights into electronic structure and its interplay with optical properties of Pd coated TiO_2 NTs.

Herein, this chapter reports the XAFS and XEOL studies of Pd decorated TiO_2 NTs prepared under controlled conditions to reveal the synergetic effects of vertically aligned TiO_2 NTs and uniformly coated Pd NPs through the analysis of Ti $L_{3,2}$-edge, O K-edge, Pd L_3- and K-edge as well as related optical luminescence excited by X-rays. In addition, RIXS is also used to pinpoint the effect of Pd modification on the Ti 3d states via d-d transitions analysis.

5.2 Experimental Section

5.2.1 Material Synthesis

Highly ordered TiO_2 NTs were prepared by electrochemical anodization using a custom-made two-electrode cell. A Ti metal foil (2 cm × 0.5 cm, 0.1 mm thick, Goodfellow) was used as the anode for NT growth while a Pt wire was the cathode. During the anodic oxidation process, 0.3 wt. % of ammonium fluoride (NH_4F, ACS, 98.0% min, Alfa Aesar) and 2 vol. % of deionized water together with ethylene glycol were used as the electrolyte. In order to grow an ideal nanotubular structure for palladium deposition, a two-step anodization method was used: Ti foil was firstly anodized at 50 V (Hewlett-Packard-6209B DC power supply) for 4 h, and ultrasonically rinsed in 1 M HCl to peel off the first layer. Subsequently, a second anodization was performed at 50 V for 30 min to obtain the vertically aligned NTs. The as-prepared NTs (APNT) attached on Ti foil were crystalized through annealing at 450 ℃ for 2 h (denoted as NT450).

A hydrothermal method [6] was used for palladium modification. Briefly, a 13 ml solution consisting of 150 mg of polyvinylpyrrolidone (PVP, average M_w ~55,000, Sigma-Aldrich), 50 mg of sodium iodide (NaI, ACS reagent, > 99.5%, Sigma-Aldrich) and 1.3 mg of palladium chloride ($PdCl_2$, ~99%, Sigma-Aldrich) together with NT450 were transferred into a 30 ml Teflon-lined stainless-steel autoclave and then heated at 180 ℃ for 2 h under sealing. Subsequently, the palladium coated NTs (henceforth denoted as PCNT450) were washed with ethanol and dried with N_2 gas.

5.2.2 Material Characterization

The morphology of NT450 and PCNT450 was characterized using scanning electron microscopy (SEM, LEO 1540XB), X-ray diffraction (XRD) spectra were collected using a Rigaku rotating-anode X-ray diffractometer with Co K_α radiation from 2-82 ° with a scan rate of $2\theta = 10° \text{ min}^{-1}$. A CHI 832a potentiostat (CH Instruments, Austin TX) was used for the photoelectrochemical (PEC) measurements using a three-electrode assembly in 1 M KOH electrolyte. Of which NT specimen (i.e., NT450 or PCNT450) attached on Ti foil was directly used as a working electrode (a constant photoactive area exposed to simulated solar light was ensured by a mask using resistive polyimide tape) [32], whereas a platinum coil and a standard calomel electrode (SCE) were utilized as the counter and reference electrodes, respectively. During the PEC test, a 150 W Newport lamp with an AM 1.5D filter was applied as the light source, and a ThorLabs SC10 shutter was employed to produce a square wave light stimulus. For linear sweep voltammetry (LSV) measurements, photocurrent was measured with a linear sweep voltage from -0.4 V to 0.4 V with a scan rate of 5 mV s^{-1}. Meantime, a chopped light with a frequency of 0.333 Hz was applied during the test. Chronoamperometry test was performed with chopped light at 0 V versus SCE in 1 M KOH. The decay *i-t* profiles were also measured at 0 V versus SCE in 1 M KOH with light switched from on to off at the beginning of the decay *i-t* curve collection.

XAFS spectra were recorded at the Canadian Light Source (CLS) located at the University of Saskatchewan (Saskatoon, SK, Canada). The Ti $L_{3,2}$-edge and O K-edge were obtained on the Spherical Grating Monochromator (SGM, $E/\Delta E > 5000$) beamline [33]. Pd L_3-edge was measured on the Soft X-Ray Microcharacterization Beamline (SXRMB, $E/\Delta E > 5000$) [34] while Pd K-edge was collected on the Hard X-ray Micro Analysis (HXMA, $E/\Delta E > 5000$) beamline [35]. The surface-sensitive total electron yield (TEY) and bulk-sensitive partial fluorescence yield (PFY) were used for absorption spectra collection. An Ocean Optics QE 65000 spectrometer was used for tracking XEOL spectra during the XAFS spectra collection (i.e., XAFS and XEOL were measured simultaneously by using different detectors). Photoluminescence yield (PLY), as a reflection of XEOL intensity variation which is also treated as optical-XANES, was tracked as the excitation energy tuned from below to above the edge of interest. All spectra were normalized to the incident photon flux. The RIXS spectra of NT450 and PCNT450 were collected at beamline 8.0.1 at the Advanced Light Source (ALS), Lawrence Berkeley National Laboratory (LBNL). Ti 2p RIXS spectra were measured using a high-resolution grazing incidence grating spectrometer with a resolution of 0.4 eV [36].

5.3 Results and Discussion

5.3.1 SEM, XRD and Photoactivity

SEM images of NT450 are shown in **Figure 5-1a** and **1b**, the vertically aligned NTs have an inner tube diameter of ~ 60 nm with an average wall thickness of ~ 25 nm. After palladium modification (**Figure 5-1c** and **1d**), the NPs with the diameter of ~ 5 nm are uniformly deposited on the orifice, the inner and outer tube walls without changing the morphology of NTs. XRD measurements were carried out to examine the crystal structure of NT specimens. As shown in **Figure 5-1e**, it is apparent that the structure of the APNT is amorphous, so only diffraction signal from Ti substrate is observed. After annealing at 450℃, both NT450 and PCNT450 present diffraction patterns in line with the anatase TiO_2 structure. In addition, a noticeable palladium diffraction peak (200) is located at $2\theta = 55.5°$ in PCNT450 and no other additional Pd peaks are detected. It suggests that the size of Pd NPs deposited on the surface of NTs is very small, which is consistent with the SEM result.

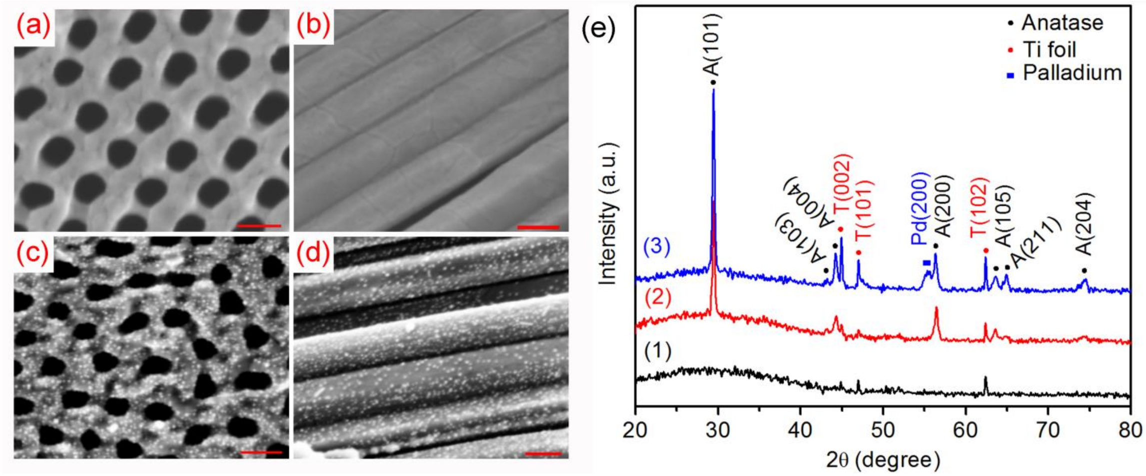

Figure 5-1 Top/side SEM images of (a/b) NT450 and (c/d) PCNT450, the scale bars are 100 nm. (e) XRD spectra of (1) APNT, (2) NT450 and (3) PCNT450.

To evaluate the photoactivity, photoelectrochemical (PEC) measurements were performed using a three-electrode assembly in 1 M KOH electrolyte. **Figure 5-2a** illustrates the linear sweep voltammetry (LSV) results of the two samples. Both specimens show the steady photocurrent densities at a potential range of -0.4 ~ 0.4 V

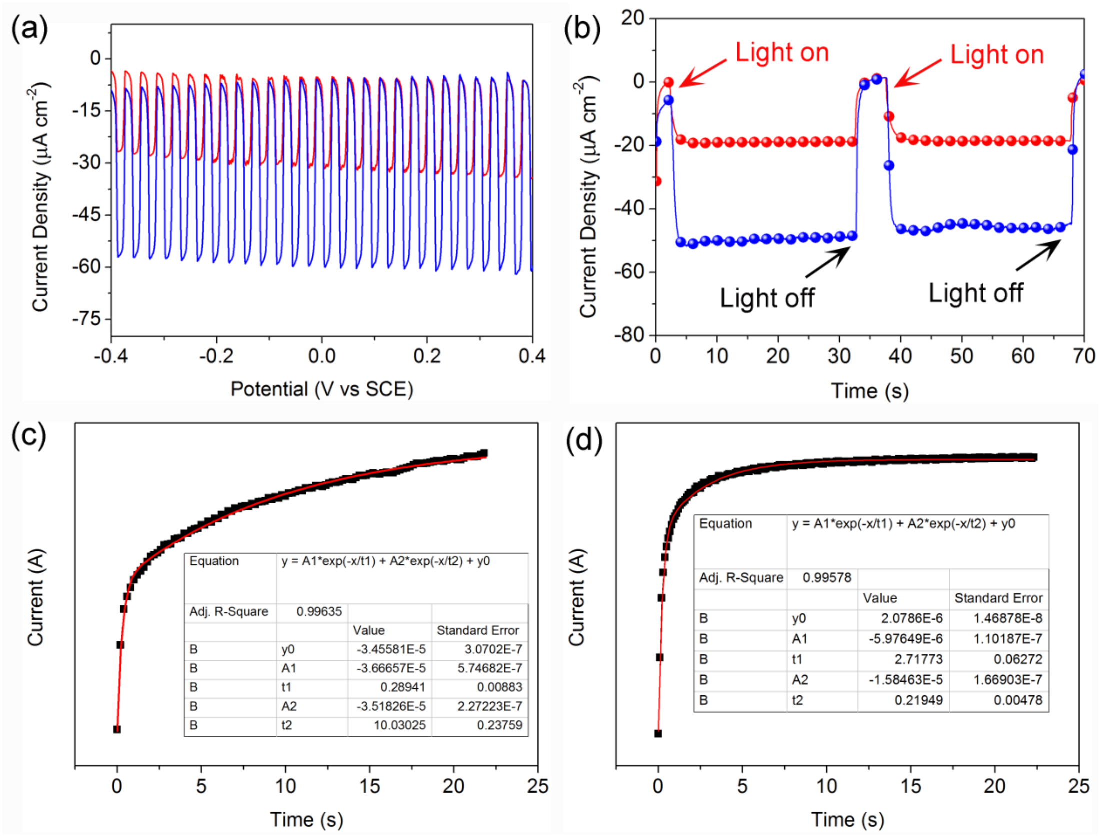

Equation	y = A1*exp(-x/t1) + A2*exp(-x/t2) + y0		
Adj. R-Square	0.99635		
		Value	Standard Error
B	y0	-3.45581E-5	3.0702E-7
B	A1	-3.66657E-5	5.74682E-7
B	t1	0.28941	0.00883
B	A2	-3.51826E-5	2.27223E-7
B	t2	10.03025	0.23759

Equation	y = A1*exp(-x/t1) + A2*exp(-x/t2) + y0		
Adj. R-Square	0.99578		
		Value	Standard Error
B	y0	2.0786E-6	1.46878E-8
B	A1	-5.97649E-6	1.10187E-7
B	t1	2.71773	0.06272
B	A2	-1.58463E-5	1.66903E-7
B	t2	0.21949	0.00478

Figure 5-2 (a) LSV measured at a scan rate of 5 mV s^{-1} under AM1.5 irradiation for NT450 (red) and PCNT450 (blue). (b) Chronoamperometry measured at 0 V with AM1.5 irradiation for NT450 (red) and PCNT450 (blue). Fitted values of decay constant from PEC measurements for (c) NT450 and (d) PCNT450, by fitting to a bi-exponential function to decay *i-t* profile with two time constants.

relative to SCE standard electrode. Compared with the NT450, PCNT450 demonstrates a significant increase of photocurrent density. It clearly demonstrates that the decorated Pd NP exhibits strong electron storage character owing to its lower Fermi energy level than the conduction band energy of TiO_2, thus the migration of photo-induced electrons from the conduction band of TiO_2 to attached Pd NP would greatly enhance the charge separation, resulting in the elongation of charge carrier lifetime and superior photocurrent density. **Figure 5-2b** shows the associated chronoamperometry (at 0 V versus SCE) results. It is clear that PCNT450 shows a photocurrent density over two times higher than NT450.

To assess the decay time, the fitting of a bi-exponential function to the decay *i*-*t* profile with two time constants was carried out (**Equation 5-1** and **5-2**) [37,38].

$$y(t) = A_1 e^{-t/t1} + A_2 e^{-t/t2} + A_0 \qquad (5\text{-}1)$$

$$t_m = t_1 \bullet t_2/(t_1 + t_2) \qquad (5\text{-}2)$$

where y is the time dependent photocurrent; A_1 and A_2 are fitting constants; t is the time; t_1 and t_2 are exponential lifetime components; t_m is the harmonic life time and determined to be 281 and 203 ps for NT450 and PCNT450 with fitted curves shown in **Figure 6-2c** and **2d**, respectively. The decrease of decay time in PCNT450 evidently indicates that the decoration of Pd NPs could remove the surface trap states of TiO_2, hence hindering the photo-excited electron–hole recombination [37,38].

5.3.2 Synchrotron X-ray Absorption Spectroscopy

To reveal the synergy in PCNT450 for enhanced photoactivity, various synchrotron X-ray spectroscopies were applied to disclose the fundamentals. The effect of Pd decoration on the electronic structure of TiO_2 NT substrate is firstly examined by the analysis of Ti $L_{3,2}$-edge and O K-edge as shown in **Figure 5-3**, in which the XANES spectra of commercial anatase and rutile (*Sigma-Aldrich*) are used as standards for comparison. Fine structures at the Ti $L_{3,2}$-edge arise from transitions from $2p_{3/2}$ and $2p_{1/2}$ to unoccupied $3d_{5/2}$ and $3d_{3/2}$ states of Ti site according to the dipole selection rule ($\Delta l = \pm 1$, $\Delta j = 0, \pm 1$). From **Figure 5-3a**, several resonances are presented in the TEY spectra of all samples: two weak pre-edge peaks (p_1 and p_2), two Ti L_3 characteristic peaks t_1 and e_1 (further splitting into e_{11} and e_{12}) and two Ti L_2 characteristic peaks t_2 and e_2. The origin of pre-edge feature p_1 and p_2 is multiplet splitting due to core hole–d electron interactions [39,40]. The energy region from 457.5 to 462 eV is the Ti L_3-edge, peaks t_1 and e_1 are transitions to t_{2g} and e_g states, respectively [41]. A further splitting of the second peak of Ti L_3-edge (e_1) into e_{11} and e_{12} can be assigned to the local distortion at the Ti site from the octahedron (O_h) structure [42]. The relative intensity of e_{11} and e_{12} can be used to distinguish between the anatase and rutile crystal structure of TiO_2. The higher intensity of e_{11} over e_{12} as shown in **Figure 5-3a** indicates that anatase (D_{2d} symmetry) is the dominant structure in NT450 and PCNT450 [25,42], which is also in good accordance with the XANES profile of standard anatase sample shown in **Figure 5-3a**. The energy region from 462 to 470 eV is the Ti L_2-edge region, and peaks t_2 and e_2 are transitions to t_{2g} and e_g states, respectively [41]. Compared with the e_1 peak splitting at Ti L_3-edge, however, we cannot find e_2 peak splitting in this Ti L_2-edge region, which is partly due to the life-time broadening (core-hole effect) because of Coster-Kronig transitions and partly due to the interference of Ti L_3-edge EXAFS underneath. The non-splitting e_1 feature, together with the shorter energy distance between t_2 and e_2, of APNT is due to its amorphous structure, which is consistent with XRD result and previous studies [25,42].

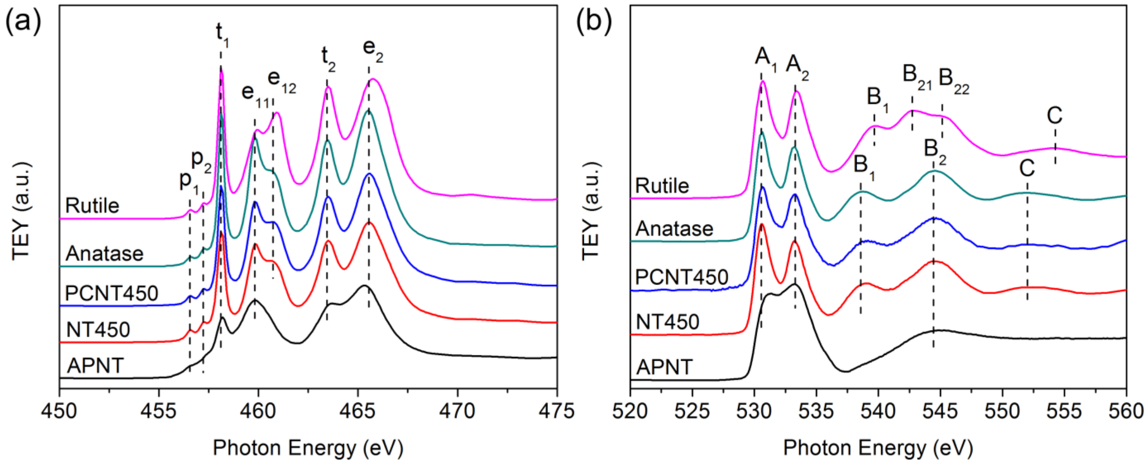

Figure 5-3 (a) Ti $L_{3,2}$-edge and (b) O K-edge XANES spectra of APNT, NT450, PCNT450, commercial anatase and rutile (*Sigma-Aldrich*). All spectra are normalized to the edge jump (flat region of the absorption above the threshold). All except the APNT are shifted vertically for clarity.

Fine structures at the O K-edge can be attributed to dipole transitions from 1s to unoccupied 2p states of O site; different types of features presented in **Figure 5-3b** are due to transitions to the hybridized states between O 2p and Ti 3d or Ti 4sp: The pre-edge within energy region from 529 to 536 eV is transition from O 1s to unoccupied O 2p-Ti 3d hybridized states [42]. And the splitting into two intense peaks A_1 and A_2 is due to the splitting of Ti 3d band and transitions to t_{2g} and e_g states, respectively, which, as a common feature in transitional metal oxides, clearly shows the strong hybridization between O 2p and Ti 3d orbitals. Peaks B_1 and B_2 are transitions from O 1s to O 2p-Ti

4sp hybridized bands while the appearance of higher energy resonance peak C located at ~553eV reflects the long range order in these crystalline samples. It is worth noting that the further peak splitting of B_2 into B_{21} and B_{22} together with energy shifts of peak B_1 and C indicates the totally different local environment of O site in rutile phase (D_{2h} symmetry) compared to anatase phase (D_{2d} symmetry). By comparing the O K-edge XANES of anatase and rutile (**Figure 5-3b**), we can conclude that both NT450 and PCNT450 display anatase structure by sharing the similar O K-edge XANES spectra pattern. The broad pre-edge feature, together with the absence of peak C, of APNT at the O K-edge indicates its amorphous structure [25,42], which is in good accordance with Ti $L_{3,2}$-edge XANES analysis. Therefore, both the XANES spectra from Ti $L_{3,2}$-edge and O K-edge do not show any noticeable difference before and after Pd modification, indicating Pd NPs in this work are only coated on the surface of NTs [6,43]; i.e., Pd is not doped or intercalated into titania lattice.

To provide evidence of Pd NPs coating onto TiO_2 NTs, the study of Pd itself is necessary and the Pd L_3-edge XAFS spectra are shown in **Figure 5-4a**. Pd L_3-edge of Pd foil and $PdCl_2$ (*Sigma-Aldrich*) are shown as standards for comparison. From **Figure 5-4a**, the Pd L_3-edge XAFS spectra of PCNT450 and Pd foil share the similar spectral features. The oscillating patterns (peak f to h) are the EXAFS signature of fcc metallic Pd [44,45], indicating Pd(II) is successfully reduced to Pd(0). After the reaction, a brown color can be observed in the post-reaction solution which can easily make starch solution turn blue. It indicates that I^- is oxidized to I_2 having served as the reducing agent to convert Pd(II) to the Pd nuclei on the surface of TiO_2 NTs and for subsequent Pd NPs growth. This observation is consistent with the result of SEM where Pd NPs are uniformly deposited on the surface of TiO_2 NTs.

In the Pd L_3-edge XANES, the first intense peak, so-called whiteline (WL) appears as a sharp resonance just above the threshold; it arises from $2p_{3/2}$ to 4d states transitions, and the area underneath the WL is proportional to the unoccupied densities of states of the Pd d-band above the Fermi level [44]; i.e., that the larger the area under WL, the higher the unoccupied d-hole count of Pd 4d states, which often correlates to improved catalytic activity. From **Figure 5-4**, several interesting observations are noted: first, a significant

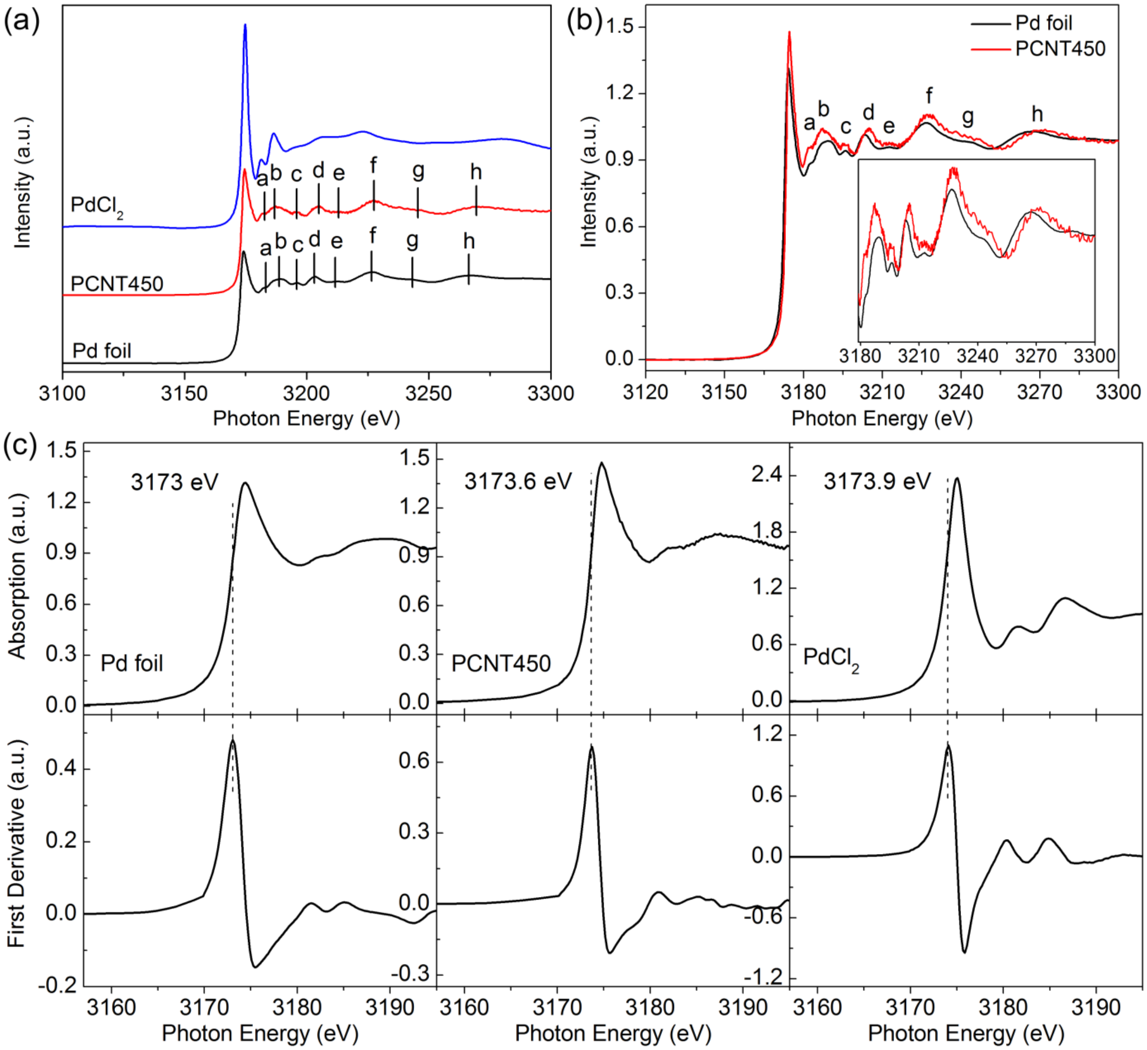

Figure 5-4 (a) Pd L_3-edge XAFS spectra of Pd foil, PCNT450 and $PdCl_2$. (b) A close Pd L_3-edge comparison between Pd foil and PCNT450, the inset is their post-edge comparison. (c) XANES spectra and their first derivatives near Pd L_3-edge whiteline region of Pd foil, PCNT450 and $PdCl_2$ (the vertical dash lines indicate their absorption threshold (E_0)). All XAFS spectra are normalized to the edge jump.

increase in the WL intensity of $PdCl_2$ and a slightly enhanced WL of PCNT450 relative to Pd foil can be seen (**Figure 5-4a** and **5-4b**); second, compared with the absorption threshold (the first maximum of the first derivative of XANES) of Pd foil (E_0 = 3173 eV), the Pd L_3-edge absorption threshold of PCNT450 and $PdCl_2$ shifts by 0.6 eV and 0.9 eV, respectively, to the higher energy region (**Figure 5-4c**); third, upon palladium NPs formation, the Pd L_3-edge of PCNT450 shows a noticeable broadening in all resonance peaks than that of Pd foil (**Figure 5-4b**); last but more interestingly, a closer observation within Pd L_3 post-edge region of PCNT450 shows that while peak b slightly shifts to lower energy, all other features (d ~ h) shift with progressive larger separation to the corresponding peaks in Pd metal (the inset of **Figure 5-4b**).

For $PdCl_2$, together with its high-energy-shifted absorption threshold, the intense WL intensity is mainly due to its expected 4d electron configuration of Pd(II) although covalence will reduce the total d hole to be less than 2 [46]. The enhanced WL and slightly broadened feature of PCNT450 relative to the bulk Pd foil indicate a d-charge depletion in Pd 4d band upon NPs formation, which is consistent with the +0.6 eV shift of its absorption threshold since reduced Pd d-d interaction at the nanoparticle surface due to a reduction in coordination number, and the interaction between Pd and TiO_2 will both contribute to d charge depletion on Pd site. Then a more effective hybridization between d and s, p orbitals of Pd would yield positive threshold shift as 4d charge screens the core hole better than 5s and 5p [45]. The energy-shifted features at the Pd L_3 post-edge can be revealed through the Pd K-edge EXAFS analysis (see below) and the shift of these features (d ~ h) to a higher energy region often indicates a shorter Pd-Pd bond distance (contracted fcc structure) in the NP relative to bulk. According to a d-hole count calculation method [47,48] and the 0.36 d-hole count of palladium metal [44,46], a 0.38 d-hole count is obtained for PCNT450, which is ~ 5.6 % increase compared to the metal foil.

The nature of decorated Pd on TiO_2 NTs is further examined by the Pd K-edge EXAFS study. The similar XAFS oscillation patterns between PCNT450 and Pd foil (**Figure 5-5a**) indicate that they share the same fcc structure. The broadening of the Pd K-edge XANES features (inset of **Figure 5-5a**) of PCNT450 compared to the sharp features observed in bulk Pd foil results from the degradation of long-range order and disorder due to the truncation of the lattice for Pd NPs formation (surface), and to some extent the Pd and TiO_2 NT interface. Note that the oscillation pattern of EXAFS is composed of phase and amplitude, in which the former includes bond length and phase information while the latter provides backscattering amplitude, bond length, and coordination number, etc. Since Fourier transform technique can be used to separate the phase and amplitude, and chemical transferability of phase and amplitude works well between Pd NPs and bulk Pd foil due to their similar systems. Thus the Fourier transform process of the EXAFS oscillations can be used to obtain the bond length difference from the phase analysis and the relative degree of disorder from the amplitude between PCNT450 and Pd foil [49,50]. **Figure 5-5b** shows the Fourier transform of the EXAFS with *k* weighting (*k* range: 2.5-15 Å^{-1} for Pd foil while 2.5-13 Å^{-1} for PCNT450). It is evident that the bond length of the first shell of Pd NPs is smaller than that of bulk Pd foil.

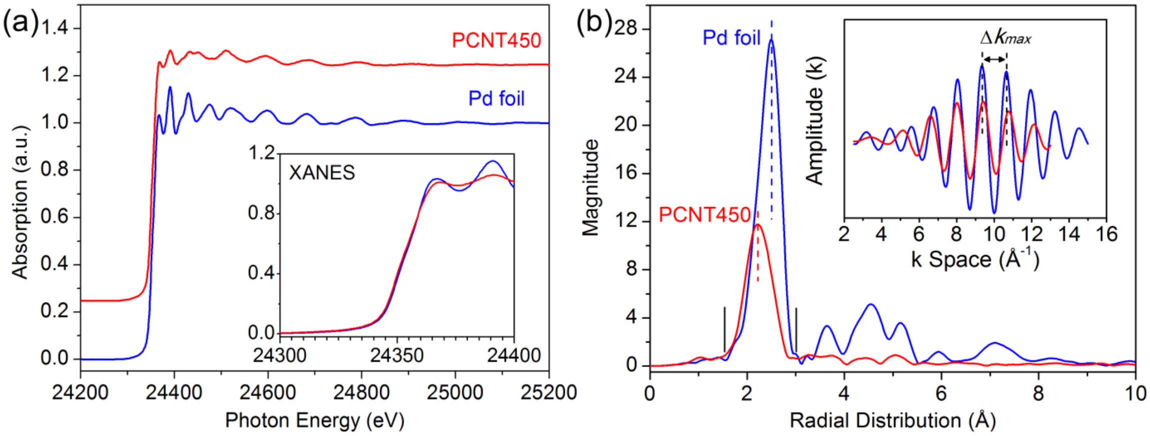

Figure 5-5 (a) Pd K-edge XAFS of PCNT450 and Pd foil (the PCNT450 spectrum is vertically shifted for comparison); the inset is the Pd K-edge XANES. (b) Fourier transform of the EXAFS for PCNT450 and Pd foil. Note that the bond length difference cannot be directly read off since the Pd backscatter phase is not linear in *k* space; the inset shows the Fourier back transform with a filter window at the first shell (*R* range: 1.5-3.0 Å).

Assuming chemical transferability of the phases and amplitude of Pd NPs and bulk Pd foil, a Fourier back-transform of the first shell from the *R* space to *k* space with identical filter window as indicated by two black solid bars (*R* range: 1.5 - 3.0 Å, the inset of **Figure 5-5b**), can be used to obtain the difference of the first shell Pd-Pd interatomic distance. Qualitatively, since $r = (2\pi/\Delta k_{max} - \beta)/2$, where *r* and *k* are the bond length and wave vector, respectively. β is a constant for low *Z* scatterers or in the high *k* region for Pd where the phase of the backscatterer is nearly linear in *k* [50]. So the larger the Δk_{max}, the shorter the bond, which is the case for PCNT450, suggesting the shorter Pd-Pd bond length of Pd NPs than the bulk Pd foil. The reduction in amplitude indicates the disorder structure of Pd NPs due to the truncation of the lattice and the decrease of coordination number at the surface. With an assumption that the phase and the backscattering amplitude of Pd are the same in both Pd NP and Pd metal (a reasonable assumption of chemical transferability), the fitted Δr = 0.14 Å, which was derived from fitting the phase function of Pd NP (extracted from the filtered Fourier back-transform of the first Pd-Pd shell) with that of the Pd metal with a known first shell Pd-Pd distance of 2.75 Å. Intuitively, the fitting result is a little large and it is, probably, due to the partially oxidized shell of Pd NP, resulting in the increase of electron density on the surface and shrinkage of the Pd NP. Because electron transfer from the central Pd atoms to the surface Pd atoms will strength the hybridization between two Pd atoms, thus decreasing the bond distance of Pd-Pd.

Hence, it is no doubt that the obtained Pd NPs coating on TiO_2 NTs show the typical fcc but contracted crystal structure, where the consequent increase of Pd 4d hole count upon NPs formation should be responsible for the enhanced photoactivity of PCNT450 (**Figure 5-2**).

5.3.3 XEOL and RIXS Analysis

The synergistic effect of palladium coating on the TiO_2 host can be revealed with XEOL analysis. As shown in **Figure 5-6a**, NT450, like commercial anatase sample, exhibits one broad luminescence band centered at ~500 nm whereas the wavelength of green emission band shifts to ~550 nm in PCNT450 with a comparatively sharp reduction in its intensity.

In order to unfold the origin and distinguish the differences of these two broad green emission bands before and after Pd modification, a combination of PLY with TEY and PFY XANES at the Ti $L_{3,2}$- and O K-edges is used in this study as shown in **Figure 5-6b** ~ **6e**. Note that TEY and PFY spectra are shown for comparison although all PFY spectra show a broadening feature due to self-absorption [25]. PLY spectra are presented to demonstrate the variation of luminescence intensities as the excitation energy is continuously scanned across both the Ti $L_{3,2}$- and O K-edges. As shown in **Figure 5-6**, the PLY spectra at the Ti $L_{3,2}$- and O K-edges of PCNT450 follow the trace of TEY and

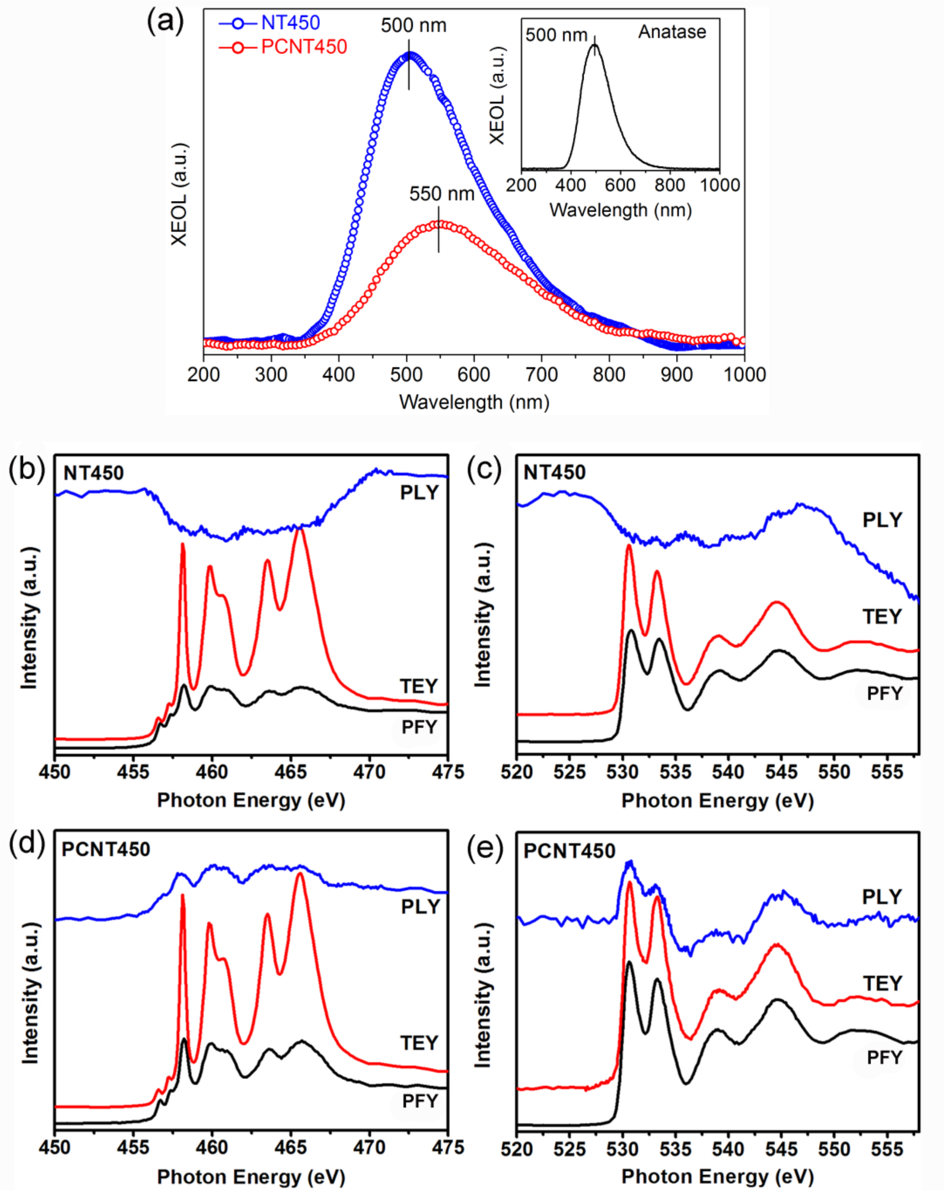

Figure 5-6 (a) XEOL spectra of NT450 and PCNT450 collected with excitation photon energy at 575 eV normalized to incident flux (well above O K-edge, the inset is the XEOL spectrum of commercial anatase collected at 575 eV). Stacks of PLY spectra with TEY and PFY spectra across the (b) Ti $L_{3,2}$-edge and (c) O K-edge of NT450, and (d) Ti $L_{3,2}$-edge and (e) O K-edge of PCNT450. All spectra are normalized to the incident photon flux.

PFY spectra whereas the PLY spectra of NT450 behave in a totally different way: PLY at the Ti $L_{3,2}$-edge displays totally inversed feature and a partially inversed PLY is collected at the O K-edge, meantime, both of them (PLY at the Ti L- and O K-edges) do not show much fine structure compare to their associated TEY and PFY XANES profiles.

The inversion of PLY can be due to multiple reasons: (1) the element with an inverse PLY spectrum at the edge of interest does not contribute or contributes less effectively to the optical luminescence because the excited photoelectron tends to decay in a non-radiative way (e.g., phonons); (2) sample is too thick and suffers the saturation effect [25]. Because once the photon energy reaches the edge of interest in the material, the attenuation length of X-ray will decrease sharply due to the increase of absorption cross-section. For example, the attenuation length of X-ray is ~900 nm below and ~100 nm above the Ti $L_{3,2}$-edge [25], then some of the Auger electrons as well as other secondary electrons and fluorescence X-rays will escape from the sample surface without fully contributing to optical luminescence via thermalization. Since the optical photons are mainly from the energy transfer of the above secondary process to optical channel, hence, an inefficient energy transfer would result in a decrease of XEOL intensity. As the NT specimen in this study has a thickness in microns (not shown) and a partially inversed PLY at the O site is observed (**Figure 5-6c**), so the inversion of PLY is more likely caused by saturation effect. Moreover, PLY spectra at the Ti $L_{3,2}$- and O K-edges of PCNT450 follow the trace of TEY and PFY XANES profiles. It indicates that this green emission is very sensitive to the sample surface. It should be mentioned that Pd absorbs strongly in the 400 -600 eV region; thus below the Ti L- or the O K-edge, Pd absorbs and its contribution to luminescence is negligible, so below the edge, the luminescence is weaker than when Pd is absent, leading to a positive (right side up) PLY.

Therefore, it is undoubted that two emission bands (~500 nm in NT450 and ~550 nm in PCNT450) originate from the similar site: surface defects of anatase (e.g., oxygen vacancies), which is consistent with a previous XANES and XEOL study of pure NTs [25] and photoluminescence (PL) studies of Pd modified TiO_2 [51-53]. The red shift of PCNT450 XEOL spectrum, compared with the XEOL spectra of NT450 and commercial anatase, is almost certainly due to the surface modification of TiO_2 NTs upon Pd coating. The sharp decrease of XEOL intensity of PCNT450 indicates the reduction of surface defects of anatase by either healing upon Pd NPs coating [43] or suppressing with the preferred deposition of Pd NPs on such surface sites. And the absorption of incident photon by Pd does not contribute directly to energy transfer to the optical channel. Henceforth, on one hand, the photo-generated electrons at the TiO_2 conduction band in PCNT450 can recombine with valence holes via surface defects which is similar to the recombination process of pure NTs (NT450); on the other hand, they can be captured by Pd site at the interface between Pd and TiO_2 since the equalized Femi energy level of PCNT450 (once Pd and TiO_2 are in contact, their Fermi level will equalize and a subsequent Schottky barrier layer will be formed at their interface) is lower than the conduction band energy level of TiO_2. Thus electrons on the conduction band of TiO_2 prefer to transferring to the Pd site, corroborating that Pd can act as the electron sink on the surface of TiO_2 and hence effectively slowing down the recombination rate of radiative recombination of electrons and holes.

In addition, resonant inelastic X-ray scattering (RIXS) spectroscopy (or RXES: resonant X-ray emission spectroscopy) is also used to pinpoint the effect of Pd modification on the Ti 3d states of anatase TiO_2 NTs as shown in **Figure 5-7**. The energy loss scale is obtained via subtracting the measured emission energy from the excitation energy (indicated in **Figure 5-7a**). Earlier Ti 2p RIXS studies of TiO_2 have been well-established via experimental [36,54,55] and theoretical [56] analysis. It is well documented that three components are included in Ti 2p RIXS (shown in **Figure 5-7b**) [36,57]: normal Ti 3d→Ti 2p emissions at fixed photon emission energy (the energy loss scale of these peaks vary as the excitation energy increases and are proportional to the change of the excitation energy) are indicated by the short solid bars; elastic scattering features (which have emission energies equal to the excitation energies) are located at the 0 eV on the energy loss scale; and inelastic scattering features such as charge-transfer features, which are shown as constant energy loss peaks (c_1, c_2 and c_3), are located between elastic scattering features and normal Ti 3d→Ti 2p emission peaks. The origin of the weak energy loss features located between 0 eV and 5 eV below the excitation energy is quite interesting and can be assigned to d-d transitions as inelastic scattering features (shake-up) [36,57]. In **Figure 5-7b**, these d-d transition features are clearly presented in NT450 especially when the excitation energy reaches the t_{2g}-resonance (spectrum a and c) and e_g-resonance (spectrum e and f), which, to the best of our knowledge, have not been

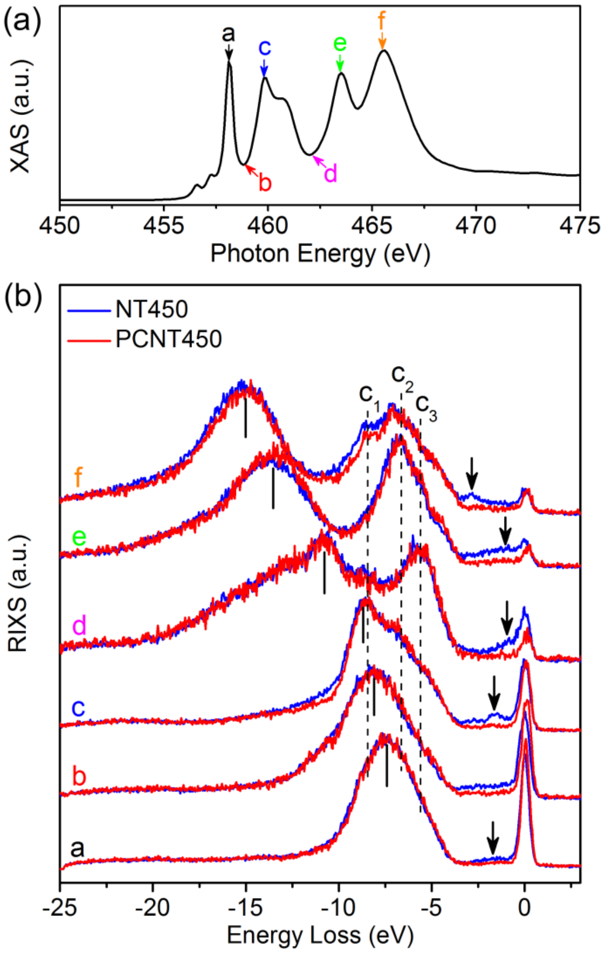

Figure 5-7 (a) Ti 2p XANES. (b) Ti 2p RIXS spectra of NT450 and PCNT450 excited at the photon energies indicated in the XANES spectrum and each pair RIXS spectra of NT450 and PCNT450 are normalized to their corresponding Ti 3d→Ti 2p emission (indicated by solid bars), respectively. The elastic peak is at 0 eV energy loss.

reported before in Ti 2p RIXS spectra of both pure anatase and rutile TiO_2 nanomaterials. And all these energy loss features are totally quenched upon palladium modification. Previous Ti 2p RIXS study of lithium doped nanoporous anatase TiO_2 [36] and $La_xSr_{1-x}TiO_3$ [57] indicate that the presence of d-d transition features is due to the presence of an extra electron localized at the Ti t_{2g} states, i.e., t_{2g} states are partially occupied instead of the Ti 3d(0) configuration of TiO_2. Likewise, we can attribute the origins of these inelastic scattering features to the reduction of Ti(IV) to Ti(III) (Ti d band is no longer empty) resulting from the defects presented in NT450. More interestingly, the disappearance of these low energy loss features in PCNT450 clearly indicates the coated Pd NPs can effectively heal the defects, especially defects at the interface between Pd and TiO_2, to decrease the recombination probability of photo-excited electron–hole pairs. Thus decoration of Pd NPs onto TiO_2 NTs can efficiently elongate the lifetime of photoactive electron-hole pairs, which is consistent with the XEOL reduction (**Figure 5-6a**) as well as enhanced photoactivity (**Figure 5-2**) of PCNT450.

5.4 Conclusions

Vertically well-aligned TiO_2 NTs are obtained using a two-step electrochemical anodization process, this ideal nanotubular morphology favors the uniform deposition of Pd NPs on the surface of NTs (inner and outer tube-wall). Several findings are highlighted here: (1) Pd NPs are only coated on NTs without the noticeable change of electronic structure of pure NTs via the Ti $L_{3,2}$- and O K-edges examinations; (2) Pd NP is contracted compared to Pd metal by showing extra Pd 4d unoccupied states; (3) The sharp reduction of XEOL intensity of Pd modified NTs compared with pure NTs, together with RIXS analysis, indicates that the coated Pd NPs can partially heal the surface defects of anatase, hence, Pd can remove the photo-excited electrons from the conduction band of TiO_2 to efficiently hamper the radiative recombination process; (4) all the above findings corroborate the enhanced photoactivity of Pd coated TiO_2 NT specimen as demonstrated in this work.

5.5 References

[1] J. F. Yan and F. Zhou, *J. Mater. Chem.* **21**, 9406 (2011).

[2] G. K. Mor, K. Shankar, M. Paulose, O. K. Varghese, and C. A. Grimes, *Nano Lett.* **6**, 215 (2006).

[3] Z. R. R. Tian, J. A. Voigt, J. Liu, B. McKenzie, and H. F. Xu, *J. Am. Chem. Soc.* **125**, 12384 (2003).

[4] J. J. Gong, Y. K. Lai, and C. J. Lin, *Electrochim. Acta* **55**, 4776 (2010).

[5] J. J. Gong, C. J. Lin, M. D. Ye, and Y. K. Lai, *Chem. Commun.* **47**, 2598 (2011).

[6] M. D. Ye, J. J. Gong, Y. K. Lai, C. J. Lin, and Z. Q. Lin, *J. Am. Chem. Soc.* **134**, 15720 (2012).

[7] Z. Y. Li, H. N. Zhang, W. Zheng, W. Wang, H. M. Huang, C. Wang, A. G. MacDiarmid, and Y. Wei, *J. Am. Chem. Soc.* **130**, 5036 (2008).

[8] N. K. Shrestha, J. M. Macak, F. Schmidt-Stein, R. Hahn, C. T. Mierke, B. Fabry, and P. Schmuki, *Angew. Chem. Int. Ed.* **48**, 969 (2009).

[9] Y. Y. Song, F. Schmidt-Stein, S. Bauer, and P. Schmuki, *J. Am. Chem. Soc.* **131**, 4230 (2009).

[10] E. Balaur, J. M. Macak, H. Tsuchiya, and P. Schmuki, *J. Mater. Chem.* **15**, 4488 (2005).

[11] S. Caramori, V. Cristino, R. Argazzi, L. Meda, and C. A. Bignozzi, *Inorg. Chem.* **49**, 3320 (2010).

[12] K. S. Mun, S. D. Alvarez, W. Y. Choi, and M. J. Sailor, *ACS Nano* **4**, 2070 (2010).

[13] J. P. Zou, Q. Zhang, K. Huang, and N. Marzari, *J. Phys. Chem. C* **114**, 10725 (2010).

[14] K. Shin, S. Il Seok, S. H. Im, and J. H. Park, *Chem. Commun.* **46**, 2385 (2010).

[15] J. Hensel, G. M. Wang, Y. Li, and J. Z. Zhang, *Nano Lett.* **10**, 478 (2010).

[16] H. B. Li, X. C. Duan, G. C. Liu, and X. Q. Liu, *J. Mater. Sci.* **43**, 1669 (2008).

[17] X. H. Li, G. Y. Chen, L. B. Yang, Z. Jin, and J. H. Liu, *Adv. Funct. Mater.* **20**, 2815 (2010).

[18] C. H. Lin, C. H. Lee, J. H. Chao, C. Y. Kuo, Y. C. Cheng, W. N. Huang, H. W. Chang, Y. M. Huang, and M. K. Shih, *Catal. Lett.* **98**, 61 (2004).

[19] M. Zhang, Y. Bando, and K. Wada, *J. Mater. Sci. Lett.* **20**, 167 (2001).

[20] S. Kobayashi, N. Hamasaki, M. Suzuki, M. Kimura, H. Shirai, and K. Hanabusa, *J. Am. Chem. Soc.* **124**, 6550 (2002).

[21] Q. Chen, W. Z. Zhou, G. H. Du, and L. M. Peng, *Adv. Mater.* **14**, 1208 (2002).

[22] B. D. Yao, Y. F. Chan, X. Y. Zhang, W. F. Zhang, Z. Y. Yang, and N. Wang, *Appl. Phys. Lett.* **82**, 281 (2003).

[23] J. Zhang, M. J. Li, Z. C. Feng, J. Chen, and C. Li, *J. Phys. Chem. B* **110**, 927 (2006).

[24] T. B. Ghosh, S. Dhabal, and A. K. Datta, *J. Appl. Phys.* **94**, 4577 (2003).

[25] L. J. Liu, J. Chan, and T. K. Sham, *J. Phys. Chem. C* **114**, 21353 (2010).

[26] C. Ratanatawanate, Y. Tao, and K. J. Balkus, *J. Phys. Chem. C* **113**, 10755 (2009).

[27] L. Wang, M. I. Nathan, T. H. Lim, M. A. Khan, and Q. Chen, *Appl. Phys. Lett.* **68**, 1267 (1996).

[28] Z. H. Zhang, Y. J. Yu, and P. Wang, *ACS Appl. Mater. Interfaces* **4**, 990 (2012).

[29] F. Gobal and M. Faraji, *J. Electroanal. Chem.* **691**, 51 (2013).

[30] M. Alexander and K. Pandian, *J. Solid State Electrochem.* **17**, 1117 (2013).

[31] R. Zhao, R. F. Ding, S. J. Yuan, W. Jiang, and B. Liang, *Int. J. Hydrogen Energy* **36**, 1066 (2011).

[32] D. Vaccarello, L. J. Liu, J. G. Zhou, T. K. Sham, and Z. F. Ding, *J. Phys. Chem. C* **119**, 11922 (2015).

[33] T. Regier, J. Paulsen, G. Wright, I. Coulthard, K. Tan, T. K. Sham, and R. I. R. Blyth, *AIP Conf. Proc.* **879**, 473 (2007).

[34] Y. F. Hu *et al.*, *AIP Conf. Proc.* **1234**, 343 (2010).

[35] J. W. Li, X. B. Chen, E. Matias, W. J. Zhang, and Asme, *Proc. ASME Int. Mech. Eng. Congr. Expo.* **13**, 91 (2012).

[36] A. Augustsson, A. Henningsson, S. M. Butorin, H. Siegbahn, J. Nordgren, and J. H. Guo, *J. Chem. Phys.* **119**, 3983 (2003).

[37] A. A. Melvin, K. Illath, T. Das, T. Raja, S. Bhattacharyya, and C. S. Gopinath, *Nanoscale* **7**, 13477 (2015).

[38] Y. C. Pu *et al.*, *Nano Lett.* **13**, 3817 (2013).

[39] G. S. Henderson, X. Liu, and M. E. Fleet, *Phys. Chem. Miner.* **29**, 32 (2002).

[40] J. P. Crocombette and F. Jollet, *J. Phys.: Condens. Matter* **6**, 10811 (1994).

[41] T. Li, R. Larciprete, S. Turchini, N. Zema, A. Bonanni, and A. Di Trolio, *J. Phys. Chem. C* **117**, 687 (2013).

[42] J. G. Zhou *et al.*, *J. Mater. Chem.* **19**, 6804 (2009).

[43] Y. G. Chang, J. Xu, Y. Y. Zhang, S. Y. Ma, L. H. Xin, L. N. Zhu, and C. T. Xut, *J. Phys. Chem. C* **113**, 18761 (2009).

[44] T. K. Sham, *Phys. Rev. B* **31**, 1903 (1985).

[45] P. Zhang and T. K. Sham, *Appl. Phys. Lett.* **82**, 1778 (2003).

[46] T. K. Sham, *Phys. Rev. B* **31**, 1888 (1985).

[47] I. Coulthard and T. K. Sham, *Phys. Rev. Lett.* **77**, 4824 (1996).

[48] P. Zhang and T. K. Sham, *Appl. Phys. Lett.* **81**, 736 (2002).

[49] I. Coulthard, D. T. Jiang, J. W. Lorimer, T. K. Sham, and X. H. Feng, *Langmuir* **9**, 3441 (1993).

[50] X. H. Sun, C. Didychuk, T. K. Sham, and N. B. Wong, *Nanotechnology* **17**, 2925 (2006).

[51] Z. B. Wu, Z. Y. Sheng, Y. Liu, H. Q. Wang, N. Tang, and J. Wang, *J. Hazard. Mater.* **164**, 542 (2009).

[52] Y. C. Hsiao and Y. H. Tseng, *Micro Nano Lett.* **5**, 317 (2010).

[53] R. Vinu and G. Madras, *J. Mol. Catal. A: Chem.* **291**, 5 (2008).

[54] Y. Harada, T. Kinugasa, R. Eguchi, M. Matsubara, A. Kotani, M. Watanabe, A. Yagishita, and S. Shin, *Phys. Rev. B* **61**, 12854 (2000).

[55] L. D. Finkelstein *et al.*, *Phys. Rev. B* **60**, 2212 (1999).

[56] M. Matsubara, T. Uozumi, A. Kotani, Y. Harada, and S. Shin, *J. Phys. Soc. Jpn.* **69**, 1558 (2000).

[57] T. Higuchi *et al.*, *Phys. Rev. B* **60**, 7711 (1999).

Chapter 6

6 Tracking the Sodium Uptake/Release Behavior in TiO_2 Nanotubes

6.1 Introduction

Current research in TiO_2 engineering currently has made promising progress toward its energy applications in photocatalysis [1,2], dye-sensitized solar cells [3,4], supercapacitors [5,6], and rechargeable battery systems such as lithium-ion batteries (LIBs) and sodium-ion batteries (SIBs) [7-10]. TiO_2 has been shown to exhibit excellent cyclability and high rate capability as an anode material in LIBs and SIBs, due to its open structure for the fast transport of Li^+ and Na^+ ions [7,8]. Nevertheless, although both alkali metal ions theoretically have comparable activation barrier for insertion/extraction in/out of titania lattice [11], their ionic size difference has resulted in different electrochemical reaction mechanisms. For example, the reaction of Li^+ with anatase TiO_2 exhibits a two-phase transition process, showing reversible plateaus in the potential-capacity curve [7,12,13], whereas the reaction of Na^+ with anatase TiO_2 shows no plateau, indicating its pseudocapacitive (i.e., Na^+ ion is rather adsorbed than stored inside the lattice) nature during cycling [8,14]. A comprehensive understanding of the lithiation process in nanostructured TiO_2 anodes has been worked out in a previous report [7]. Efforts in this work deal with the sodiation mechanism in nanostructured TiO_2 anodes.

As a matter of fact, the Na^+ reaction mechanism with TiO_2 is still not clearly understood. On one hand, the reversible Na^+ insertion/extraction without affecting the integrity of the TiO_2 host structure has been reported [9,15,16]; one the other hand, an irreversible TiO_2 phase transformation to a stable amorphous sodium titanate structure after the first cycle has been claimed; the newly formed phase allows for subsequent reversible Na^+ uptake/release and is responsible for the associated SIB performance [8,17]. Therefore, the further understanding of the Na^+ uptake/release behavior in TiO_2 as well as the associated mechanism in a functional battery is of foremost importance, in order to achieve the desired energy and power densities of SIB using TiO_2 for practical (hybrid) electric vehicles.

Recent development of efficient TiO_2 nanomaterials for SIB mainly concentrates on their phase differences, such as amorphous, anatase, TiO_2-B and rutile [8,9,16-19]. The main objective of this work is to study the interaction between the Na^+ insertion/extraction and the electronic structure of TiO_2 nanotubes (NTs), in the amorphous and anatase structures, using the element and chemical-specific X-ray absorption near edge structure (XANES).

First of all, amorphous and anatase TiO_2 are two popular structures investigated as anode materials in SIB systems [8]. The highly distorted (locally) amorphous structure with rich defects and voids are desirable for the accommodation of Na^+ ions. Also, compared to crystalline structure, the diffusion of Na^+ ions can be enhanced in its amorphous counterpart which provides more percolation pathways due to its increased interfacial regions [16]. Alternatively, anatase TiO_2 also shows its excellent capability for the accommodation of Na^+ ions due to the following advantages: (1) two-dimensional Na^+ diffusion tunnels along the a and b axis (**Figure 6-1**) with a size of 3.725 Å × 3.785 Å suitable for the interstitial accommodation of Na^+ ion (1.02 Å), (2) low insertion potential (~1 V vs. Na^+/Na), (3) high theoretical capacity of ~335 mAh g^{-1}, and (4) pseudocapacitive character upon Na^+ uptake/release [8,17,18,20-22].

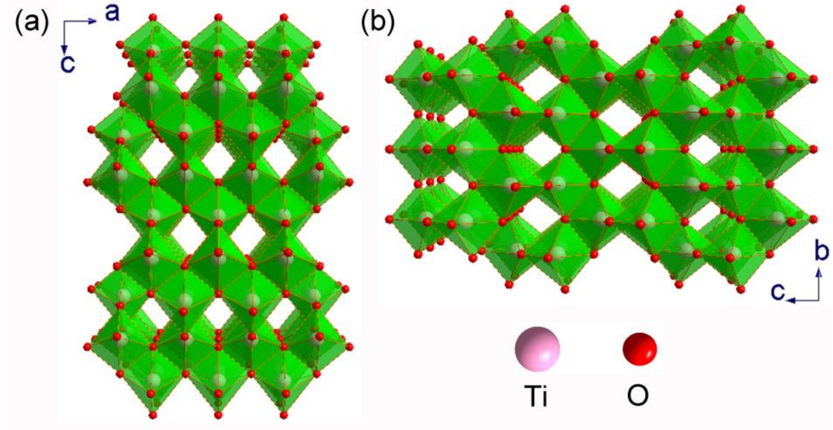

Figure 6-1 Crystal structure of anatase TiO_2 projected along [010] (a) and [100] (b) directions.

Second, anodic TiO_2 NTs attached to Ti metal foil exhibit excellent electrochemical performance. It is because (1) the unidirectional NT tunnels provide large interface for fast ionic/electronic mobility, (2) the self-ordered NTs directly attached to the metallic substrate with good mechanical adhesion and electrical connection to current collector, can greatly reduce the resistance without using binder and carbon additive, and (3) NTs also offer an electrolyte reservoir for the local access of Na^+ ions [18].

XANES is arguably the most suitable technique to investigate the local structure variation of TiO_2 upon sodiation/desodiation. As XANES records the core level excitation of element of interest, thus the effect of Na^+ insertion/extraction on the local structure of TiO_2 can be tracked from multiple perspectives; i.e., Ti, O and Na. Besides, XANES is a local probe, it has the unique advantage for studying amorphous structures. Therefore, in this chapter, an insight for the Na^+ reaction mechanism with TiO_2 NTs is provided, of which the Na^+ uptake/release behavior in amorphous and anatase structures is comparatively examined at the Ti K-edge, Ti $L_{3,2}$-edge, O K-edge and Na K-edge.

6.2 Experimental Section

6.2.1 Preparation of Amorphous and Anatase TiO_2 NTs

Vertically aligned TiO_2 NTs were prepared by an electrochemical anodization method. In a standard two-electrode electrochemical cell, Ti foil (0.1 mm thick, Goodfellow) with a size of 1 cm × 0.5 cm was the anode while a Pt wire was used as cathode. The electrolyte composition included 0.3 wt. % NH_4F (ACS, 98.0 % min, Alfa Aesar), 2 vol. % H_2O and ethylene glycol. To obtain ordered NTs with good geometry and alignment, a two-step anodization procedure was applied. In the first step, Ti foil was anodized at 50 V for 4 h, then the first TiO_2 layer was removed by ultrasonication in 1M HCl. Next, the refreshed Ti foil was rinsed with water and then ethanol several times and dried with N_2 gas. In the second step, to ensure the conductivity of Ti substrate for the following battery test, one side of Ti foil was covered by nail polish to prevent Ti from oxidization. For the second anodization, the same procedure as in the first step was employed, and the one-side of refreshed Ti foil was anodized at 50 V for 40 min. Later on, the as-grown NTs attached to the Ti substrate were rinsed with ethanol several times to remove the excess electrolyte and dried with N_2 gas, and the nail polish on the back side was carefully removed by ethanol infiltrated kimwipes. To initiate the anatase crystallization, the as-grown amorphous NTs were annealed at 450 ℃ for 2 h to obtain anatase TiO_2 NTs [23].

6.2.2 Electrochemical Characterization of Amorphous and Anatase TiO_2 NTs

The electrochemical performance of amorphous and anatase TiO_2 NTs on Ti substrates (5 mm × 5mm) was evaluated in coin-type half cells. The coin-type half cells were assembled in an argon-filled glove box ($[O_2] < 1$ppm, $[H_2O] < 1$ppm), using polypropylene separator (Celgard 3501) and Na metal as the counter electrode. The electrolyte was 1M $NaClO_4$ in ethylene carbonate (EC) and propylene carbonate (PC) in a volume ratio of 1:1. Charge-discharge cycling at a constant current mode was carried out on the Arbin BT-2000 Battery Test System. The electrochemical performance was measured in a voltage range of 0.01 – 2.0 V at room temperature. The specific areal capacity (μAh cm^{-2}) was used to compare the performance of amorphous and anatase TiO_2 NTs, because it is unable to measure the accurate amount of TiO_2 NTs on the Ti substrates. TiO_2 NTs charged or discharged at certain potentials were harvested by disassembling the coin-type half cells in the glove box, and washed with the PC solvent. Then the TiO_2 NTs samples were sealed with kapton tapes and put into an argon-filled container to prevent exposure to the air during transportation.

6.2.3 Morphology and Structure Characterizations

Scanning electron microscopy (SEM) images and energy dispersive X-ray (EDX) mapping were recorded by a LEO (Zeiss) 1540 XB SEM facility operating at 10 kV. XANES measurements were performed at the Canadian Light Source (CLS, Saskatoon, SK, Canada). The Ti K-edge was recorded at the Soft X-ray Microcharacterization Beamline (SXRMB) using Si(111) monochromator crystals [24], whereas the Ti $L_{3,2}$-edge, O K-edge and Na K-edge were tracked at the Spherical Grating Monochromator (SGM) beamline [25]. Note that both beamlines have an energy resolution $E/\Delta E > 5000$, and all the XANES experiments were measured using both total electron yield (TEY) and partial fluorescence yield (PFY). Typically, TEY and PFY provide consistent results for homogeneous samples although they have different probing depths. While TEY (surface-sensitive) tracks the out-going secondary electrons by measuring the specimen current, PFY (bulk-sensitive) collects the out-going characteristic X-ray fluorescence of the element of interest using four silicon drift detectors [23,26]. All spectra were normalized to the incident photon flux.

6.3 Results and Discussion

6.3.1 Electrochemical Performance and Morphology Characterization

The electrochemical performances of TiO_2 NT specimens are examined as shown in **Figure 6-2**. Apparently, both amorphous and anatase TiO_2 NTs exhibit excellent cyclibility and high rate capability upon Na^+ uptake/release. Nevertheless, the amorphous NT delivers a higher areal capacity than the anatase one, which can be mainly attributed to the defect-rich and disordered nature of amorphous TiO_2 NTs, allowing easier accommodation of sodium ions [7,10,27].

In order to track the Na^+ insertion/extraction behavior of both amorphous and crystalline anatase TiO_2 NTs (henceforth denoted “am” and “c”, for amorphous and crystalline anatase, respectively), five different discharge/charge potentials were selected during the first cycle. As shown in **Figure 6-3a**, five states with different discharge/charge potentials are highlighted on the first-cycle discharge/charge curves of amorphous NTs. To track the morphology evolution of NTs during the sodiation/desodiation process, the top and side SEM images of am-1, am-3 and am-5 are shown in **Figure 6-3b**, **3c** and **3d**, respectively. By the same analysis, the first-cycle discharge/charge curves of anatase NTs with five highlighted points are illustrated in **Figure 6-3e**, and the related top and side SEM views of c-1, c-3 and c-5 are displayed in **Figure 6-3f**, **3g** and **3h**, respectively. Apparently, neither amorphous nor anatase TiO_2 shows obvious potential plateaus during the Na^+ uptake/release process, which is in line with previous reports [8,16,18]. Both amorphous and anatase porous NT layers (with an inner NT diameter of ~70 nm and a NT wall thickness of ~30 nm) undergo a negligible morphology change upon Na^+ insertion/extraction. It suggests that the stress and strain in TiO_2 induced by Na^+ ion intercalation can be readily accommodated by the nanotubular structure due to its large

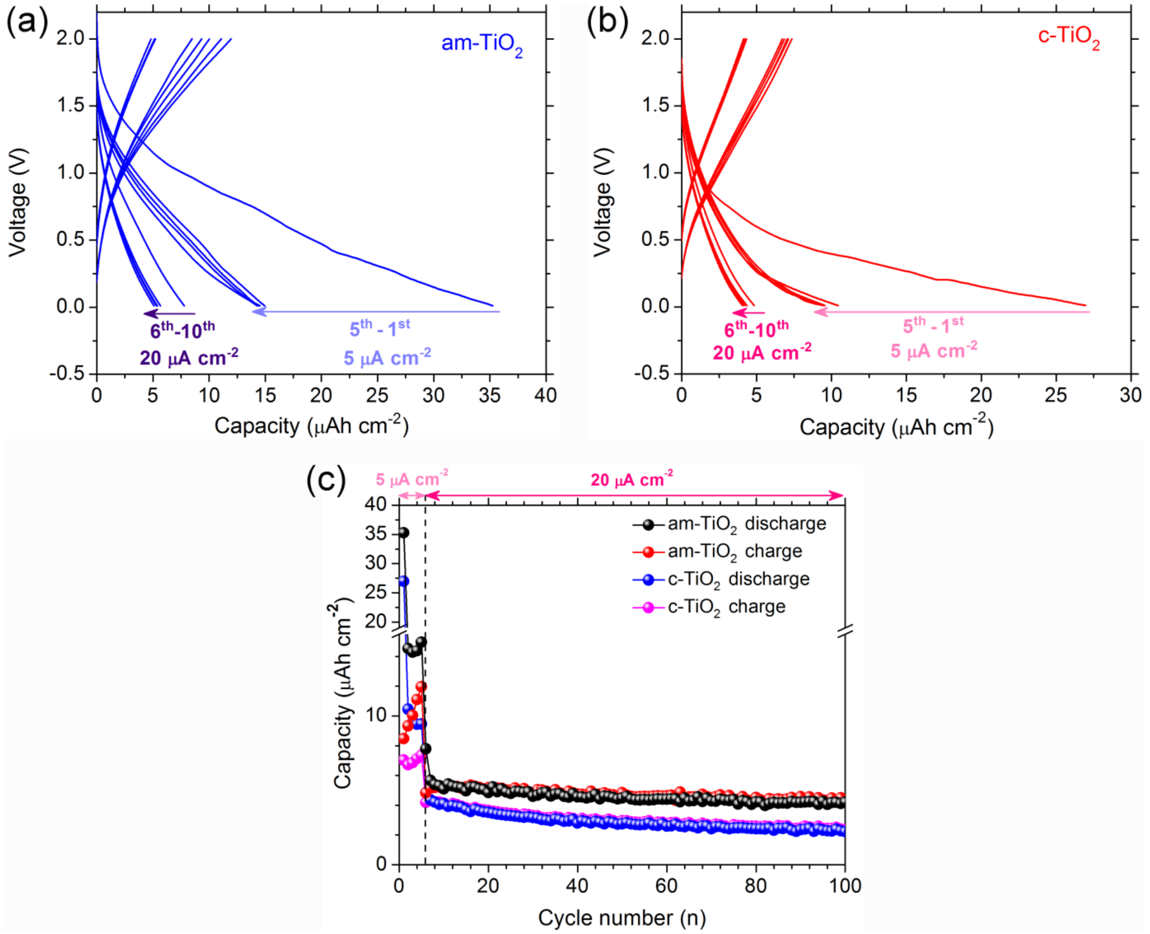

Figure 6-2 Continuous discharge and charge curves at the first ten cycles of (a) amorphous and (b) anatase TiO_2 NTs measured at 5 µA cm^{-2} for the first five cycles and at 20 µA cm^{-2} for the following five cycles. (c) Resulting cycling data of amorphous and anatase TiO_2 NTs measured at 5 µA cm^{-2} for the first five cycles and at 20 µA cm^{-2} for the rest 95 cycles. The unstable capacities shown at the first five cycles are mainly due to the electrolyte decomposition at low current density.

surface to volume ratio as well as the presence of voids [7]. Nonetheless, flower-like structures appear on the top surface of NTs once discharged to 0.01 V (**Figure 6-3c** and **3g**), and they are gone when NTs are again fully charged (**Figure 6-3d** and **3h**), which aligns with a previous report and the reappearance of these structures is not observed for the subsequent cycling [8]. Keep in mind that in the following discussions, state 3 is the turning point where switching from sodiation to desodiation occurs.

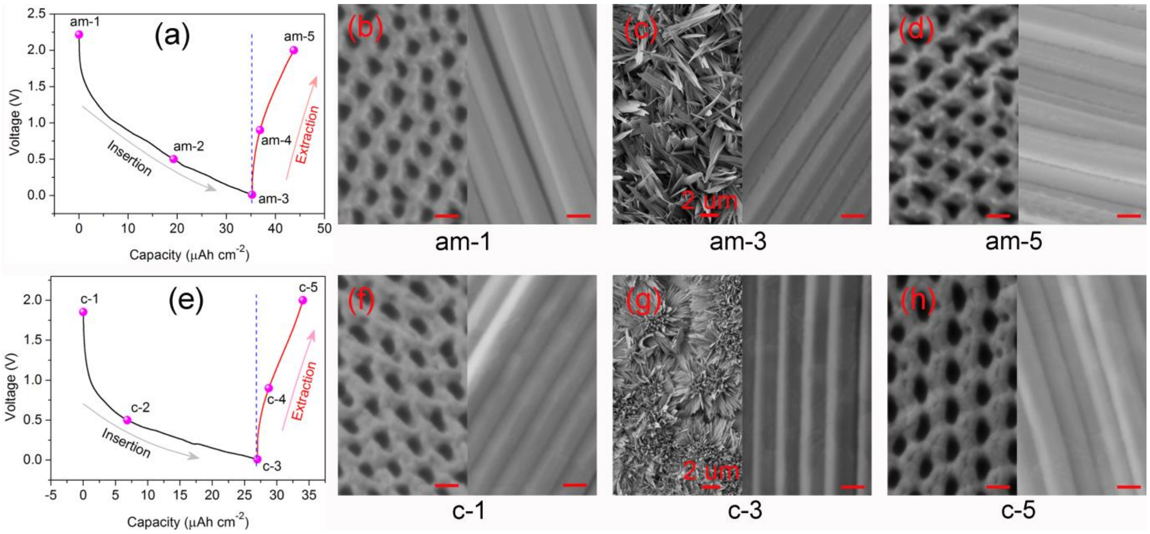

Figure 6-3 (a) the first-cycle discharge/charge curves of amorphous NTs with potential plotted as a function of areal capacity (μAh cm^{-2}), five discharge/charge potentials are labeled where the XANES and SEM characterizations are carried out; (b ~ d) top/side SEM views of am-1, am-3 and am-5 as indicated in (a), respectively; (e) the first-cycle discharge/charge curves of anatase NTs with potential plotted as a function of capacity; (f ~ h) top/side SEM views of c-1, c-3 and c-5 as indicated in (e), respectively. The unlabeled scale bars of SEM images are 100 nm.

To determine the chemical components involved in those flower-like structures. Energy dispersive X-ray (EDX) mapping of amorphous NTs (am-2) is taken at a region with a lesser densification of those structures. As shown in **Figure 6-4**, Na, C, O, Ti and F elements are found in this area. The top flower-like structures are mainly composed of Na, C and O, whereas sodium fluoride particles are also scattered on the top of NTs. EDX mapping of anatase NTs provides the similar findings (not shown). The structural analysis of these flower-like structures will be addressed later.

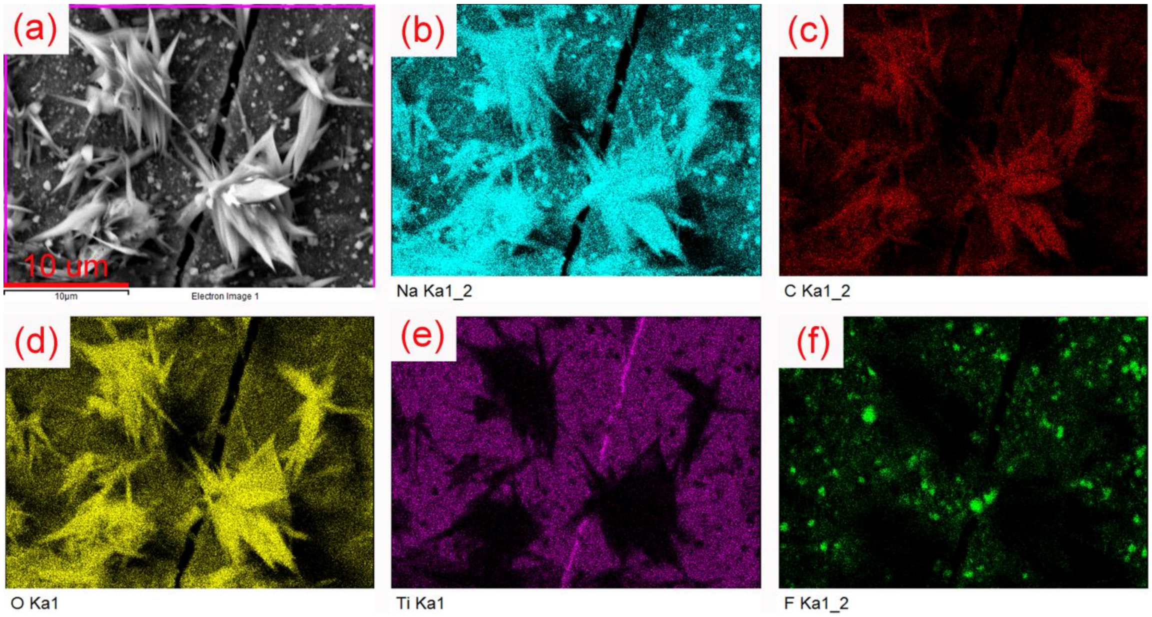

Figure 6-4 EDX mapping of am-2. (a) SEM image of the region of interest. (b ~ f). The elemental mappings for Na (cyan), C (red), O (yellow), Ti (purple), and F (green), respectively.

6.3.2 Ti K-edge Analysis

To track the local structure variations upon Na^+ uptake/release, we first performed XANES analysis at the Ti K-edge. **Figure 6-5** shows the Ti K-edge TEY XANES spectra of both amorphous and anatase NTs collected at their corresponding five different discharge/charge states of the first cycle (indicated in **Figure 6-3a** and **3e**). Meantime, the Ti K-edge spectra of Ti foil, Ti_2O_3, anatase and rutile TiO_2 standards are also included for comparison. Generally, the interpretation of the Ti K-edge is intricate, of which the main features above the edge (above 4980 eV) can be assigned to dipole transition from Ti 1s to 4p states, whereas the pre-edge features (before 4980 eV) are ascribed to electronic transitions to crystal field split hybridized states between Ti 4p and 3d orbitals based on a mixture of quadrupole and dipole excitations [7,28-31]. The pre-edge features can be used as fingerprints for tracking the local structure modification of Ti atoms. As shown in **Figure 6-5a**, both anatase and rutile standards exhibit similar pre-edge features. Whereas peak p_2 can be attributed to the quadrupole transition from Ti 1s to t_{2g} states of Ti absorber, feature p_4 originates from dipole transitions from Ti 1s to states of p character covalently hybridized with both t_{2g} states of Ti neighbor and e_g states of Ti absorber, resonance p_5 can be assigned to dipole transition from Ti 1s to p states covalently hybridized with the e_g states of Ti neighbor [7,28,32-34]. As an extra electron is introduced in TiO_2, its occupancy in Ti 3d orbital interferes with the O ligands, resulting in Jahn-Teller distortion and exchange interaction which yield the broad pre-edge feature, red shift of the edge onset, and the lower intensity of main-edge features at the Ti K-edge of Ti_2O_3. In the case of Ti foil, although the origins of its pre-edge features p_1 and p_3 at the Ti K-edge are still not clearly understood, they must arise from somewhat localized states of d character just above the Fermi level. The highly intensified pre-edge resonances together with the red shift of its main-edge peak compared to TiO_2 and Ti_2O_3, certainly corroborating its metallic Ti^0 character [7,16].

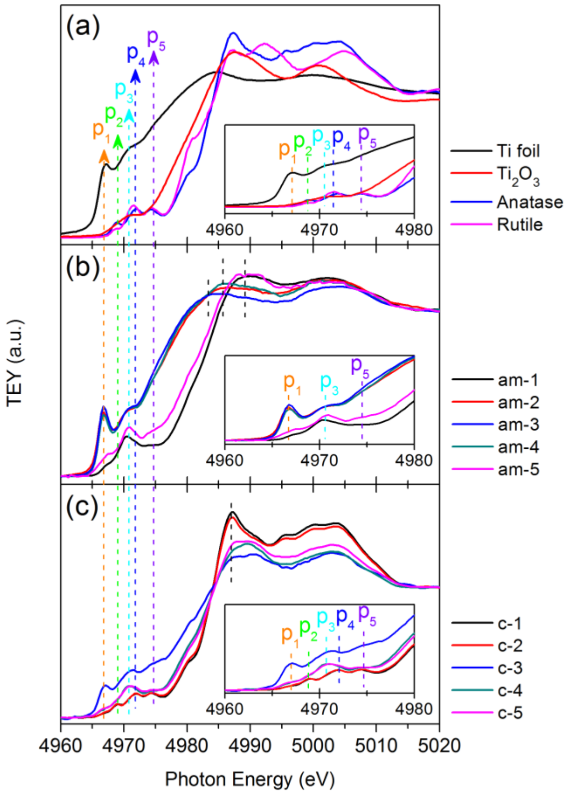

Figure 6-5 Ti K-edge XANES spectra of (a) standards including Ti foil, Ti_2O_3, anatase and rutile TiO_2, (b) amorphous and (c) anatase NTs with five different discharge/charge states at the first cycle. The insets show the magnified views of the corresponding pre-edge regions.

Figure 6-5b shows the evolution of the Ti K-edge XANES spectra of amorphous NTs at five different states. am-1 exhibits an intense peak p_3 as well as two shoulder features p_1 and p_5 at its Ti K pre-edge region, which indicates the distorted or defective Ti local environment with tetrahedral or pentahedral coordination in the amorphous structure [7,35,36]. After discharging to 0.5 V, the Ti K-edge spectrum of am-2 undergoes a dramatic change by showing an unmistakable metallic Ti-like spectral feature with intense peaks p_1 and p_3 together with the red shift of its main-edge feature. The formation of metallic Ti is further confirmed by the Ti K-edge spectrum of am-3. Once amorphous NTs are discharged to 0.01 V, the retention of strong features p_1 and p_3 as well as the further red shift of the main-edge feature of am-3 compared to am-2, evidently suggests that the introduction of Na^+ ion into titania matrix does not just induce the reduction of Ti^{4+} into Ti^{3+} for charge balancing as suggested earlier [16], but it is capable of reducing TiO_2 into metallic Ti after the electrochemical reaction. Consistent results are also reported by Wu et al [8]. By charging back to 0.9 V, despite the characteristics of metallic Ti at the pre-edge region retain, am-4 endures a partial oxidization along with the extraction of Na^+ ions as its main-edge feature at the Ti K-edge exhibits a blue shift compared to am-3 (fully discharge). Once the amorphous NTs are fully charged to 2 V, the general Ti K-edge spectrum pattern of am-5 resembles that of am-1 although it shows the more intense pre-edge features and a slightly negative shift of its edge onset. It indicates that the amorphous TiO_2 NT is a suitable host structure for the Na^+ uptake/release. Note that the formation of metallic Ti during sodiation/desodiation is quite interesting, in agreement of Wu et al. [8] but in contrast to many others [9,16,21,27,37,38].

Figure 6-5c demonstrates the Ti local structure evolution at the Ti K-edge of anatase NTs upon Na^+ intercalation/deintercalation. Both c-1 and c-2 share the same anatase TiO_2 XANES profile. It indicates that the electrochemical reaction at the discharging potential range of 2.2 V ~ 0.5 V, rather than the Na^+ reaction with anatase TiO_2, mainly results in the electrolyte decomposition and/or the formation of solid electrolyte interphase (SEI) [8,14]. As the anatase NTs are discharged to 0.01 V, a sharp change is observed at the Ti K-edge XANES of c-3. At the pre-edge, the general broad and intense features are displayed, where the metallic Ti characteristics (peaks p_1 and p_3) are clearly present, suggesting the reduction of TiO_2 upon its interaction with Na^+ ion as discussed above. Meantime, the decrease of Ti oxidation states in c-3 can be further confirmed by the variation of its main-edge feature, where the peak intensity sharply drops as extra electrons fill the Ti 3d orbitals (hybridized with Ti 4p). Furthermore, the flattening of main-edge features of c-3 compared to the pronounced main-edge fine structures of c-1 and c-2 (crystalline anatase), indicates the degradation of long-range order of anatase TiO_2 NT upon Na^+ insertion. Partial oxidation process takes place as the Na^+ extraction proceeds. Hence, both c-4 and c-5 show a decrease of the intensity of the pre-edge features and an increase of main-edge peaks. Nevertheless, once fully charged to 2 V, neither the pre-edge nor the main-edge of c-5 holds their anatase XANES features. Instead, an amorphous-like Ti K-edge spectrum appears, indicating that an amorphization process occurs in anatase TiO_2 upon Na^+ uptake/release.

6.3.3 Ti L-edge Analysis

XANES measurement at the Ti $L_{3,2}$-edge which tracks the unoccupied densities of state of d character directly, was also performed. **Figure 6-6a** shows the Ti $L_{3,2}$-edge TEY XANES spectra of Ti foil, Ti_2O_3, anatase and rutile TiO_2 standards. The interpretations of fine structures a ~ g are well established [23,26,39,40]: whereas the two resonances a and b at the pre-edge region can be attributed to core-hole–d-electron interactions, feature c and the doublet (d + e) at the Ti L_3-edge result from electronic transitions from the Ti $2p_{3/2}$ to t_{2g} and e_g states, respectively, and electronic transitions from the Ti $2p_{1/2}$ to t_{2g} and e_g states correspond to the respective origins of peak f and g at the Ti L_2-edge. Since the Ti e_g orbitals align toward the O 2p orbitals, the Ti L_3-e_g peak (doublet peaks d and e) possesses high sensitivity of the Ti local environment, i.e., local symmetry and oxidation state [23,41-43]. For anatase and rutile TiO_2 (Ti^{4+}), the dominant peak d over e of the former and the inverse case of the latter, denotes their different local symmetries of D_{2d} and D_{2h}, respectively. As an extra electron fills in the Ti 3d orbital, the Ti L_3-e_g band of Ti_2O_3 (Ti^{3+}) delivers a large peak shape change, where the peak splitting is no longer obvious and only a single peak d is observed. It should be mentioned that the surface of Ti_2O_3 standard suffers a partial oxidization as shown at its TEY XANES, instead, Ti^{3+} signal from its bulk recorded in PFY XANES (**Figure 6-6b**) exhibits a general red shift

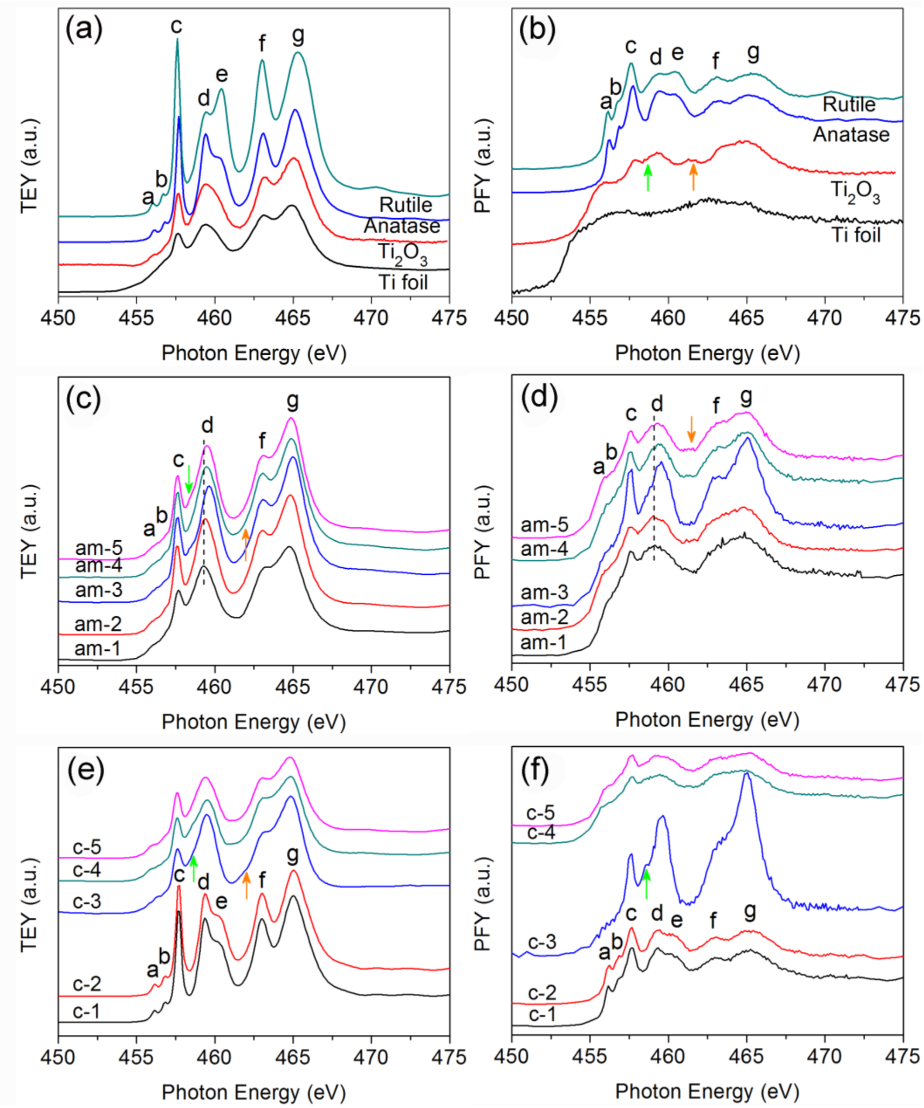

Figure 6-6 Ti $L_{3,2}$-edge XANES spectra of standards including Ti foil, Ti_2O_3, anatase and rutile TiO_2 recorded in (a) TEY and (b) PFY; Ti $L_{3,2}$-edge TEY/PFY XANES spectra of (c/d) amorphous and (e/f) anatase NTs with five different discharge/charge states at the first cycle.

of the Ti $L_{3,2}$-edge spectrum relative to TiO_2, is in good agreement with previous reports [23,44]. As for the Ti foil which is usually covered with an oxide layer, its Ti $L_{3,2}$-edge TEY spectrum, as expected, exhibits a surface XANES pattern close to that of Ti_2O_3, whereas its bulk shows a metallic Ti^0 character with a broad Ti $L_{3,2}$-edge PFY spectrum shifted toward the lower energy region (**Figure 6-6b**).

Figure 6-6c compiles the Ti $L_{3,2}$-edge TEY XANES of amorphous NTs at five different discharge/charge potentials. Since the as-grown NTs has the distorted local symmetry and a rich amount of Ti^{3+}, the Ti $L_{3,2}$-edge spectrum of am-1 shows a general broad pattern without the splitting of peak d [45]. When the amorphous NTs are discharged to 0.5 V, am-2 delivers a different XANES profile compared with am-1, showing a well-resolved spectrum as well as the slightly blue shift of peak d. It suggests that the Ti local structure of amorphous TiO_2 NTs has been changed upon the electrochemical reaction with Na^+ ions within the potential range of 2.2 ~ 0.5 V, which correlates with the above Ti K-edge results (**Figure 6-5b**). Nevertheless, the predominant Ti^0 characteristics detected at the Ti K-edge TEY spectrum of am-2 become negligible at its Ti $L_{3,2}$-edge TEY XANES. This is mainly due to the surface oxidization on the electrode and the much shallower probing depths at the Ti $L_{3,2}$-edge (~ 460 eV) as compared to the Ti K-edge (~ 5000 eV), in line with a previous XPS analysis of sodiated TiO_2 with/without Ar^+ etching [8]. Interestingly, the bulk-sensitive Ti $L_{3,2}$-edge PFY spectrum of am-2 (**Figure 6-6d**) delivers the similar XANES pattern with that of am-1 without showing a reduced Ti signal, indicating that the electrochemical reaction between Na^+ and TiO_2, at this point, only occurs on the surface/subsurface.

With a further decrease of discharging potential to 0.01 V, asymmetries in peaks d and f are observed in the XANES spectrum of am-3 (switching point). Two shoulder features labeled with green and orange arrows pop up at the lower energy regions of peaks d and f, respectively, which clearly represents the formation of new Ti-oxide species with lower Ti oxidation states (e.g., Ti^{3+}) [44]. Meanwhile, peak d shows a blue shift, which presumably results from the distortion of TiO_6 octahedral upon Na^+ intercalation. As the charging process proceeds, the energy position of peak d in both am-4 and am-5 moves back, showing a slight difference compared with the energy position of peak d in am-1. Also, the asymmetric feature is presented in am-5. It demonstrates that part of the inserted Na^+ ions would rather stay in the amorphous TiO_2 host structure despite the charging process is fully completed (i.e., Na^+ trapping). Consistent results are shown in the relevant PFY XANES (**Figure 6-6d**).

Figure 6-6e shows the effect of the Na^+ ion uptake/release process on the Ti local structure in anatase TiO_2 NTs. Within the discharging potential of 1.8 V ~ 0.5 V, no change of anatase XANES profile at the Ti $L_{3,2}$-edge is seen between c-1 and c-2, agreeing with the results revealed at the Ti K-edge (**Figure 6-5c**). As the potential drops to 0.01 V (state 3), the anatase characteristics disappear, instead, c-3 shows a Ti $L_{3,2}$-edge XANES pattern resembling an amorphous structure. Interestingly, it is nearly identical to the Ti $L_{3,2}$-edge XANES of am-3 where the two asymmetric features located at the lower energy locations of peaks d and f, respectively, are also seen. As the Na^+ ion extraction proceeds along with the charging process, both c-4 and c-5 display the very similar amorphous Ti $L_{3,2}$-edge XANES profiles, indicating that the anatase to amorphous transformation upon Na^+ ion insertion is an irreversible phase transition. Further evidence is given by the associated PFY XANES (**Figure 6-6f**) showing that the transition is not limited to the surface of the nanotube.

Therefore, the above findings from the Ti perspectives manifest great significance. At first, by discharging to 0.5 V, the insertion of Na^+ ion occurs in amorphous TiO_2 NT but not significantly in anatase, indicating that the sodiation reaction in the former requires less energy than that in the latter. It can be attributed to the more active nature of amorphous TiO_2 which holds a highly distorted structure and rich defects on its surface for the easier adsorption and reaction of Na^+ ion [45], corroborating the much greater areal capacity achieved in amorphous TiO_2 NTs within the discharging potential range of 2.2 ~ 0.5 V (**Figure 6-3**). Meanwhile, the electrochemical reaction between Na^+ ion and amorphous TiO_2 would firstly reduce the TiO_2 into metallic Ti along with the Na^+ intercalation into titania matrix, forming sodium oxide and metallic Ti [8]. The initial interaction of sodium oxide with TiO_2 yields sodium titanate. Note that the formation of flower-like structures (**Figure 6-4**) is also found during this process. Then by a further discharging to 0.01 V, the Na^+ ion intercalation, together with the formation of metallic Ti and flower-like structures, proceeds further in amorphous NTs but it has been firstly initiated in anatase NTs, suggesting that sodiation of anatase TiO_2 starts at a lower voltage than amorphous TiO_2. It totally explains why Xiong et al. [16] only observed the electrochemical activity of amorphous TiO_2 but not the anatase in their SIB performance study using a cutoff discharge potential of 0.5 V. At this point, the portion of metallic Ti of c-3 revealed by the Ti K-edge analysis is not as significant as that of am-3. It indicates that amorphous TiO_2 can uptake more Na^+ ions than anatase TiO_2 at the same potential, which is in agreement with its higher total areal capacity (**Figure 6-3a**) at 0.01 V, and, again not unexpected; it reveals the much more active nature of amorphous TiO_2 than its anatase counterpart regarding their electrochemical reactivity with Na^+ ion. Nevertheless, anatase TiO_2 with its two-dimensional Na^+ diffusion tunnels (**Figure 6-1**) shows its fast Na^+ uptake capability after its initial sodiation at a lower discharge potential, which achieves a greater areal capacity within the potential range of 0.5 ~ 0.01 V than amorphous NTs, as a comparison demonstrated in **Figure 6-3a** and **3e**. Moreover, both amorphous and anatase hosts exhibit the similar structures at the fully discharged state, especially at the Ti $L_{3,2}$-edge XANES, resembling the amorphous sodium titanate [46]. What clearly emerges from this observation is that whatever the initial host structure is (i.e., amorphous or anatase), the electrochemical reaction of TiO_2 with Na^+ ion would proceed albeit with different rates and inevitably result in the amorphous structure. This is particularly evident for crystalline anatase TiO_2 NT, where the large stress and strain induced by the accommodation of large Na^+ ion would distort both the local structure of distorted TiO_6 octahedral and its ordered long-range connectivity. Lastly, it appears noteworthy that this amorphization transition of anatase is irreversible [8], as the NTs, instead of returning to the anatase structure, retain the amorphous structure despite they are fully charged (**Figure 6-5** and **Figure 6-6**).

6.3.4 O K-edge and Na K-edge Analysis

We now return to the flower-like structures (containing Na, C and O as shown in **Figure 6-4**) which appear in the discharge process and disappear in the charge process along with the Na^+ uptake/release as well as the formation/disappearance of metallic Ti during the first cycle, it is highly necessary to provide structural analysis of these structures to further understand the sodiation mechanism of TiO_2 NTs. Moreover, the irreversible amorphization of anatase NT during the electrochemical reaction of Na^+ ion with anatase TiO_2 is discovered from the above Ti XANES analysis; hence, it is essential to scrutinize the electronic structures of the fully charged materials, which allow for the reversible Na^+ uptake/release in the following cycling and are responsible for the superior cyclability and high rate capability (**Figure 6-2**) [8]. Therefore, XANES analysis from the O (**Figure 6-7a** ~ **7c**) and Na (**Figure 6-7d** ~ **7f**) perspectives is carried out.

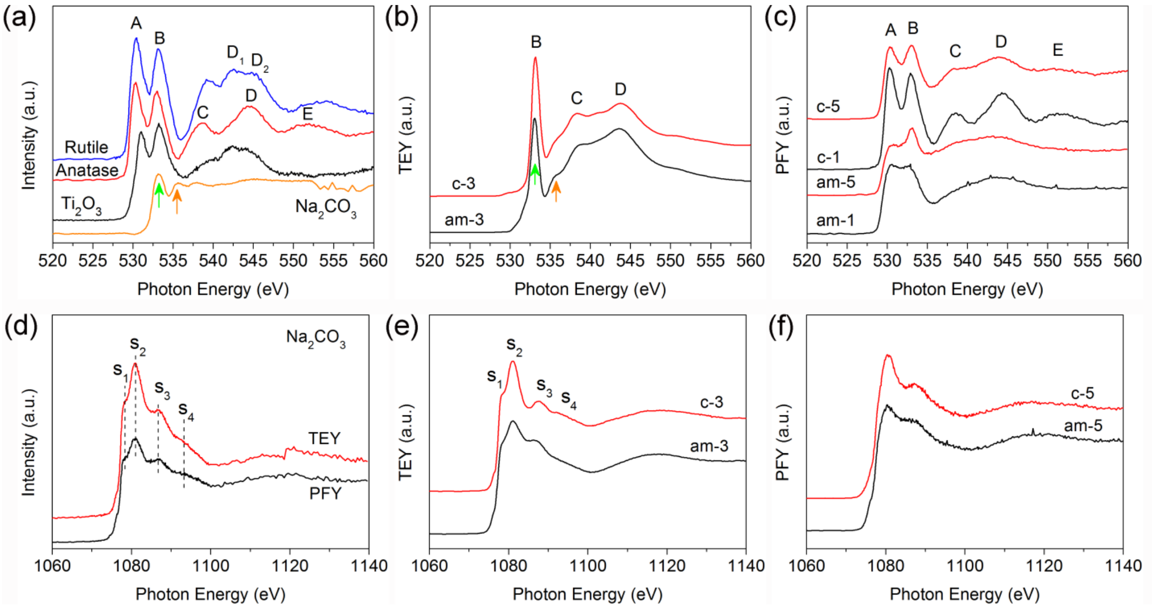

Figure 6-7 O K-edge XANES spectra of (a) standards including Na_2CO_3, Ti_2O_3, anatase and rutile TiO_2, (b) am-3 and c-3 recorded in TEY mode, and (c) am-1, am-5, c-1 and c-5 recorded in PFY mode. Na K-edge XANES of (d) Na_2CO_3 recorded in both TEY and PFY modes, (e) am-3 and c-3 recorded in TEY mode, and (f) am-5 and c-5 recorded in PFY mode.

First, as the flower-like structures cover most of the electrode surface by discharging at 0.01 V (**Figure 6-3b** and **3e**), structural information of the surface of am-3 and c-3 can be obtained using TEY XANES. **Figure 6-7a** shows the O K-edge XANES of standard Na_2CO_3, Ti_2O_3, anatase and rutile TiO_2. In general, except Na_2CO_3, the O K-edge XANES more or less show the typical TiO_2 features A ~ E. Whereas the origins of peaks A and B can be assigned to the electronic transitions from O 1s to 2p covalently hybridized with the t_{2g} and e_g states of Ti 3d, respectively, peaks C and D result from the O 2p hybridized with the Ti 4s and 4p states, and the presence of feature E usually suggests the long-range order of the associated structure [23,26,40,45].

By comparing to these standards, the O K-edge TEY XANES spectra of both am-3 and c-3 (**Figure 6-7b**) exhibit the dominant Na_2CO_3 features (indicated by green and orange arrows) coupled with TiO_2 features (peaks C, D and possibly B), which indicates that these flower-like structures are mainly Na_2CO_3. Further evidence is provided by the Na K-edge XANES. In general, Na K-edge absorption involves the electronic transition from Na 1s to 3p states, which brings the four distinct resonances (s_1 ~ s_4) at the main-edge region of Na_2CO_3 (**Figure 6-7d**) [46]. Consistently, the Na K-edge TEY XANES spectra of both am-3 and c-3 show Na_2CO_3 XANES features, which double confirm the Na_2CO_3 nature of these flower-like structures formed during the electrochemical reaction between Na^+ ion and TiO_2. Nonetheless, results from a recent report point out that flower-like structures hold a sodium oxide form [8], in contrast to our Na_2CO_3 findings revealed by XANES at the O K-edge and Na K-edge (**Figure 6-7b** and **7e**). However, the presence of sodium oxide is not unwarranted; due to its instability, its exposure to ambient CO_2 would result in the formation of Na_2CO_3, which is commonly seen in SIB material study [46]. Thus Na_2CO_3 can be viewed as the product of the initial phase reaction between Na^+ and TiO_2, and it will subside as sodium titanate begins to form.

Second, to investigate the electronic structures of fully charged amorphous and anatase NTs with respect to the electronic structure of their initial stage before discharging, we examine the XANES recorded in PFY at the O K-edge and Na K-edge. Note that PFY rather than TEY XANES mode is applied to minimize contribution from the surface Na_2CO_3 residuals and the SEI. As shown in **Figure 6-7c**, by comparing the O K-edge PFY XANES of am-1 and am-5, we see a generally broad spectrum with the enhanced intensity of peak B in am-5. Similar change also happens to the anatase NTs before discharging (c-1) and after fully charging (c-5) despite the intensity increase of peak B in c-5, which is not as significant as that in am-5.

Several features can be noted from the O data. First, the broadening of O K-edge XANES indicates that the O local structures in both amorphous and anatase NTs are further distorted after the first cycle of Na^+ insertion/extraction [23]. In particular, the anatase host structure suffers degradation of its long-range order as feature E is smoothed out, resulting in the partial amorphization. Secondly, the enhanced intensity of peak B could be due to the contribution of (1) Na_2CO_3 impurity (resonance at the energy location of feature B in **Figure 6-7a**), or (2) reduced Ti-oxide species (e.g., Ti_2O_3 has a more intense peak B over A in **Figure 6-7a**), or (3) the change of O-Ti coordination number and the connectivity of the TiO_6 octahedral aroused by the leftover Na^+ ion in NTs after fully charging [46]. To confirm the latter, **Figure 6-7f** shows the Na K-edge PFY XANES of am-5 and c-5. Unlike the characteristic resonances $s_1 \sim s_4$ shown at the Na K-edge XANES of Na_2CO_3 (**Figure 6-7d**), both am-5 and c-5 exhibit the two similar broad features located between 1080 eV and 1100 eV, which are in accordance with our previous report of amorphous sodium titanate [46], where the broad doublet features indicate the short-range order of Na^+ ions [46-48]. Therefore, results from both O and Na perspectives are in alignment with the above Ti analysis, and unambiguously indicate that both amorphous and anatase TiO_2 NTs transform to the amorphous sodium titanate NTs after the first cycle of Na^+ insertion/extraction. It is worth noting that the sodiated titanates result from two different host materials might contain different structures, which totally explains why they provide different areal capacities for the long-term cyclability although both of them deliver the reversible Na^+ uptake/release capability (**Figure 6-2**).

6.4 Conclusions

Highly ordered TiO_2 NT arrays in both amorphous and anatase phases have been synthesized using electrochemical anodization, coupled with a post-annealing process for the preparation of the latter. The interaction between Na^+ and TiO_2 during electrochemical processes has been investigated, using both amorphous and anatase TiO_2 NTs as anode materials for the cycling of Na^+ uptake/release. The associated local structure variations of amorphous and anatase TiO_2 at the first cycle are comparatively examined using XANES. From the electrochemical perspective, amorphous TiO_2 NTs exhibits a lower sodiation potential and higher areal capacity than anatase NTs due to the distorted structure and rich defects involved in the former, allowing easier accommodation of Na^+ ions than the latter. Nonetheless, anatase TiO_2 with its two-dimensional ionic diffusion tunnels can also uptake Na^+ ion very quickly after its initial sodiation. From XANES results, we find that both amorphous and anatase TiO_2 NTs show a partial reduction of TiO_2 into metallic Ti upon Na^+ insertion, of which amorphous TiO_2 NT with its more active nature results in a larger amount of metallic Ti than anatase during sodiation. Meantime, a detailed XANES analysis at the Ti K and L, O K and Na K edges reveals that both amorphous and anatase TiO_2 NTs undergo phase transformations to amorphous sodium titanates after full charge at the first cycle. Accordingly, these newly formed structures, other than the original amorphous and anatase TiO_2, are responsible for the subsequent battery performance. Further analysis is underway to characterize the difference between these two amorphous sodium titanates, where a detailed structural analysis will contribute to the understanding of the process hence a pathway leading to the optimal performance of these materials for functional battery design.

6.5 References

[1] M. D. Ye, J. J. Gong, Y. K. Lai, C. J. Lin, and Z. Q. Lin, *J. Am. Chem. Soc.* **134**, 15720 (2012).

[2] X. B. Chen, L. Liu, P. Y. Yu, and S. S. Mao, *Science* **331**, 746 (2011).

[3] K. Zhu, N. R. Neale, A. Miedaner, and A. J. Frank, *Nano Lett.* **7**, 69 (2007).

[4] E. J. W. Crossland, N. Noel, V. Sivaram, T. Leijtens, J. A. Alexander-Webber, and H. J. Snaith, *Nature* **495**, 215 (2013).

[5] X. H. Lu, G. M. Wang, T. Zhai, M. H. Yu, J. Y. Gan, Y. X. Tong, and Y. Li, *Nano Lett.* **12**, 1690 (2012).

[6] H. Kim, M. Y. Cho, M. H. Kim, K. Y. Park, H. Gwon, Y. Lee, K. C. Roh, and K. Kang, *Adv. Energy Mater.* **3**, 1500 (2013).

[7] D. N. Wang, L. J. Liu, X. L. Sun, and T. K. Sham, *J. Mater. Chem. A* **3**, 412 (2015).

[8] L. M. Wu, D. Bresser, D. Buchholz, G. A. Giffin, C. R. Castro, A. Ochel, and S. Passerini, *Adv. Energy Mater.* **5**, 1401142 (2015).

[9] K. T. Kim, G. Ali, K. Y. Chung, C. S. Yoon, H. Yashiro, Y. K. Sun, J. Lu, K. Amine, and S. T. Myung, *Nano Lett.* **14**, 416 (2014).

[10] H. T. Fang, M. Liu, D. W. Wang, T. Sun, D. S. Guan, F. Li, J. G. Zhou, T. K. Sham, and H. M. Cheng, *Nanotechnology* **20**, 225701 (2009).

[11] S. Lunell, A. Stashans, L. Ojamae, H. Lindstrom, and A. Hagfeldt, *J. Am. Chem. Soc.* **119**, 7374 (1997).

[12] D. Bresser, E. Paillard, E. Binetti, S. Krueger, M. Striccoli, M. Winter, and S. Passerini, *J. Power Sources* **206**, 301 (2012).

[13] M. Wagemaker, W. J. H. Borghols, and F. M. Mulder, *J. Am. Chem. Soc.* **129**, 4323 (2007).

[14] J. R. Gonzalez, R. Alcantara, F. Nacimiento, G. F. Ortiz, and J. L. Tirado, *CrystEngComm* **16**, 4602 (2014).

[15] S. M. Oh, J. Y. Hwang, C. S. Yoon, J. Lu, K. Amine, I. Belharouak, and Y. K. Sun, *ACS Appl. Mater. Interfaces* **6**, 11295 (2014).

[16] H. Xiong, M. D. Slater, M. Balasubramanian, C. S. Johnson, and T. Rajh, *J. Phys. Chem. Lett.* **2**, 2560 (2011).

[17] D. W. Su, S. X. Dou, and G. X. Wang, *Chem. Mater.* **27**, 6022 (2015).

[18] J. F. Ni, S. D. Fu, C. Wu, J. Maier, Y. Yu, and L. Li, *Adv. Mater.* **28**, 2259 (2016).

[19] J. P. Huang, D. D. Yuan, H. Z. Zhang, Y. L. Cao, G. R. Li, H. X. Yang, and X. P. Gao, *RSC Adv.* **3**, 12593 (2013).

[20] S. K. Das, B. Jache, H. Lahon, C. L. Bender, J. Janek, and P. Adelhelm, *Chem. Commun.* **52**, 1428 (2016).

[21] Y. Xu, E. M. Lotfabad, H. L. Wang, B. Farbod, Z. W. Xu, A. Kohandehghan, and D. Mitlin, *Chem. Commun.* **49**, 8973 (2013).

[22] M. N. Tahir, B. Oschmann, D. Buchholz, X. W. Dou, I. Lieberwirth, M. Panthofer, W. Tremel, R. Zentel, and S. Passerini, *Adv. Energy Mater.* **6**, 1501489 (2016).

[23] J. Li, ; Liu, C. H.; Li, X.; Wang, Z. Q.; Shao, Y. C.; Wang, S. D.; Sun, X. L.; Pong, W. F.; Guo, J. H.; Sham, T. K., *Chem. Mater.* **28**, 4467 (2016).

[24] Y. F. Hu *et al.*, *AIP Conf. Proc.* **1234**, 343 (2010).

[25] T. Regier, J. Paulsen, G. Wright, I. Coulthard, K. Tan, T. K. Sham, and R. I. R. Blyth, *AIP Conf. Proc.* **879**, 473 (2007).

[26] J. Li, L. J. Liu, and T. K. Sham, *Chem. Mater.* **27**, 3021 (2015).

[27] J. R. Gonzalez, R. Alcantara, G. F. Ortiz, F. Nacimiento, and J. L. Tirado, *J. Electrochem. Soc.* **160**, A1390 (2013).

[28] F. Farges, G. E. Brown, and J. J. Rehr, *Phys. Rev. B* **56**, 1809 (1997).

[29] V. Luca, S. Djajanti, and R. F. Howe, *J. Phys. Chem. B* **102**, 10650 (1998).

[30] T. Rajh, J. M. Nedeljkovic, L. X. Chen, O. Poluektov, and M. C. Thurnauer, *J. Phys. Chem. B* **103**, 3515 (1999).

[31] Y. Joly, D. Cabaret, H. Renevier, and C. R. Natoli, *Phys. Rev. Lett.* **82**, 2398 (1999).

[32] Z. Y. Wu, G. Ouvrard, P. Gressier, and C. R. Natoli, *Phys. Rev. B* **55**, 10382 (1997).

[33] M. A. Khan, A. Kotani, and J. C. Parlebas, *J. Phys.: Condens. Matter* **3**, 1763 (1991).

[34] K. Okada and A. Kotani, *J. Electron Spectrosc. Relat. Phenom.* **62**, 131 (1993).

[35] S. J. Stewart, M. Fernandez-Garcia, C. Belver, B. S. Mun, and F. G. Requejo, *J. Phys. Chem. B* **110**, 16482 (2006).

[36] L. X. Chen, T. Rajh, Z. Y. Wang, and M. C. Thurnauer, *J. Phys. Chem. B* **101**, 10688 (1997).

[37] L. M. Wu, D. Buchholz, D. Bresser, L. G. Chagas, and S. Passerini, *J. Power Sources* **251**, 379 (2014).

[38] H. A. Cha, H. M. Jeong, and J. K. Kang, *J. Mater. Chem. A* **2**, 5182 (2014).

[39] C. X. Kronawitter *et al.*, *Nano Lett.* **11**, 3855 (2011).

[40] J. G. Zhou *et al.*, *J. Mater. Chem.* **19**, 6804 (2009).

[41] C. L. Chen *et al.*, *Phys. Chem. Chem. Phys.* **17**, 22064 (2015).

[42] F. M. F. Degroot, J. C. Fuggle, B. T. Thole, and G. A. Sawatzky, *Phys. Rev. B* **42**, 5459 (1990).

[43] P. Kruger, *Phys. Rev. B* **81**, 125121 (2010).

[44] M. K. Tian *et al.*, *ACS Nano* **9**, 10482 (2015).

[45] J. Li, C. H. Liu, Y. F. Ye, J. F. Zhu, S. D. Wang, J. H. Guo, and T. K. Sham, *J. Phys. Chem. C* **120**, 4623 (2016).

[46] J. Liu, M. N. Banis, B. W. Xiao, Q. Sun, A. Lushington, R. Y. Li, J. H. Guo, T. K. Sham, and X. L. Sun, *J. Mater. Chem. A* **3**, 24281 (2015).

[47] L. Cormier and D. R. Neuville, *Chem. Geol.* **213**, 103 (2004).

[48] S. De Wispelaere, D. Cabaret, C. Levelut, S. Rossano, A. M. Flank, P. Parent, and F. Farges, *Chem. Geol.* **213**, 63 (2004).

Chapter 7

7 Summary and Future Work

7.1 Conclusions

This thesis has focused on tracking the electronic and structural properties of vertically ordered TiO_2 nanostructures upon the morphology-dependent solid state phase transition, anion (N, F) doping, noble metal (Pd) coating and sodium intercalation, which are strongly correlated with their morphologies, chemical compositions and surface-bulk interactions. XAFS, STXM, XEOL and RIXS were applied as powerful tools to study these associated phenomena with both element and chemical site specificities.

Chapter 3 discussed the morphology-dependent phase transition in anodic TiO_2 nanostructures. As for the top nanograss and bottom nanotube hierarchical TiO_2 structure, the formation of nanograss from the unzipping of tip nanotube can greatly retard the ART temperature as revealed by XANES analysis at the Ti $L_{3,2}$-edge and O K-edge, due to its ultra-fine grain size. Specifically, whereas the nanograss shows an anatase-stable structure with an annealing temperature as high as 850 ℃, the nanotube exhibits the ART process at 550 ℃ and becomes rutile-dominant at 600 ℃ [1]. Thus the ART process as well as the crystal phase component(s) in anodic TiO_2 structure can be controlled by its morphology modification. To further understand the ART mechanism in nanotube, STXM measurements at the Ti $L_{3,2}$-edge and O K-edge were employed to spatially resolve the rutile nucleation site and growth behavior. It was found that the bottom nanotube cap is a fluorine-rich layer, which helps the exposure of anatase {001} facets [2,3] during anatase crystallization and then results in the subsequent ART phenomenon with elevated annealing temperature due to the lower rutile nucleation energy of anatase {001} than anatase {101} presented in the nanotube wall [4]. Accordingly, a bottom-up rutile nucleation and growth behavior was confirmed by the STXM results where the anatase-rutile mixed phase structure exhibits a top anatase nanotube layer with a dense rutile layer at the bottom together with a thin interface layer with a gradual ART located in-between. It suggests that rutile structure growth proceeds from bottom to the top at the expense of the nanotubular anatase phase via structural reconstruction.

Chapter 4 investigated the anion-doping effect on the electronic structure of TiO_2 nanotubes, where a black TiO_2 nanotube heterostructure with an anatase-core and an amorphous-shell has been synthesized by NH_3 annealing of amorphous nanotube grown by the anodization of a Ti substrate. Remarkable photoabsorption behavior of these black TiO_2 nanotubes was observed: strong absorption throughout the entire optical wavelength region from ultraviolet to near-infrared. XANES, XPS and RIXS were used to unravel the origin of this spectacular light capture phenomenon. Surface-sensitive XANES recorded in total electron yield and XPS showed that the surface layer is amorphous with a chemical composition approaching that of Ti_4O_7. Bulk-sensitive XANES using X-ray partial fluorescence yield and Ti 2p RIXS confirmed the presence of a rich amount of Ti^{3+} in the crystalline bulk (core of the nanotube with anatase structure) of black TiO_2 nanotubes which exhibits a dispersive d-d energy loss at ~2 eV corresponding to the broad visible light absorption at ~600 nm. Our results suggest that the extraordinary photoabsorption behavior of these black TiO_2 nanotubes is due to the stabilization of Ti^{3+} in this special N-doped core-shell assembly having structure varying between TiO_2 (bulk anatase) to Ti_4O_7 (surface, amorphous). Furthermore, a discussion regarding the core-shell construction with the assistance of self-doped fluorine species from electrochemical anodization was made to understand the associated core-shell formation mechanism.

In Chapter 5, the optical, structural and chemical properties of TiO_2 nanotubes upon Pd decoration (coating) were thoroughly studied. With a strong evidence of enhanced photoperformance from the Pd decorated TiO_2 nanotube specimen, this chapter mainly focused on characterizing the synergy between TiO_2 host structure and the secondary Pd nanoparticle. XANES at the Ti $L_{3,2}$- and O K-edges were firstly used to investigate the TiO_2 nanotubes before and after Pd modification. It was found that Pd nanoparticles are uniformly coated on, other than doping into, the nanotube surface. Pd L_3-edge of the as-decorated Pd nanoparticles showed a more intense whiteline and a blue shift for the Pd L_3-edge absorption threshold relative to Pd metal, indicating a charge-depletion from Pd 4d orbital as a result nanoparticle formation. The lattice of Pd is slightly contracted upon nanoparticle formation albeit it remains fcc as revealed from the EXAFS analysis at the Pd K-edge. XEOL together with XANES with element and site specificities were employed to study the optical luminescence from TiO_2 nanotubes. It was shown that the defect-originated XEOL intensity drops noticeably in the Pd decorated nanotubes, suggesting the interaction between Pd and TiO_2 can effectively hinder the radiative recombination of electrons and holes. Further evidence was provided by the Ti 2p RIXS analysis in which low energy loss features (d-d transition) were observed in bare TiO_2 nanotube but not in Pd decorated one, indicating the erase of surface trap states of TiO_2 upon Pd decoration [5].

Chapter 6 presented a mechanistic study of TiO_2 nanotube upon Na^+ uptake/release, of which the sodiation/desodiation behaviors of amorphous and anatase TiO_2 have been comparatively investigated. Specifically, the local structure variations of TiO_2 nanotubes in both structures upon sodiation/desodiation were examined by XANES studies at the Ti K- and L-, O K- and Na K- edges. Upon Na^+ ion insertion, the Ti K-edge analysis suggested that TiO_2 nanotubes in both amorphous and anatase phases are partially reduced to metallic Ti, which was found to be an inevitable product during the initial sodiation of TiO_2. Meantime, it was also shown that the sodiation of amorphous nanotubes is more effective than anatase. More importantly, the Ti K-edge results further revealed that irreversible phase transformations from pure amorphous and anatase TiO_2 nanotubes to amorphous sodium titanate nanotubes take place after the first cycle of discharge/charge, which was corroborated by the XANES study at the Ti L-, O K- and Na K-edges. These newly formed amorphous sodium titanates nanotubes hold the key to the performance of these materials. They provid a more open and flexible structures for the reversible uptake/release of Na^+ ions, and hence exhibit long-term stability and therefore can be used as promising anode materials for the design of sodium-ion batteries.

7.2 Future Work

As a wide band gap semiconductor, TiO_2 has a general low photoabsorption capability, limiting its solar energy conversion as well as photocatalytic efficiency. Meantime, its insufficient ionic transport hinders its practical application for battery design. To overcome these challenges, this thesis has pointed out four research directions: (1) the construction of synergistic anatase-rutile mixed phase structure, (2) anion doping, (3) noble metal decoration, and (4) the mechanistic investigation of Na^+ uptake/release behavior. Nevertheless, a further development and understanding of each direction is a necessity to improve the performance and efficiency of TiO_2 for future practical applications.

The ART of TiO_2 has been studied for many years. However, most of them have focused on the size-dependent ART of TiO_2 nanoparticles whereas the morphology-dependent (e.g., TiO_2 NT) ART research of TiO_2 has only received sporadic attention, in which the latter needs a detailed investigation due to the outperformance of well-ordered TiO_2 nanostructures than the nanoparticulate ones [6]. Using highly ordered TiO_2 NT synthesized by electrochemical anodization as an example, it was found that the rutile nucleation starts from the NT bottom (cap) and the growth of a dense rutile structure proceeds from the bottom to top at the expense of nanotubular anatase structure [7]. Therefore, on one hand, in order to prepare anatase-stable NT using in high temperature condition, the removal of the bottom cap and a finer modification of NT morphology such as length, wall thickness and diameter, will be promising routes. Unzipping of NT into nanograss can further increase the ART temperature [8]. On the other hand, another future prospect of TiO_2 NT might concentrate on the preparation of a more photoactive NT with a uniform distribution of anatase-rutile mixed structure which can optimize the synergy of anatase and rutile TiO_2.

Anion doping of TiO_2 NT has shown its enhanced photoabsorption towards the visible region, particularly, N doping can create an anatase-amorphous core-shell heterostructure which shows an extraordinary photoabsorption across the UV-NIR wavelength region [9]. Nonetheless, a further photoperformance test with respect to photoconversion as well as photocatalytic efficiency, needs to be carried out to fully functionalize this type of structure. More importantly, in-situ characterization of the N-doped core-shell TiO_2 NT in photocatalysis is of foremost importance to understand the photocatalytic mechanism of this unique heterostructure, of which in-situ XANES measurements with element and site specificities will be truly essential to reveal the contributions of N dopant and the core-shell interaction for the enhanced photoactivity.

It was found that Pd decoration on TiO_2 NT can efficiently suppress the surface defects of TiO_2 and reduce the recombination rate of photoexcited electron–hole pair [10]. Nevertheless, the photocatalytic efficiency still needs to be improved. It is well documented that metal alloy usually outperforms their individual metals due to their synergistic interaction. Indeed, the alloying of Pd with Au, Pt as well as other transitional metals with their established synergy has been widely reported [11-15]. Henceforth, the growth of secondary metal alloy nanostructure upon TiO_2 NT host structure is another effective route for the optimal of TiO_2 catalytic efficiency. Furthermore, in-situ XAFS analysis of metal (alloy)/TiO_2 system during photocatalytic reaction will provide further details in dynamic electronic interactions.

As for the application of TiO_2 in NIB research, it has been pointed out that TiO_2 would be inevitably transformed to amorphous sodium titanate after the first cycle of discharge/charge. The newly formed structure has showed its superior cycling stability and high rate performance. Thus experimentally, it is desirable to synthesize amorphous sodium titanate with different Na/Ti ratio for the purpose of achieving the best composition for accommodating the Na^+ during sodiation/desodiation. More importantly, in-situ/operando battery characterization using synchrotron X-rays will help elucidate the sodium ionic diffusion mechanism in amorphous sodium titanate to further optimize the composition for practical battery design.

7.3 References

[1] L. J. Liu, J. Chan, and T. K. Sham, *J. Phys. Chem. C* **114**, 21353 (2010).

[2] T. R. Gordon, M. Cargnello, T. Paik, F. Mangolini, R. T. Weber, P. Fornasiero, and C. B. Murray, *J. Am. Chem. Soc.* **134**, 6751 (2012).

[3] H. G. Yang, C. H. Sun, S. Z. Qiao, J. Zou, G. Liu, S. C. Smith, H. M. Cheng, and G. Q. Lu, *Nature* **453**, 638 (2008).

[4] S. C. Zhu, S. H. Xie, and Z. P. Liu, *J. Am. Chem. Soc.* **137**, 11532 (2015).

[5] A. Augustsson, A. Henningsson, S. M. Butorin, H. Siegbahn, J. Nordgren, and J. H. Guo, *J. Chem. Phys.* **119**, 3983 (2003).

[6] M. Z. Ge, C. Y. Cao, J. Y. Huang, S. H. Li, Z. Chen, K. Q. Zhang, S. S. Al-Deyabd, and Y. K. Lai, *J. Mater. Chem. A* **4**, 6772 (2016).

[7] J. Li, Z. Q. Wang, J. Wang, and T. K. Sham, *J. Phys. Chem. C* **120**, 9 (2016).

[8] J. Li, L. J. Liu, and T. K. Sham, *Chem. Mater.* **27**, 3021 (2015).

[9] J. Li *et al.*, *Chem. Mater.* **28**, 4467 (2016).

[10] J. Li, T. K. Sham, Y. Ye, J. Zhu, and J. Guo, *J. Phys. Chem. C* **119**, 2222 (2015).

[11] C. H. Liu, R. H. Liu, Q. J. Sun, J. B. Chang, X. Gao, Y. Liu, S. T. Lee, Z. H. Kang, and S. D. Wang, *Nanoscale* **7**, 6356 (2015).

[12] O. Rosseler, C. Ulhaq-Bouillet, A. Bonnefont, S. Pronkin, E. Savinova, A. Louvet, V. Keller, and N. Keller, *Appl. Catal., B* **166**, 381 (2015).

[13] L. Kesavan *et al.*, *Science* **331**, 195 (2011).

[14] K. Z. Jiang, P. T. Wang, S. J. Guo, X. Zhang, X. Shen, G. Lu, D. Su, and X. Q. Huang, *Angew. Chem., Int. Ed.* **55**, 9030 (2016).

[15] Q. F. Zhang, X. P. Wu, Y. K. Li, R. J. Chai, G. F. Zhao, C. Z. Wang, X. Q. Gong, Y. Liu, and Y. Lu, *ACS Catal.* **6**, 6236 (2016).

Appendix A: Copyright Release from ACS Publications

Title: 2D XANES-XEOL Spectroscopy Studies of Morphology-Dependent Phase Transformation and Corresponding Luminescence from Hierarchical TiO2 Nanostructures

Author: Jun Li, Lijia Liu, Tsun-Kong Sham

Publication: Chemistry of Materials

Publisher: American Chemical Society

Date: Apr 1, 2015

Copyright © 2015, American Chemical Society

Logged in as:
Jun Li

PERMISSION/LICENSE IS GRANTED FOR YOUR ORDER AT NO CHARGE

This type of permission/license, instead of the standard Terms & Conditions, is sent to you because no fee is being charged for your order. Please note the following:

- Permission is granted for your request in both print and electronic formats, and translations.
- If figures and/or tables were requested, they may be adapted or used in part.
- Please print this page for your records and send a copy of it to your publisher/graduate school.
- Appropriate credit for the requested material should be given as follows: "Reprinted (adapted) with permission from (COMPLETE REFERENCE CITATION). Copyright (YEAR) American Chemical Society." Insert appropriate information in place of the capitalized words.
- One-time permission is granted only for the use specified in your request. No additional uses are granted (such as derivative works or other editions). For any other uses, please submit a new request.

Copyright © 2016 Copyright Clearance Center, Inc. All Rights Reserved. Privacy statement. Terms and Conditions.
Comments? We would like to hear from you. E-mail us at customercare@copyright.com

Appendix B: Copyright Release from ACS Publications

Title: Unfolding the Anatase-to-Rutile Phase Transition in TiO2 Nanotubes Using X-ray Spectroscopy and Spectromicroscopy

Author: Jun Li, Zhiqiang Wang, Jian Wang, et al

Publication: The Journal of Physical Chemistry C

Publisher: American Chemical Society

Date: Sep 1, 2016

Copyright © 2016, American Chemical Society

Logged in as:
Jun Li

PERMISSION/LICENSE IS GRANTED FOR YOUR ORDER AT NO CHARGE

This type of permission/license, instead of the standard Terms & Conditions, is sent to you because no fee is being charged for your order. Please note the following:

- Permission is granted for your request in both print and electronic formats, and translations.
- If figures and/or tables were requested, they may be adapted or used in part.
- Please print this page for your records and send a copy of it to your publisher/graduate school.
- Appropriate credit for the requested material should be given as follows: "Reprinted (adapted) with permission from (COMPLETE REFERENCE CITATION). Copyright (YEAR) American Chemical Society." Insert appropriate information in place of the capitalized words.
- One-time permission is granted only for the use specified in your request. No additional uses are granted (such as derivative works or other editions). For any other uses, please submit a new request.

Appendix C: Copyright Release from ACS Publications

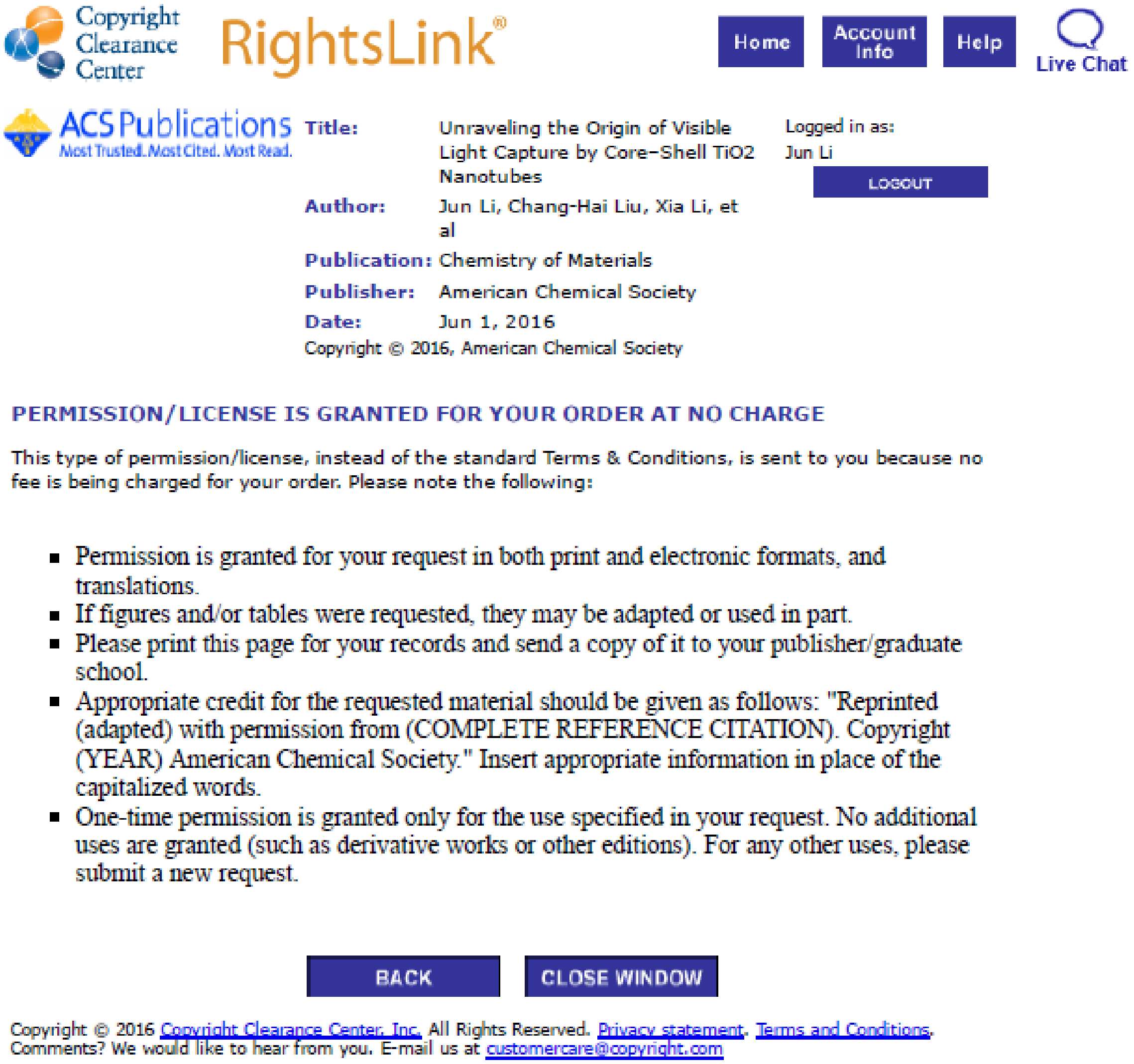

Title: Unraveling the Origin of Visible Light Capture by Core–Shell TiO2 Nanotubes

Author: Jun Li, Chang-Hai Liu, Xia Li, et al

Publication: Chemistry of Materials

Publisher: American Chemical Society

Date: Jun 1, 2016

Copyright © 2016, American Chemical Society

Logged in as:
Jun Li

PERMISSION/LICENSE IS GRANTED FOR YOUR ORDER AT NO CHARGE

This type of permission/license, instead of the standard Terms & Conditions, is sent to you because no fee is being charged for your order. Please note the following:

- Permission is granted for your request in both print and electronic formats, and translations.
- If figures and/or tables were requested, they may be adapted or used in part.
- Please print this page for your records and send a copy of it to your publisher/graduate school.
- Appropriate credit for the requested material should be given as follows: "Reprinted (adapted) with permission from (COMPLETE REFERENCE CITATION). Copyright (YEAR) American Chemical Society." Insert appropriate information in place of the capitalized words.
- One-time permission is granted only for the use specified in your request. No additional uses are granted (such as derivative works or other editions). For any other uses, please submit a new request.

Copyright © 2016 Copyright Clearance Center, Inc. All Rights Reserved. Privacy statement. Terms and Conditions.
Comments? We would like to hear from you. E-mail us at customercare@copyright.com

Appendix D: Copyright Release from ACS Publications

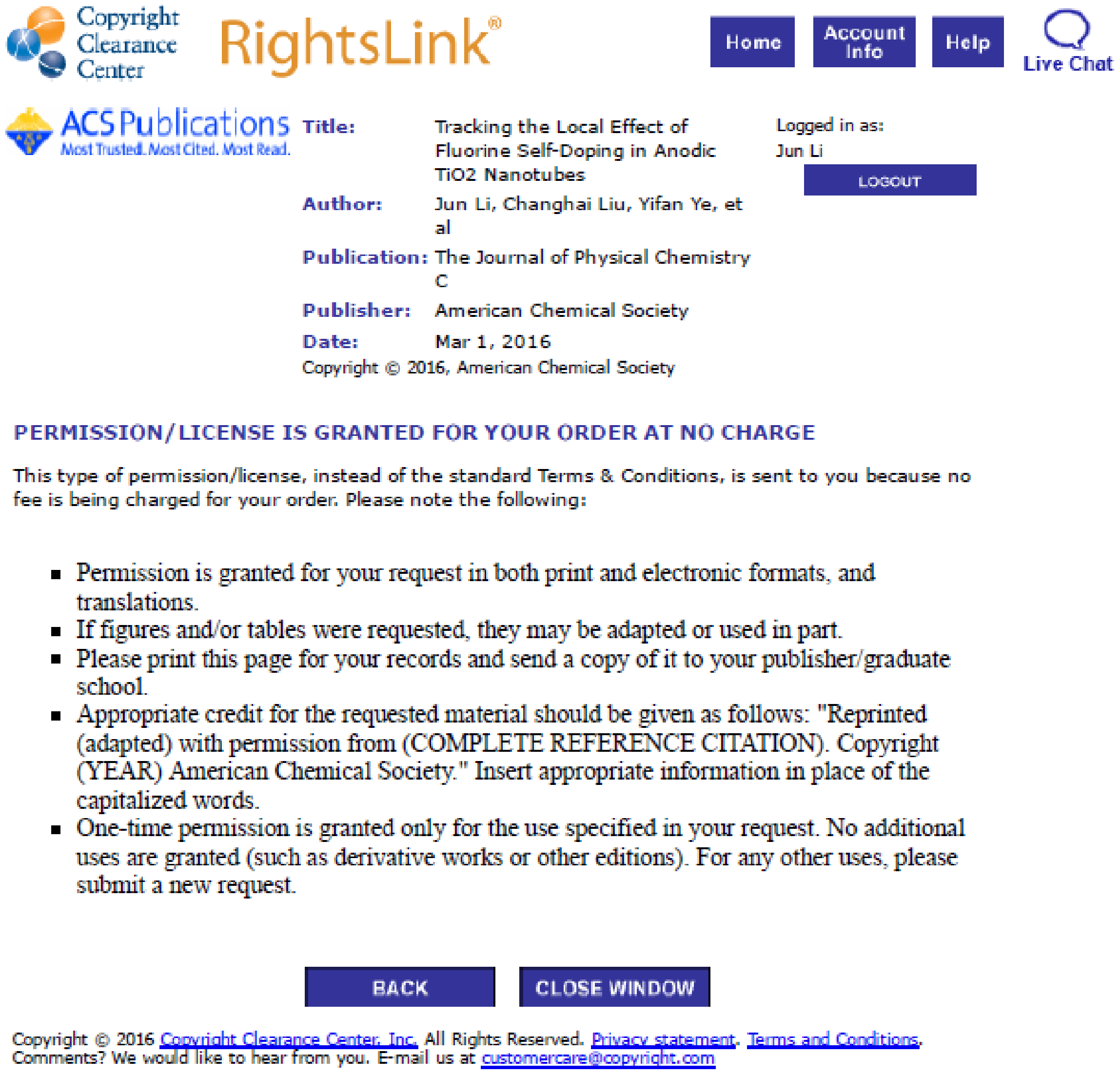

Title: Tracking the Local Effect of Fluorine Self-Doping in Anodic TiO2 Nanotubes

Author: Jun Li, Changhai Liu, Yifan Ye, et al

Publication: The Journal of Physical Chemistry C

Publisher: American Chemical Society

Date: Mar 1, 2016

Copyright © 2016, American Chemical Society

Logged in as:
Jun Li

PERMISSION/LICENSE IS GRANTED FOR YOUR ORDER AT NO CHARGE

This type of permission/license, instead of the standard Terms & Conditions, is sent to you because no fee is being charged for your order. Please note the following:

- Permission is granted for your request in both print and electronic formats, and translations.
- If figures and/or tables were requested, they may be adapted or used in part.
- Please print this page for your records and send a copy of it to your publisher/graduate school.
- Appropriate credit for the requested material should be given as follows: "Reprinted (adapted) with permission from (COMPLETE REFERENCE CITATION). Copyright (YEAR) American Chemical Society." Insert appropriate information in place of the capitalized words.
- One-time permission is granted only for the use specified in your request. No additional uses are granted (such as derivative works or other editions). For any other uses, please submit a new request.

Appendix E: Copyright Release from ACS Publications

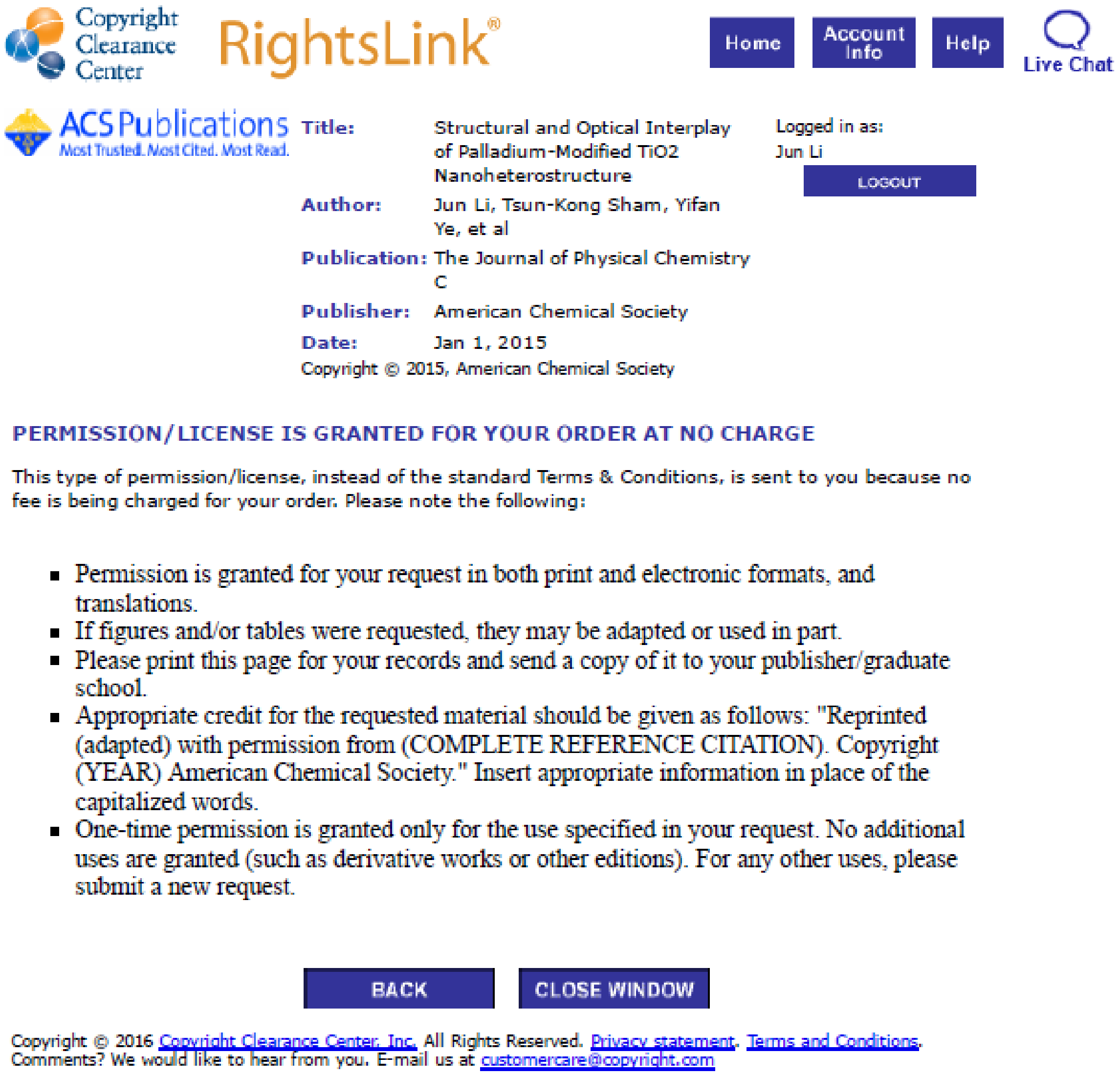

Title: Structural and Optical Interplay of Palladium-Modified TiO2 Nanoheterostructure

Author: Jun Li, Tsun-Kong Sham, Yifan Ye, et al

Publication: The Journal of Physical Chemistry C

Publisher: American Chemical Society

Date: Jan 1, 2015

Copyright © 2015, American Chemical Society

Logged in as:
Jun Li

PERMISSION/LICENSE IS GRANTED FOR YOUR ORDER AT NO CHARGE

This type of permission/license, instead of the standard Terms & Conditions, is sent to you because no fee is being charged for your order. Please note the following:

- Permission is granted for your request in both print and electronic formats, and translations.
- If figures and/or tables were requested, they may be adapted or used in part.
- Please print this page for your records and send a copy of it to your publisher/graduate school.
- Appropriate credit for the requested material should be given as follows: "Reprinted (adapted) with permission from (COMPLETE REFERENCE CITATION). Copyright (YEAR) American Chemical Society." Insert appropriate information in place of the capitalized words.
- One-time permission is granted only for the use specified in your request. No additional uses are granted (such as derivative works or other editions). For any other uses, please submit a new request.

Curriculum Vitae

Name:	Jun Li
Post-secondary Education and Degrees:	The University of Western Ontario London, Ontario, Canada 2013-present Ph.D. Candidate
	Harbin Institute of Technology Harbin, Heilongjiang, China 2008-2012 B.Eng.in Chemical Engineering
Honours and Awards:	CSC Travel Award 2016
	VUVX2016 Student Prize Award 2016
	CRC Student Prize Award 2016
	CLS Graduate Student Travel Award 2013-2016
Related Work Experience	Teaching Assistant in Chemistry The University of Western Ontario 2013-2016

Publications:

1. **J. Li,** J. Liu, Q. Sun, X. L. Sun, and T. K. Sham, Tracking the Sodium Uptake/Release Behavior in TiO_2 Nanotubes. *Phys. Chem. Chem. Phys.* Submitted (2016).

2. **J. Li,** A. Balaji, and T. K. Sham, Tracking the Morphology and Phase Transformations of Anodic Iron Oxide Nanotubes using X-ray Spectroscopy. *J. Electron Spectrosc. Relat. Phenom.* In press (2016) DOI: http://dx.doi.org/10.1016/j.elspec.2016.11.009

3. Y. Liu, S. Kim, J. A. McLeod, **J. Li,** X. X. Guo, T. K. Sham, and L. J. Liu, The Effect of Crystal Structure of TiO_2 Nanotubes on the Formation of Calcium Phosphate Coatings during Biomimetic Deposition. *Appl. Surf. Sci.* In press (2016). DOI: http://dx.doi.org/10.1016/j.apsusc.2016.11.114

4. **J. Li,** Z. Q. Wang, J. Wang, and T. K. Sham, Unfolding the Anatase-to-Rutile Phase Transition in TiO_2 Nanotube using X-ray Spectroscopy and Spectromicroscopy. *J. Phys. Chem. C* **120**, 22079 (2016).

5. **J. Li,** C. H. Liu, X. Li, Z. Q. Wang, Y. C. Shao, S. D. Wang, X. L. Sun, W. F. Pong, J. H. Guo, and T. K. Sham, Unraveling the Origin of Visible Light Capture by Core-Shell TiO_2 Nanotubes. *Chem. Mater.* **28**, 4467 (2016).

6. **J. Li,** C. H. Liu, Y. F. Ye, J. F. Zhu, S. D. Wang, J. H. Guo, and T. K. Sham, Tracking the Local Effect of Fluorine Self-Doping in Anodic TiO_2 Nanotubes. *J. Phys. Chem. C* **120**, 4623 (2016).

7. **J. Li,** L. J. Liu, and T. K. Sham, 2D XANES-XEOL Spectroscopy Studies of Morphology-Dependent Phase Transformation and Corresponding Luminescence from Hierarchical TiO_2 Nanostructures. *Chem. Mater.* **27**, 3021 (2015).

8. **J. Li,** T. K. Sham, Y. F. Ye, J. F. Zhu, and J. H. Guo, Structural and Optical Interplay of Palladium-Modified TiO_2 Nanoheterostructure. *J. Phys. Chem. C* **119**, 2222 (2015).

9. **J. Li,** Z. Q. Wang, A. K. Zhao, J. Wang, Y. Song, and T. K. Sham, Nanoscale Clarification of the Electronic Structure and Optical Properties of TiO_2 Nanowire with An Impurity Phase upon Sodium Intercalation. *J. Phys. Chem. C* **119**, 17848 (2015).

10. L. J. Liu, **J. Li,** and T. K. Sham, Near-Band-Gap Luminescence from TiO_2 Nanograss-Nanotube Hierarchical Membranes. *Can. J. Chem.* **93**, 106 (2015).

11. **J. Li,** A. Balaji, Z. Q. Wang, J. Wang, and T. K. Sham, A Facile Design of Iron Oxide Nanostructures with Anisotropic Alignment. *Manuscript*.

12. **J. Li,** C. H. Liu, M. N. Banis, Y. Yiu, X. L. Sun, S. D. Wang, and T. K. Sham, Revealing the Synergy in Bimetallic $PdPt/TiO_2$ Heterostructure. *Manuscript in preparation*.

Conference Presentations:

1. **J. Li,** Z. Q. Wang, J. Wang, and T. K. Sham, (Student Prize Talk) *39th International Conference on Vacuum Ultraviolet and X-ray Physics*. ETH Zurich, Switzerland, **Jul 2016**

2. **J. Li,** A. Balaji, and T. K. Sham, (Poster) *39th International Conference on Vacuum Ultraviolet and X-ray Physics*. ETH Zurich, Switzerland, **Jul 2016**

3. **J. Li,** C. H. Liu, Z. Q. Wang, S. D. Wang, and T. K. Sham, (Student Prize Talk) *99th Canadian Chemistry Conference and Exhibition*. Halifax, NS, **Jun 2016**

4. **J. Li,** Z. Q. Wang, X. X. Guo, O. Lobacheva, and T. K. Sham, (Poster) *Canadian Light Source 18th Annual Users' Meeting*. Saskatoon, SK, **May 2015**

5. **J. Li,** Z. Q. Wang, M. Kozachuk, and T. K. Sham, (Poster) *Ontario and Canada Research Chairs Symposium*. Toronto, ON, **May 2015**

6. **J. Li,** and T. K. Sham, (Poster) *Centre for Advanced Materials and Biomaterials Research (CAMBR) Conference*, London, ON, **Sept 2013**